DEVELOPMENT OF A LOW COST INFERENTIAL NATURAL GAS ENERGY FLOW RATE PROTOTYPE RETROFIT MODULE

FINAL REPORT

For the reporting period:
September 2002 – May 2005

Prepared by:

E. Kelner
D. George
T. Morrow
T. Owen
M. Nored
R. Burkey
A. Minachi

May 2005

Prepared for:
U.S. DEPARTMENT OF ENERGY
DOE Cooperative Agreement No. DE-FC21-96MC33033

DOE Technical Monitor
Anthony Zammerilli
Gas Technology Management Division

Submitted by:
SOUTHWEST RESEARCH INSTITUTE®
Mechanical and Fluids Engineering Division
6220 Culebra Road
San Antonio, Texas, USA 78238–5166

This page is intentionally blank.

DISCLAIMER

This page is intentionally blank.

DEVELOPMENT OF A LOW COST INFERENTIAL NATURAL GAS ENERGY FLOW RATE PROTOTYPE RETROFIT MODULE

E. Kelner
D. George
T. Morrow
T. Owen
M. Nored
R. Burkey
A. Minachi

SOUTHWEST RESEARCH INSTITUTE®
Mechanical and Fluids Engineering Division
6220 Culebra Road
San Antonio, Texas, USA 78238–5166

ABSTRACT

In 1998, Southwest Research Institute® began a multi-year project to develop a working prototype instrument module for natural gas energy measurement. The module will be used to retrofit a natural gas custody transfer flow meter for energy measurement, at a cost an order of magnitude lower than a gas chromatograph. Development and evaluation of the prototype energy meter in 2002–2003 included: (1) refinement of the algorithm used to infer properties of the natural gas stream, such as heating value; (2) evaluation of potential sensing technologies for nitrogen content, improvements in carbon dioxide measurements, and improvements in ultrasonic measurement technology and signal processing for improved speed of sound measurements; (3) design, fabrication and testing of a new prototype energy meter module incorporating these algorithm and sensor refinements; and (4) laboratory and field performance tests of the original and modified energy meter modules.

Field tests of the original energy meter module have provided results in close agreement with an onsite gas chromatograph. The original algorithm has also been tested at a field site as a stand-alone application using measurements from *in situ* instruments, and has demonstrated its usefulness as a diagnostic tool. The algorithm has been revised to use measurement technologies existing in the module to measure the gas stream at multiple states and infer nitrogen content. The instrumentation module has also been modified to incorporate recent improvements in CO_2 and sound speed sensing technology. Laboratory testing of the upgraded module has identified additional testing needed to attain the target accuracy in sound speed measurements and heating value.

This page is intentionally blank.

TABLE OF CONTENTS

LIST OF FIGURES

Page

LIST OF TABLES

Page

1. INTRODUCTION

1.1 BACKGROUND

Natural gas is priced and sold based on the energy delivered to the customer. The value of natural gas depends on the accurate determination of energy flow rate. Historically, the U.S. natural gas industry has determined energy flow rate using independent measurements of flow rate (rate of delivery) and heating value (combustible energy). In order to obtain the heating value of a gas, gas chromatography has traditionally been used to generate a composition assay from samples of the gas. This technology (installation and operational costs) and the sample-taking process required to support gas chromatographs are often too cost-prohibitive to be used on a wide scale.

Besides the economic considerations, deregulation (FERC Orders 436, 500, 636, etc.) and the increased accessibility of the market has caused supplies to become more varied in composition and less uniform in terms of energy content. Deregulation has expanded the supplier sources from large, single, well-defined sources to include many small suppliers of less defined or well-known compositions. Multiple supply (and/or storage) fields with widely varying gas qualities lose their identity when the gases are commingled in the pipeline. Heating value variations from 980 to 1250 Btu/scf may be recorded at the same locations over a period of time. Because energy content is less predictable, a way to measure energy flow rate locally and less expensively is a crucial need in the natural gas industry.

Energy flow rate measurement is critical to many aspects of the industry that rely on energy content (whether high or low) as a quality determination factor. Some suppliers (such as those with low-pressure Appalachian gas) provide richer gas than the rest of the country. If energy content is measured correctly, the richer portion can be stripped of its heavier hydrocarbons and sold separately without impacting the quality of the normal pipeline gas, thus providing a product with higher profitability for the suppliers. Most large end-users use gas for fuel and care about energy because a few percent change in heating value can have a large economic impact. Lower heating values mean more gas volume must be purchased so it is essential that energy rates be measured correctly. Finally, variations greater than 50 Btu/scf can adversely affect burner efficiencies in furnaces and engines, resulting in reduced operational efficiency.

In 1998, Southwest Research Institute® (SwRI®) performed an assessment of natural gas technology and a feasibility evaluation for the U.S. Department of Energy (DOE). The study aimed to compare traditional and alternative technologies for energy flow rate measurement in terms of their accuracy, capital investment, and "operational and maintenance" costs. The existing technology used by the industry is technically sound and fulfills accuracy requirements, but its inherent costs are difficult to justify in most cases. As an alternative to gas chromatographs, SwRI investigated use of an inferential approach to energy measurement developed by Behring et al. [1999]. Behring et al. found that flow and energy measurement properties may be determined with just a few inferential measurements that characterize the natural gas composition without a full composition analysis.

The SwRI study of 1999 determined that this alternative inferential approach to energy measurement was feasible. Heating values and densities may be calculated by sensing the speed of sound and the N_2 and CO_2 concentrations at a known temperature and pressure in a sample and then applying a gross inferential correlation equation. The correlation is based on a database of 102 different natural gas compositions (987-1150 Btu/scf and 83.4-98.3 mol% methane). This database represents essentially a full practical range of natural gas mixtures under gas quality tariff authority. The inferential approach uses a curve fit to adjust the pressure and temperature of the reference database to sample conditions and a regression equation to predict molecular weight and heating value based on the AGA-8 Gross Characterization Method (American Gas Association [1994]).

The feasibility of the approach was demonstrated by sensing the speed of sound, the carbon dioxide concentration, the nitrogen concentration, the temperature, and the pressure. Existing ultrasonic transducers and carbon dioxide sensors were used in a proof-of-concept study. Laboratory tests of these sensors in combination with the gas heating value algorithm supported the technical feasibility of the new approach. No sensor for nitrogen concentration was available for this application, but indirect measurement approaches were identified. The 1999 study recommended certain refinements in the speed of sound and carbon dioxide sensors and investigation of the suggested indirect nitrogen-sensing methods.

Co-funded by the Gas Technology Institute (GTI) and the U.S. Department of Energy, the project was continued in 1999-2000 with the goal of developing a prototype energy meter module (Morrow et al. [2000]). The goal of this second phase of work was to retrofit a natural gas custody transfer flow meter for energy measurement at a cost an order-of-magnitude lower than a gas chromatograph. The correlation developed for the inferential technique was revised at the recommendation of the GTI Measurement Technical Advisory Group (MTAG) to use the speed of sound at arbitrary pressure and temperature as a correlation variable. In response to this recommendation, the inferential correlations were reformulated to employ the sound speed and the N_2 and CO_2 concentrations at arbitrary temperature and pressure without significant loss of accuracy. An energy meter module was then built to measure the inferential properties (CO_2, N_2, and sound speed) on a sample gas stream at reduced pressure. The module included specialized sensors for CO_2 and speed of sound and conventional sensors to measure temperature and pressure. To perform the correlation calculations and apply the AGA-8 Gross Characterization Method, a FORTRAN computer code was translated into ACCOL to run on a Bristol Babcock Model 3330 flow computer commonly used for flow metering installations in the field.

The energy meter algorithm was tested in combination with an ultrasonic flow meter operating in the MRF High Pressure Loop (HPL). For the ultrasonic flow meter tests, conventional sound speed, pressure, and temperature values at pipeline conditions from the flow meter were substituted for the prototype energy meter module measurements. Carbon dioxide and nitrogen concentrations were obtained from the MRF gas chromatograph. These inputs were fed to the Bristol Babcock flow computer for calculating the standard volumetric gas heating value. Communication problems limited the number of energy meter performance tests within the period of time reserved for testing in the MRF. However, abbreviated tests using a 12-inch

Daniel Model 3400 ultrasonic meter in the HPL indicated that the standard volumetric heating value was determined accurately to within ±1 Btu/scf.

The prototype energy meter module was tested with a 4-inch orifice flow meter in the Low Pressure Loop (LPL). For these tests, speed of sound and CO_2 concentration were measured with the prototype energy meter module. These tests showed a +47 Btu/scf difference between the measured heating value and the known reference value, due to a variety of factors. However, the measured value of CO_2 concentration was within an average of 0.054 mol% of the known value determined by the gas chromatograph, corresponding approximately with the allowable error of ±0.05 mol% for this measurement. Because of the large disparity in heating value, project priority was focused on resolving the cause of the heating value error.

Analysis of the experimental test data indicated that the principal source of error was in the measured speed of sound in the gas. Two discrepancies were found in the operating performance of the speed of sound sensor, the first related to reliably determining the ultrasonic pulse reflection transit time and the second related to measuring the true gas temperature in the speed of sound test chamber. When appropriate corrective adjustments were applied to the experimental transit times the error in heating value was reduced to +15.2 Btu/scf, demonstrating the strong influence of sound speed on the derived heating value. Similar adjustments applied to the gas temperature in the speed of sound test chamber reduced the heating value error to –2.3 Btu/scf. These results led to positive conclusions regarding the feasibility of the energy meter concept, and recommendations for improvements in the ultrasonic transducer and in modifying the speed of sound sensor design so that the gas volume under test was always at the same temperature as the ultrasonic test chamber.

Development of the prototype retrofit energy meter module in 2001-2002 involved evaluation of the inferential algorithm for wider gas compositions, a review of potential sensing methods for nitrogen content, performance testing of improved CO_2 sensors and ultrasonic transducers and a new speed of sound sensor chamber, controlled tests of the prototype module in the MRF HPL and LPL, and a two-week test of the inferential algorithm at a field site having appropriate ultrasonic flow meter and gas chromatograph facilities.

The algorithm studies showed that worst-case conditions within the normal range of the AGA-8 equation of state yielded gas density and molecular weight within ±0.1 percent. The algorithm was further evaluated using additional gas databases (more than 800 gas compositions ranging from 960-1140 Btu/scf), resulting in tightening the speed of sound measurement accuracy from ±1.5 ft/sec for the normal AGA-8 range to ±0.8 ft/sec for the expanded gas databases. These studies also showed that with measurements of other diluents, particularly oxygen, the algorithm could potentially be applied to gases having up to 20 mol% diluent content.

Four sensing methods for nitrogen were identified and evaluated, including a patented GRI inferential method for the gas mixture specific heat at constant volume as a correlate for nitrogen content, electronic microsensors for measuring either gas thermal conductivity or viscosity as

correlates for nitrogen, nuclear magnetic resonance measurements of nitrogen, and infrared absorption measurements of the hydrocarbon and CO_2 content to yield nitrogen as the balance. The microsensor approach, under development by Honeywell at the time, was found to be the most promising method.

The sound speed sensor gas test chamber was redesigned to operate as an ambient-temperature heat sink for the gas sample flow path with a custom-designed ultrasonic transducer operation at 279 kHz with 128 kHz bandwidth. Tests of this sensor in the MRF HPL and LPL facilities demonstrated that residual errors less than ±1 ft/sec could be obtained for transmission-quality natural gas.

A commercially available nondispersive infrared absorption CO_2 sensor designed to operate at a pressure of 1 atm was tested in the HPL and LPL using gases containing CO_2 concentrations in the range of 1-9 mol%. This sensor was found to provide CO_2 measurements to within ±0.05 mol% or less for CO_2 concentrations up to 3 mol%. Measurements at 6 mol% and 9 mol% revealed nonlinearities in sensor response, indicating the need for a more comprehensive calibration and response compensation procedure to provide measurements within the accuracy limit for use in the heating value algorithm.

The prototype sensor module tests in the MRF HPL and LPL using gases having less than 3 mol% CO_2 showed that gas heating values were measurable well within the expected worst-case algorithm error bounds of ±2.4 Btu/scf. A two-week field test of the inferential algorithm was performed at a gas-fired power plant in which the sound speed, pressure, and temperature at pipeline conditions were derived from an ultrasonic flow meter, and CO_2 and N_2 diluent concentrations were provided by a gas chromatograph. Using the diluent concentrations obtained on the first day and holding these values constant throughout the test period showed that the gas heating value was derived within ±10 Btu/scf of the value derived by local gas chromatographic analysis. Reprocessing the test data using continuously monitored CO_2 and N_2 values demonstrated that the gas heating value could be derived within an accuracy of -5 to +8 Btu/scf of the gas chromatograph value.

1.2 PROJECT TASKS AND GOALS, 2002-2003

An accuracy level of ±1 Btu/scf in gas heating value is a desired performance goal for the energy meter if it is to be considered as a replacement for a gas chromatograph. To achieve this level of accuracy in an improved prototype energy meter module, and to more thoroughly evaluate and expand the inferential algorithm, further development of the energy meter was performed in 2002 and 2003. The development project was co-sponsored by the U.S. Department of Energy and Pipeline Research Council International, and worked to accomplish the following tasks:

1. Evaluate, Refine, and Expand the Range of the Algorithm – Develop refinements of the inferential algorithm through conversion to the FORTRAN language and the embedding of a computational version of the AGA-8, and when available, the AGA-10 equation of

state. This revision will supersede the use of regression analysis and interpolation tables previously required to generate the reference gas database correlation parameters for deriving test gas heating values. This FORTRAN code will be adapted for use in an IIT portable data logger system for use in field evaluation tests of the algorithm as a stand-alone technology and as part of the new prototype energy meter module. A batch-processing version of the FORTRAN code will be developed to facilitate continued study of the algorithm, with focus on the use of inferential methods for determining the nitrogen content in the absence of a direct means for sensing nitrogen.

2. Energy Meter Sensors – Evaluate direct and indirect methods for determining the nitrogen concentration in the test gas, including the possible use of currently emerging microsensor technology and similar technical approaches. Modify the inferential energy analysis algorithm to derive nitrogen concentration as a supplemental unknown variable from input sensor measurements of sound speed, pressure, temperature, and carbon dioxide. Adapt the CO_2 sensor to operate at an elevated pressure corresponding to that used in the speed of sound test chamber, to permit the new module design to contain only one gas test chamber for both sound speed and CO_2 measurements. Specify and procure a custom-designed ultrasonic transducer capable of providing the broad bandwidth required for reliable high-resolution pulse time-of-flight measurements. Discuss with ultrasonic transducer manufacturers the opportunity to develop a new transducer product for a future commercialized version of the gas energy module. Develop improvements in the existing ultrasonic pulse time-of-flight signal processing techniques to provide greater precision in the measured speed of sound, including flexible methods for improving the pulse signal-to-noise ratio observed in certain sound-absorptive gas mixtures.

3. New Prototype Energy Meter Module – Design, fabricate, and test a new prototype energy meter module incorporating the advanced sensor developments defined in Task 2, including sensor modifications required for determining the nitrogen content of the test gas and interfacing with the data logger and algorithm computing unit.

4. Energy Meter Laboratory and Field Tests – Perform tests of the prototype energy meter module and data logger unit as a complete stand-alone energy meter system under controlled environmental conditions and at a gas pipeline field site, to demonstrate the operating performance and reliability of the system. Perform tests of the upgraded data logger unit equipped with the FORTRAN algorithm as a stand-alone gas energy analysis application for use at a gas pipeline terminal equipped with an ultrasonic flow meter and a gas chromatograph. Perform controlled laboratory tests of the new prototype energy meter module to demonstrate the performance of the improved sensors and data processing capabilities, including the ability to determine the nitrogen concentration in the test gas.

5. Market Survey and Commercialization – continue to assess the current prospects and industry interests in extending the inferential gas energy analysis algorithm and prototype energy meter module to commercial status. Perform a survey of industry technical representatives in the user sector to establish consensus views on current gas energy measurement needs and estimates of the potential deployment of the emerging technology being developed on this project. Inform technical representatives in the gas

industry equipment manufacturing sector of the technical developments and accomplishments and the projected market for the new technology.

1.3 SUMMARY OF ACCOMPLISHMENTS, 2002-2003

Significant progress was made on all the task objectives for 2002-2003. The results and recommendations for further development work are summarized in the following subsections.

1.3.1 Algorithm Evaluation and Refinement

Because of limited success in identifying a practical means of inferring the nitrogen content of a gas stream from measurable gas properties, the energy meter algorithm was revised to use measurements of sound speed, temperature and pressure of the gas at two different states to infer the nitrogen content. A batch version of the revised algorithm was first used to determine the optimum difference in pressures between the two states that would produce acceptable uncertainty in nitrogen content and heating value of the gas stream. The algorithm was then modified as originally planned to use the AGA-8 equation of state to compute sound speed values of gases for curve fits by the algorithm. The use of AGA-8 instead of interpolation tables for obtaining natural gas properties was shown to reduce errors in computed properties of the analyzed gas stream such as nitrogen content and heating value.

The two-state energy meter algorithm was then rewritten to incorporate the most recent standard for sound speed calculation, AGA-10. The best results from this version of the algorithm were found when the errors in the values of speed of sound input to the algorithm were less than ± 0.1 ft/s. Because this new accuracy requirement for sound speed imposed impractical requirements on data acquisition, two complementary methods were developed for obtaining sound speed measurements within the limitations of the existing energy meter sensor hardware. The first method improves the resolution of sound speed by interpolating along a polynomial fitted to the ultrasonic signal cross-correlation function. The second method expands the number of states at which the sound speed of the gas stream is measured from two to seven, to reduce the uncertainty in the mean values of heating values and other computed gas properties. For future development of the inferential energy meter toward commercialization, it is recommended that this multiple-state algorithm be implemented in an IIT data logger system for laboratory and field tests with the energy meter module.

1.3.2 Energy Meter Sensors

Two methods conceived for determining nitrogen content, both involving measurements of the gas viscosity, were evaluated experimentally to determine their potential accuracy. One sensor, developed by Honeywell around a commercial thermal anemometer, had insufficient accuracy and stability in its current form for use in the energy meter prototype. A second method involved the use of laminar flow elements to measure the gas viscosity and determine its nitrogen content. Existing hardware within the energy meter module, commercial copper tubing, and a commercial laminar flow element were all tested as potential tools for viscosity

measurement, but ambient conditions and the gas flow rate through the element were found to shift the calibration factor by as much as 20%. It was concluded that the laminar flow method of viscosity measurement would not be viable for inferring the nitrogen content of natural gas. This approach was finally set aside in favor of the modified algorithm and the measurement of sound speed at multiple states discussed above, which is recommended for further development as the energy meter system is commercialized.

The existing CO_2 sensor was successfully adapted to operate in an integrated sound speed/CO_2 chamber at the elevated pressures required for sound speed measurements. This was accomplished by calibrating the CO_2 sensor on several test gases over the range of expected operating pressures and CO_2 concentrations. A nonlinear correction equation was then incorporated into the algorithm to adjust the sensor readings for effects of elevated pressures. For improved sound speed measurements, specifications were developed for a new custom-designed ultrasonic transducer, and discussions were held with two manufacturers to identify or develop new transducers meeting the requirements, particularly bandwidth requirements for high-resolution time of flight measurements in the sound speed chamber. Bench tests of transducers from the two manufacturers led to the selection of a commercially-available 1-MHz transducer for use in the prototype speed of sound sensor, and this transducer is recommended for use in additional prototypes as the technology is developed for commercialization. Data acquired during this evaluation was also used in later signal processing model studies to develop software methods for improving the accuracy and resolution of the time difference derived from the cross correlation function and the signal-to-noise ratio of the ultrasonic signals. These methods include an interpolation of the cross correlation function used to determine the time-of-flight of sound pulses in the chamber, and averaging of multiple waveforms to reduce noise in the cross correlation.

1.3.3 New Prototype Energy Meter Module

A new prototype system was designed and built to incorporate the advanced sensor developments described above and implement the new multiple-state algorithm for inferring nitrogen content and heating value of the gas stream. For ease of integration, the prototype is composed of three separate modules containing the gas sensors, electronics, and control and data acquisition equipment, respectively. An integrated speed-of-sound and CO_2 measurement test chamber was designed and fabricated as part of this system, with the capability to precondition the gas temperature and gas flow for accurate speed-of-sound and CO_2 measurements. Communications protocols and timing requirements for the integrated energy meter system were used to program an IIT RGC data logger, which serves as the control and data acquisition module and also performs algorithm calculations. Laboratory tests of this prototype module, discussed in the following paragraphs, found the basic functionality of the new system to be sound. Based on the results of those tests, it is recommended that additional tests of the new prototype be performed to gather experimental data that will further refine the accuracy of the multi-state algorithm.

1.3.4 Energy Meter Laboratory and Field Tests

Laboratory tests were performed with the original single-state energy meter module in an environmental chamber to determine its operational performance characteristics, specifically its operating ranges in ambient temperature, gas pressure and gas diluent concentration. The speed of sound test chamber and the ultrasonic transducer performed acceptably well under all of the temperature and pressure conditions tested, and in natural gas mixtures containing diluent concentrations ranging from 0.5 to 14 mol%. However, it was found that the transducer did not uniformly radiate ultrasonic pulses into the speed of sound test chamber, leading to requirements for beam pattern uniformity and more stable operation over a wider temperature range for future ultrasonic transducers. With the application of a simple linear pressure correction, the CO_2 sensor performed within specifications at all but the highest temperature; these results led to the nonlinear pressure correction described previously. The single-state energy meter module demonstrated accurate overall performance in determining the heating value for a series of eight test gases under environmental and operating conditions anticipated in the field. The effects of high diluent concentrations and fluctuations in sound speed and CO_2 measurements at higher temperatures did not cause heating value errors to exceed the uncertainty requirements of the algorithm.

The energy meter module was also field tested at a custody transfer meter station in south Texas, marking the first field test of the module using pipeline gas. These tests exposed the module to environmental ambient conditions, applied the nonlinear CO_2 calibration correction, and used an onsite flow computer for algorithm calculations. Field test results were compared to reference values derived from an onsite gas chromatograph. The module sensors and electronics were only slightly affected by diurnal changes in ambient temperature, and the carbon dioxide sensor demonstrated reliable operation throughout the field test. The sound speed sensor produced measurements that were offset from values computed from the gas chromatograph data and the AGA-8 equation of state; the offset is believed to be related to the absolute calibration of the energy meter module before tests. During the tests, malfunctions occurred in the reference gas chromatograph that produced a consistent error in heating values computed from its analysis. This suggested the use of the energy meter module as a tool to verify the performance of onsite equipment such as the gas chromatograph. The energy meter module tracked the heating value provided by the gas chromatograph analysis very well, with a difference of ±1 Btu/scf observed during periods when the gas chromatograph was functioning correctly.

Another application of the technology tested during the research was the use of the algorithm as a stand-alone application, using input values from instruments at a metering station to monitor gas quality and to verify the performance of onsite instruments. To test this potential application, the single-state algorithm was installed on a combination data logger and flow computer, which was then installed at a compressor station in south Texas not used for custody transfer activities. The unit was programmed to accept sound speed, pressure and temperature data from an ultrasonic meter at the site, as well as nitrogen and CO_2 data from an onsite gas chromatograph (GC). The algorithm calculated heating values using both measured and assumed values of diluents as a means of testing three potential implementations of the algorithm. Differences between heating values from the algorithm and the onsite GC led to the

discovery of black powder in the metering station, which was causing small errors in ultrasonic meter measurements and significant lag times in the analysis of the gas stream by the gas chromatograph. After the lag in GC analysis was corrected, heating values computed by the algorithm during periods of flow at the station agreed with heating values computed by the GC to within 0.2 Btu/scf, well within the target accuracy of the algorithm. These field tests support the use of the algorithm as a stand-alone diagnostic tool for metering station instruments as well as part of the inferential energy meter, and it is recommended that this application be pursued during commercialization of the technology.

The last tests of the energy meter technology as part of this project involved laboratory tests of the 2003 prototype energy meter module designed for two-state operation. These tests were performed to evaluate the pressure control and response time of the two-state measurement system, determine the gas volume replacement time of the integrated sound speed and carbon dioxide test chamber, and collect sound speed and carbon dioxide measurements to provide a database for evaluating the sensors and the two-state inferential algorithm. Tests determined that a new, stable pressure-temperature state within the sound speed-CO_2 chamber can be produced within 60 seconds of the command by the pressure regulator to change states. Removal of portions of the CO_2 probe to shorten the stabilization time of measurements after a change in gas composition is recommended for future module prototypes.

Measurements of CO_2 concentrations of several test gases, using the nonlinear pressure correction described earlier, were within the accuracy required by the energy meter algorithm. However, when sound speed measurements in the test gases were compared with values computed using the AGA-10 equation of state, discrepancies of varying magnitude and sign were observed for all the test gases. Further investigation revealed three possible sources of the observed discrepancies in the experimental and calculated sound speed values: (1) composition-dependent measurement bias in the sound speed sensor, (2) inaccuracy in the certified test gas compositions that are being detected by the energy meter module, and (3) inaccuracy in sound speed calculations produced by AGA-10 due to molecular-level effects in the gas. As development of the module proceeds, it is recommended that these potential sources of discrepancies be investigated, respectively, through the following tests: (1) additional measurements of sound speed using ultrapure gases, (2) gas chromatographic analyses of the test gases, and (3) measurements of sound speed in the test gases at two different ultrasonic frequencies to identify any viscous attenuation and molecular relaxation absorption effects causing the discrepancies.

1.3.5 Market Survey and Commercialization

Meetings began in October 2003 with representatives from the natural gas industry and manufacturing interests to assess the potential for a Joint Industry Project (JIP) to fund continued development of the technology and extend it to commercial status. Attendees at the meetings included potential users who indicated their intent to participate in the JIP, and manufacturers interested in licensing the technology. Several meetings were held with candidate manufacturers to discuss commercialization of the energy meter, potential markets and licensing considerations.

Formation of the JIP was completed in October 2004, with seven pipeline companies participating. YZ Systems has been chosen as the commercialization partner of the two-state retrofit energy meter technology for the JIP. Negotiations are currently in progress with other companies to commercialize the algorithm as a stand-alone application, as recommended above. The terms of the JIP include a statement of work to complete development of the technology. The scope of work will include the items recommended above for further development, including the implementation of the multiple-state algorithm in a data logger as part of the energy meter system, potential redesigns of the CO_2 and sound speed sensors, and additional tests with the new prototype of ultrapure gases at multiple ultrasonic frequencies to gather experimental data and further refine the accuracy of the multi-state algorithm.

2. EVALUATION AND REFINEMENT OF THE INFERENTIAL ALGORITHM

The energy meter algorithm uses model equations to relate the molecular weight and the density of an unknown natural gas mixture to three variables: (1) the molar concentration of carbon dioxide, X_{CO2}; (2) the molar concentration of nitrogen, X_{N2}; and (3) the speed of sound, S, at the specified temperature and pressure. The model equation for molecular weight is:

$$MW_{calc} = \left(A_{MW} + B_{MW}/S + C_{MW}/S^2 \right) * \left(1 + D_{MW} * X_{CO2} + E_{MW} * X_{N2}\right) \tag{2.1}$$

where:

$$D_{MW} = D_{MW1} + D_{MW2}/S + D_{MW3}/S^2 \text{, and } E_{MW} = E_{MW1} + E_{MW2}/S + E_{MW3}/S^2 \tag{2.2}$$

The nine parameters in the model equation, A_{MW}, B_{MW}, C_{MW}, D_{MW1}, D_{MW2}, D_{MW3}, E_{MW1}, E_{MW2} and E_{MW3}, are determined using an equation of state and least squares error regression. A similar equation is used to infer natural gas density.

2.1 THE SINGLE-STATE METHOD

For a given natural gas mixture, the molar concentrations of carbon dioxide and nitrogen are independent of pressure and temperature, but values of speed of sound are dependent upon these state variables. In the single-state method, the speed of sound and the carbon dioxide and nitrogen concentrations are all determined from measurements at a single thermodynamic state. These measurements are input to the algorithm along with the measured pressure and temperature at that state to determine the density and molecular weight of the gas.

2.1.1 Sound Speed at Standard Temperature and Pressure

The original energy meter algorithm developed by Behring et al. [1999] specified that the speed of sound was to be measured at standard pressure, P_{std} = 14.73 psia, and standard temperature, T_{std} = 60°F. The nine unknown parameters in Equations (2.1) and (2.2) were determined from a regression fit to values of standard sound speed, nitrogen concentration, and carbon dioxide concentration for a selection of 102 natural gas mixtures, and used for all data analysis. A similar regression fit was made to data for standard density as a function of standard sound speed, nitrogen concentration, and carbon dioxide concentration. Algebraic equations were developed from these regressions that related measured values of standard sound speed, nitrogen concentration, and carbon dioxide concentration for a natural gas mixture of unknown composition to the mass-based heating value and the standard volumetric heating value of that gas.

2.1.2 Sound Speed at Arbitrary Temperature and Pressure

The stipulation that the speed of sound be measured at standard pressure and temperature was thought to be too restrictive for field implementation. Therefore, the algorithm was extended to arbitrary temperature and pressure by Morrow et al. [2000]. Equations (2.1) and (2.2) were still used for molecular weight, as were similar equations for natural gas mixture density. However, the nine model parameters would now be determined from values of molecular weight, density and speed of sound for nine reference natural gas mixtures, all at the same pressure and temperature as the sound speed measurement for the unknown natural gas mixture. The use of nine reference mixtures allowed the nine parameters to be determined by direct solution of the equations, rather than by regression. The nine reference gas mixtures covered a range of molecular weights from 16.20 lb_m/lb_{mol} to 20.20 lb_m/lb_{mol}, and a range of standard heating values from 961.6 Btu/scf to 1176 Btu/scf. Three of the nine reference gas mixtures had 0% mol concentration of nitrogen and carbon dioxide. Three of the reference gas mixtures had 2 mol% concentration of nitrogen and 4 mol% concentration of carbon dioxide. The final three reference gas mixtures had 4 mol% concentration of nitrogen and 2 mol% concentration of carbon dioxide.

As stated above, in order to calculate the model parameters for this implementation, values would be needed for the molecular weight, and for the density and the sound speed of the nine reference gas mixtures at the temperature and pressure at which the sound speed was measured in the gas mixture of unknown composition. Values of molecular weight were calculated for the nine reference gas compositions using GPA 2145-94 (Gas Processors Association [1994]). In order to determine sound speeds and values of density at arbitrary temperature and pressure, however, interpolation tables were developed from calculated values. SonicWare® (Lomic [1997]) was used to calculate values of speed of sound and density for temperatures between 20°F and 150°F in steps of 10°F, and for pressures of 14.73 psia, 50 psia, and 100 psia to 1400 psia in increments of 100 psia.

A computer code was written to perform a cubic-spline interpolation that provided values of sound speed and density for the nine reference gas mixtures at any combination of pressure and temperature within the range of the interpolation tables. The calculated values of molecular weight, and the interpolated density and sound speed values, were used to calculate the model parameters in Equations (2.1) and (2.2) exactly. Next, the model equations, together with measured values of sound speed, nitrogen concentration and carbon dioxide concentration in the natural gas mixture of unknown composition, were used to infer values of the molecular weight and gas density at measurement conditions for the unknown gas mixture.

To compute the standard volumetric heating value of the unknown gas, however, data was also required for the unknown gas at standard conditions. The least squares error correlations at standard pressure and temperature would require the standard sound speed for the unknown gas mixture, which would not be available through measurements. However, the molecular weight, nitrogen concentration, and carbon dioxide concentrations of the unknown gas mixture were already known, so Equation (2.1) could be rearranged and solved for standard sound speed using the nine parameters calculated at standard temperature and pressure for the reference gas mixtures. This quadratic equation was solved exactly for the standard sound speed, and the

result was used with correlations similar to Equations (2.1) and (2.2) to calculate mass-based heating value, standard density, and standard volumetric heating value.

A computer code was written in FORTRAN to demonstrate the validity of this approach. The FORTRAN computer code was eventually translated into ACCOL, and the energy meter algorithm was implemented on a Bristol Babcock model 3330 flow computer.

2.2 THE TWO-STATE METHOD

The methods described above work well when the value of nitrogen concentration can be measured or is known in advance. Unfortunately, attempts to determine the nitrogen concentration experimentally, by measuring a thermodynamic property such as specific heat or viscosity, were not successful. For the energy meter algorithm to work well, the value of the nitrogen concentration must be determined in an indirect manner.

A method for inferentially determining the nitrogen concentration, called the two-state method, was described by Morrow et al. [2000], but not pursued at that time. If the nine parameters in Equations (2.1) and (2.2) are evaluated at two different thermodynamic states, then two independent sets of equations are available for calculating the molecular weight as a function of speed of sound, carbon dioxide concentration, and nitrogen concentration. The molecular weight is not a function of temperature and pressure, so the two independent equations of the form of Equation (2.1) can be set equal to each other and solved for the nitrogen concentration.

The two-state method was set aside in 2000 because of concerns that random errors in speed of sound at the two thermodynamic states would produce erroneous results for nitrogen concentration. The method was revived in 2002 with the additional requirement that the same speed of sound instrument be used for the sound speed measurements at both states. It was reasoned that errors due to imprecise measurement of the distance between ultrasound source and target would be the same at both states. An error of this type would be a “bias” error, and would be correlated among measurements. While random uncorrelated errors in sound speed would remain a source of error, correlated biases were shown to pose a less severe problem.

An evaluation showed that the two-state method was relatively insensitive to a bias error of 0.1% in sound speed if the same error was applied to measurements at both states (i.e., if the sound speed measurement, at both states, was performed with the same sensor). The method was also shown to be more accurate when sound speed was determined at two different pressures, than at two different temperatures. After a review of the interpolation scheme, it was determined that it might be possible to improve the accuracy of nitrogen estimation by reducing the magnitude of the temperature and pressure steps in the interpolation scheme. New interpolation tables were produced in which the size of temperature increments was reduced from 10°F to 2°F and the size of the pressure increments was reduced from 50 psia to 12.5 psia.

Preliminary results of the two-state algorithm are shown in Table 2-1. To test the algorithm, values of speed of sound were computed with AGA-8 for a preselected gas composition at several different pressures and temperatures. The first and second columns list the values of pressure and temperature used for simulated measurements at State 1. The third and fourth columns list the values of pressure and temperature used for State 2. The fifth column lists the value of nitrogen concentration calculated by the two-state method, using the computed values of speed of sound and exact value of carbon dioxide concentration for the hypothetical gas. The exact value of the nitrogen concentration in the hypothetical test gas is 0.64675 mol%. The desired accuracy of the inferred nitrogen value is ± 0.05 mol% or better.

Table 2-1. Calculated results for nitrogen concentration from the two-state method.

State 1		State 2		N_2 Concentration
Pressure (psia)	Temperature (^oF)	Pressure (psia)	Temperature (^oF)	(mol%)
30	80	90	80	0.656
90	80	150	80	0.680
30	75	90	75	0.679
90	75	150	75	0.642
30	70	90	70	0.662
90	70	150	70	0.681
60	70	60	80	0.245
60	80	60	90	-0.879
30	70	90	75	0.680
90	75	150	80	0.635

Note that when the temperatures at States 1 and 2 are the same and the pressures differ, the calculated results are within acceptable accuracy. When both temperature and pressure vary, the results are also acceptable. However, when the pressure is held constant and the temperatures vary, the results lie outside the acceptable accuracy range.

2.2.1 Optimum Differences between States 1 and 2

Further calculations were made to determine the optimum difference in pressures or temperatures required for the two-state method. Figure 2-1 shows the results. An initial thermodynamic state corresponding to a pressure of 90 psia and temperature of 75ºF was selected. Computations of nitrogen concentration were made for a series of second states ranging from 60 psia to 110 psia in pressure, and at temperatures of 70ºF and 72ºF. The calculated value of nitrogen concentration approached the desired uncertainty interval for both second-state temperatures when the second pressure was less than or equal to 80 psia, i.e., the pressure at State 2 was at least 10 psi less than the State 1 pressure.

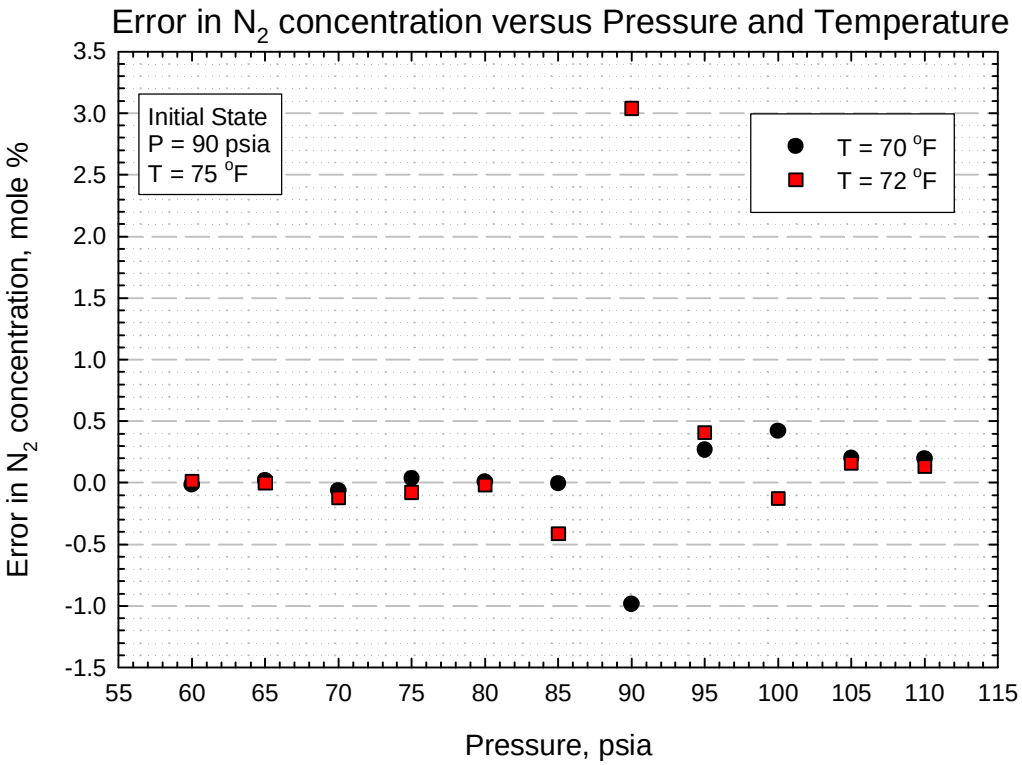

Figure 2-1. Initial analysis of error in nitrogen concentration for the two-state method, as a function of pressure and temperature difference between initial and final states.

The two-state computer program was then modified to facilitate a parametric analysis (the efficient calculation of nitrogen concentration at numerous pressures and temperatures). This allowed an expanded view of the accuracy of the method by including differences in first and second state pressures ranging from 20 to 200 psia. The state temperatures were also expanded to include differences in first and second state temperatures ranging from 50 to 90ºF.

The parametric analysis showed that the two-state method provided a stable determination of nitrogen concentration if the two states differ by at least 25 psi, regardless of the temperature. In addition, a nominally constant bias in nitrogen of +0.10 mol% (even when the second state pressure differed from the first state pressure by at least 25 psi) can be observed. If this bias is independent of gas composition, or if the bias exhibits a predictable trend as gas composition changes, it may be possible to adjust the output, essentially eliminating the bias, to provide a value for nitrogen concentration that meets the allowable measurement error limit of ± 0.05 mol%. Figure 2-2 shows the behavior of the two-state method for a typical natural gas blend with 1.00 mol% nitrogen and 1.00 mol% carbon dioxide over a pressure range of 20 to 200 psia and a temperature range of 70 to 90ºF.

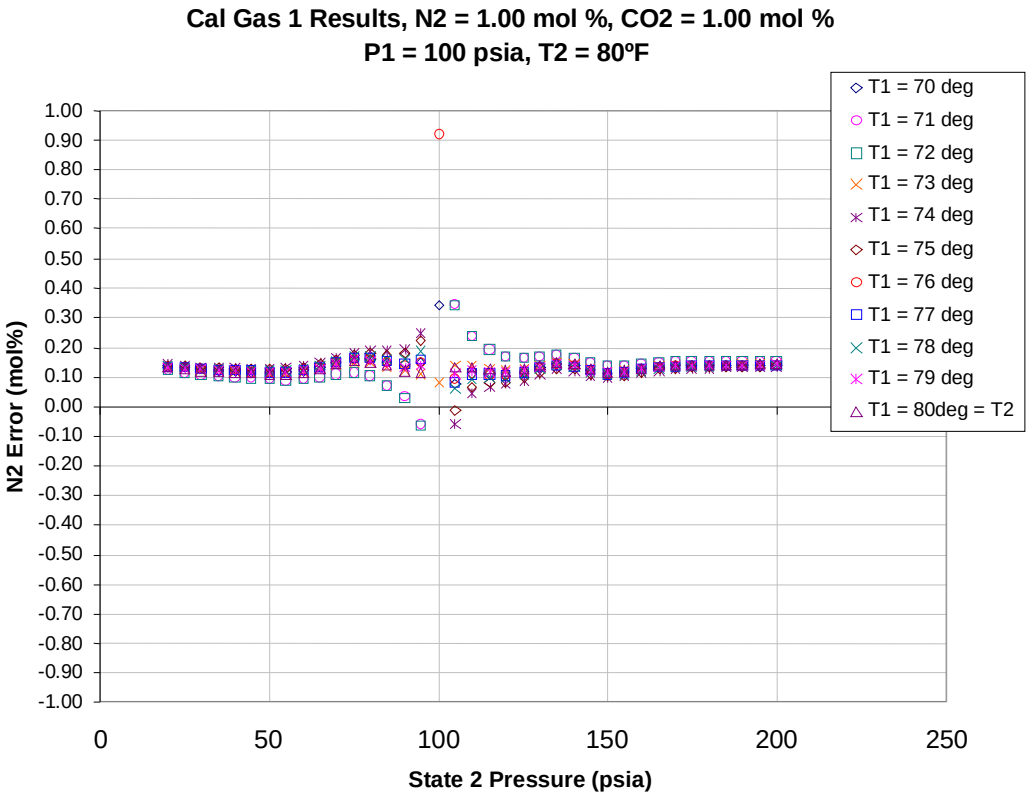

Figure 2-2. Parametric analysis of error in nitrogen concentration for the two-state method, as a function of pressure and temperature difference between initial and final states.

Next, the error analysis of the two-state method was performed using other gas compositions, specifically a reference database containing 86 gas mixtures. These reference gas compositions ranged in heating value from 950 to 1180 Btu/scf, with a maximum nitrogen concentration of 13.47 mol% and a maximum carbon dioxide concentration of 7.59 mol%. In the previous analysis, the two-state method demonstrated a consistent accuracy in nitrogen content for a wide pressure and temperature range, as long as the pressure differential between the two states was maintained at a minimum of 25 psi. Since the effect of state conditions had already been tested, the two thermodynamic state conditions in the present analysis were fixed at:

- State 1: P1 = 100 psia, T1 = 79ºF
- State 2: P2 = 70 psia, T2 = 80ºF

These state conditions were chosen in order to provide inferential nitrogen values independent of algorithm errors related to insufficient separation between pressure states.

Figure 2-3 shows the errors in inferred nitrogen content for the 86 gas compositions as a function of the gas heating value. The predicted nitrogen error is not constant, as might be expected from the previous results obtained using only two gas compositions. The method

showed reasonably good results for nitrogen concentration over the range of compositions. However, variation in the error was dependent on several factors and was not directly associated with the heating value, which makes it more difficult to correct as originally intended. The nine reference gases used to develop the algorithm interpolation tables are shown in bright green in the plot. Inferred values of nitrogen content for these gases demonstrated an error of ±0.05 mol%. The Amarillo, Gulf Coast, Ekofisk, and 100 mol% methane gas are shown as triangles of different colors. (These four gas compositions were used to validate the performance of AGA-8 (American Gas Association [1994] and AGA-10 (American Gas Association [2003].) The error in nitrogen for these four typical transmission gas compositions is ±0.065 mol%.

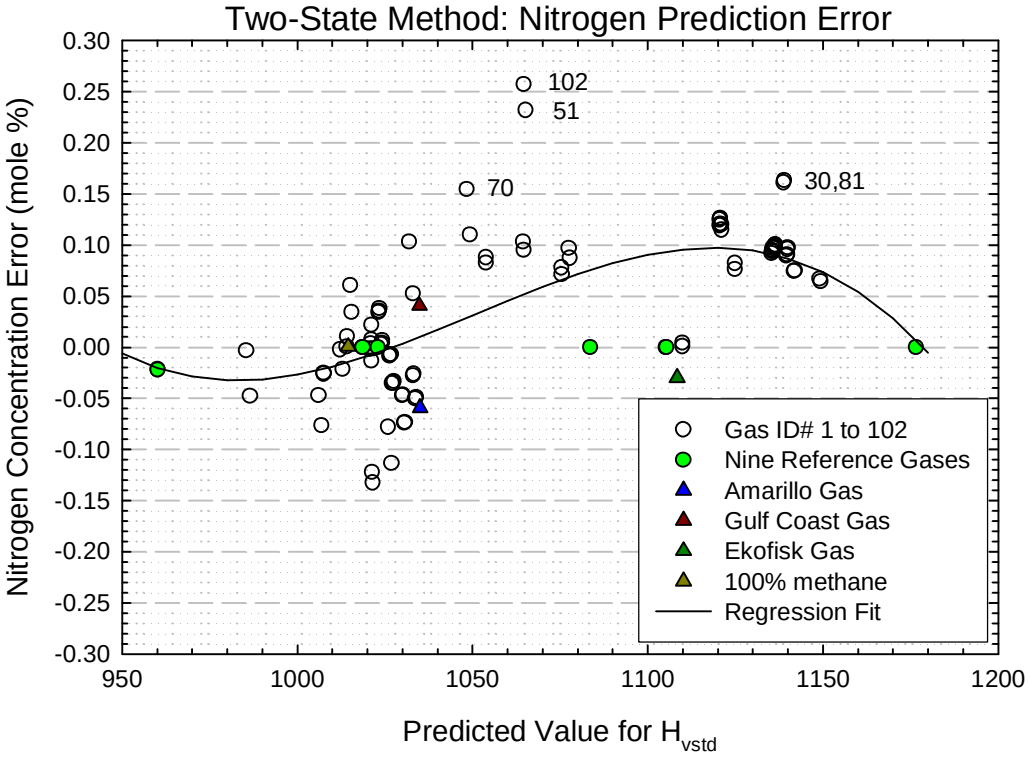

Figure 2-3. Errors in nitrogen concentration computed by the two-state method for a database of 86 gases.

For all of the gases, the average error in nitrogen concentration was 0.041 mol%, with a standard deviation of 0.077 mol%. It should be noted that the labeled points with Gas ID numbers of 30, 51, 70, 81, and 102 have compositions atypical of transmission gases, with either higher amounts of heavier hydrocarbon constituents relative to methane, or higher amounts of diluents (above 3.0 mol%).

Figure 2-3 also shows a cubic regression correlation for the derived nitrogen concentration using the standard heating value as the independent variable. This correlation could be applied to the nitrogen concentration determined from the two-state method in order to reduce the errors in the outlying points (such as Gas ID numbers 102 and 51). The correction would lower the

average error for the 86 gas compositions to 0.0052 mol%, with a standard deviation of 0.0541 mol%. Applying this correlation causes a slight increase in the nitrogen error for the nine reference gases.

2.2.2 Sensitivity to Errors in Sound Speed and CO_2 Concentration

An analysis of the two-state method's sensitivity to speed of sound and carbon dioxide measurement errors was also performed. The results are shown in Figure 2-4 through Figure 2-6 for different input errors. The analysis used a typical blend of natural gas, with approximately 95 mol% methane, 1.0 mol% nitrogen and 1.0 mol% carbon dioxide. The State 1 pressure was held fixed at 100 psia and the State 2 temperature was held at 80ºF. State 2 pressure was varied from 20 psia to 200 psia while State 1 temperature was varied from 70°F to 90ºF.

Figure 2-4 shows the error in nitrogen concentration predicted by the two-state method with no errors in the measurement of speed of sound or carbon dioxide content. The figure shows the importance of allowing at least 25-30 psia difference between the two thermodynamic states. When the State 2 pressure is less than 75 psia or greater than 125 psia, the error stabilizes at around a 0.10 mol% offset.

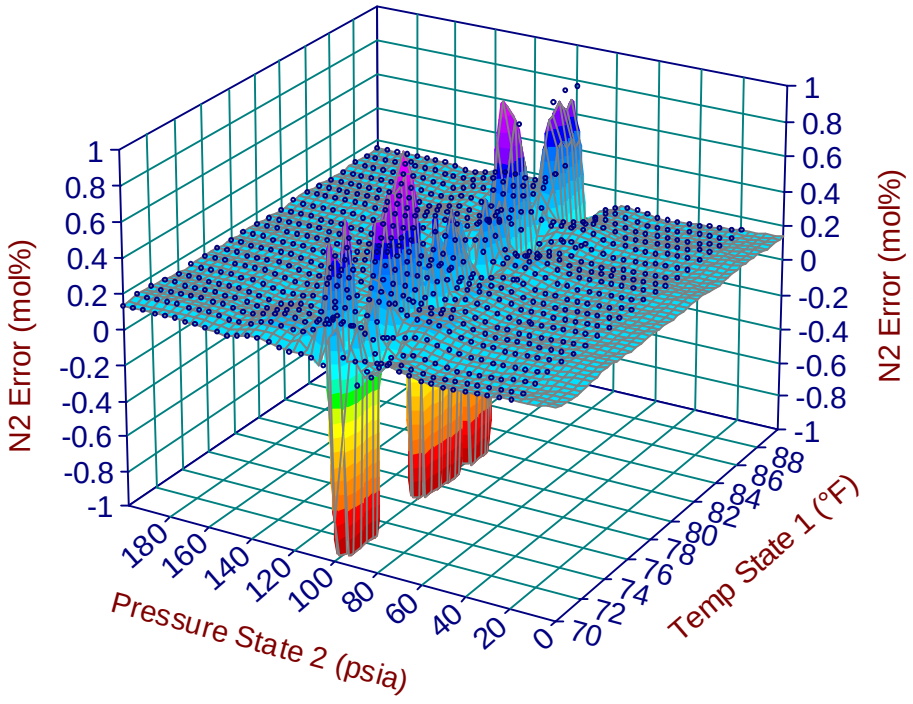

Figure 2-4. Error in nitrogen determination for a typical transmission grade natural gas mixture using the two-state method, assuming no errors in the input speed of sound and carbon dioxide content measurements.

In a field application, the error in the speed of sound measurement is expected to vary between ± 0.50 and ± 1.5 ft/sec, and the error in the measured carbon dioxide content is expected to be less than ± 0.05 mol%. In order to estimate the resulting accuracy in calculated nitrogen, calculations were made using an assumed error in the speed of sound of ± 1.0 ft/sec and an error in carbon dioxide of ± 0.03 mol%. Figure 2-5 and Figure 2-6 show the differences in the predicted nitrogen error when these errors are either both positive or both negative. When the states differ by at least 25 psi, the error in nitrogen appears to vary between +0.20 to +0.30 mol% when both input errors are negative. In contrast, when both input errors are positive the nitrogen error is between -0.05 and +0.05 mol%. These results help to characterize the likely practical error in the method, using the current version of the algorithm.

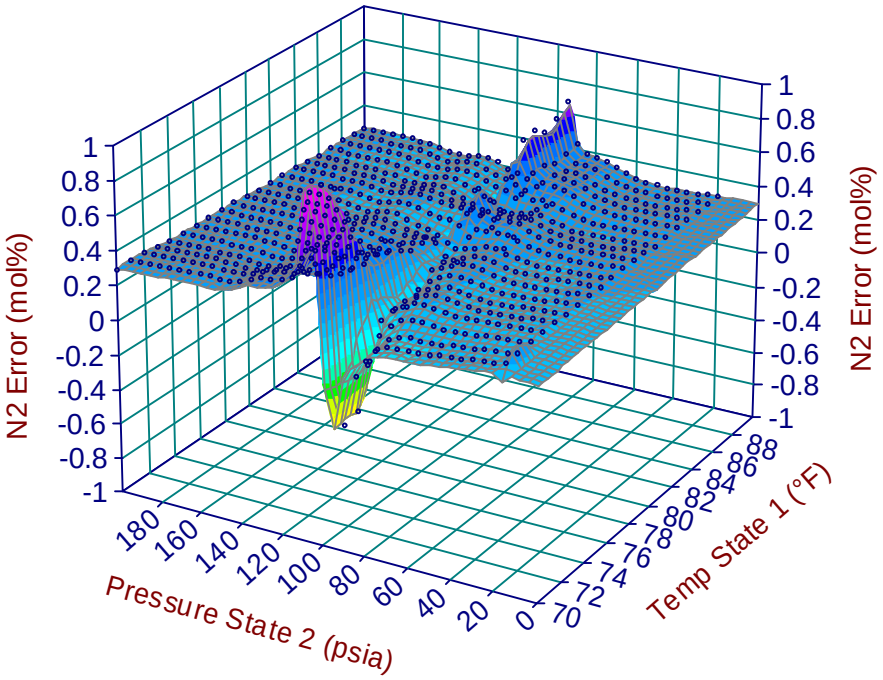

Figure 2-5. Error in nitrogen determination using the two-state method, assuming a sound speed measurement error of -1.0 ft/sec and a CO_2 measurement error of -0.03 mol%.

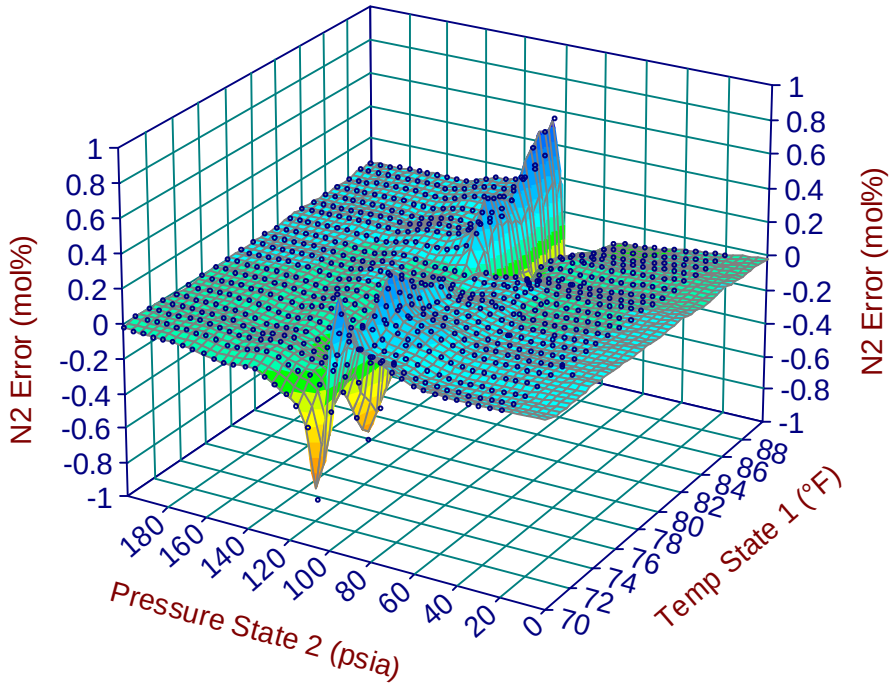

Figure 2-6. Error in nitrogen determination using the two-state method, assuming a sound speed measurement error of +1.0 ft/sec and a CO_2 measurement error of +0.03 mol%.

2.3 TWO-STATE ALGORITHM IMPROVEMENTS

An improved version of the two-state algorithm was developed to reduce the uncertainties associated with the reference gas database interpolation process. For this purpose, the AGA-8 equation of state (American Gas Association [1994]) was embedded directly in the algorithm. Instead of using AGA-8 pre-calculated values stored in the algorithm interpolation table, the AGA-8 equation of state was used to directly calculate sound speed as a function of temperature and pressure at each state for the selected reference gases.

It was also decided to once again use a gas database to generate the parameters in the model equations for molecular weight and density. Two sets of reference gases were evaluated for use in the inferential algorithm least squares regression fit. Version 1 used the full set of 86 natural gas mixtures initially used to determine the optimum pressure difference between states. Version 2 used a subset of 22 natural gas mixtures selected from the full set. The results were similar for both versions. For the calculations, the two thermodynamic states were selected as State 1 = 100 psia, 80ºF and State 2 = 50 psia, 80ºF. To evaluate the error in nitrogen calculation, results were calculated for all of the 86 gas mixtures in the reference database, which ranged in heating value from 960-1170 Btu/scf.

Both versions compared favorably to the previous two-state computer code, with reduced errors both in the calculated nitrogen concentration and in the calculated standard heating value. Figure 2-7 shows a plot of the error in nitrogen concentration using the reduced database of 22 independent gas mixtures to calculate the regression coefficients at both states. The nitrogen mean error and standard deviation were decreased to +0.0018 mol% and 0.0512 mol%, respectively, compared to the earlier version of the two-state method. The magnitude of the nitrogen concentration error is less than 0.05 mol% for 68 of the 86 gas mixtures (79% of all gases tested).

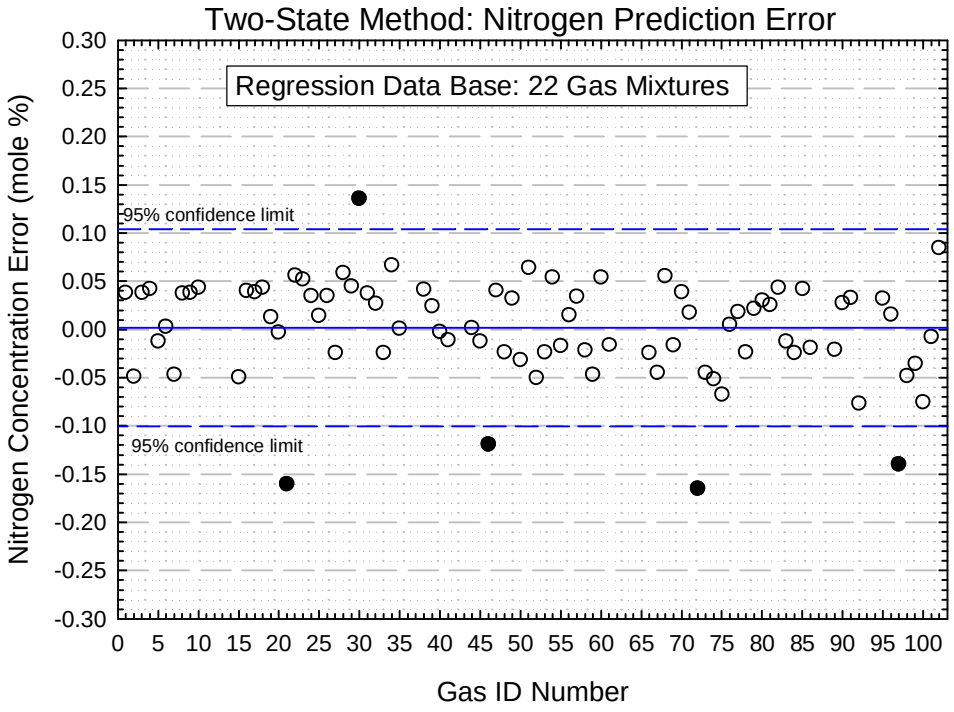

Figure 2-7. Error in computed N_2 from the two state method using the improved algorithm.

Figure 2-8 shows a similar plot of the results for heating value using the version of the algorithm with 22 independent gas mixtures. Heating value was calculated in the algorithm using correlations based upon the standard speed of sound, the carbon dioxide concentration, and the values of nitrogen concentration calculated from the two-state method. The mean error in heating value was +0.59 Btu/scf. The standard deviation in heating value error was 0.75 Btu/scf. The 95% confidence interval in standard heating value error extends from -0.94 Btu/scf to +2.16 Btu/scf. If a correction for the mean error were applied to all values, the 95% confidence interval in heating value would be ± 1.5 Btu/scf.

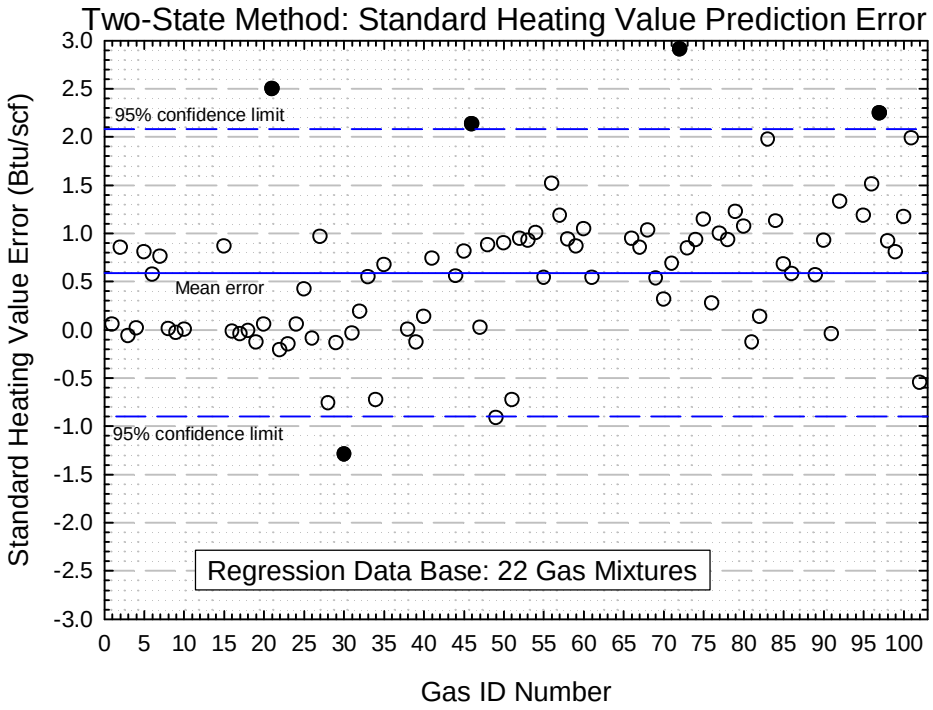

Figure 2-8. Error in standard heating value from the two state method, using the improved two-state algorithm to calculate nitrogen concentration.

The results show that the algorithm accuracy can be improved through the use of a least squares regression fit in calculating the correlation coefficients from the reference gas database. The improved accuracy for the two-state method determination of nitrogen content results from improvements in predicted molecular weight.

2.4 UPGRADE TO AGA-10 EQUATION OF STATE

A surprising result was obtained when sensitivity tests were performed on the improved two-state algorithm that used the AGA-8 equation of state, as implemented by the SUPERZ code distributed upon the release of AGA-8. The results of the sensitivity tests showed larger than acceptable errors both in nitrogen concentration and in heating value. The source of these errors was traced to differences in values of speed of sound calculated by SonicWare (used to calculate input values of sound speed for the sensitivity tests) and SUPERZ (used to calculate the input values of sound speed for the results shown in Figure 2-3). Subsequent tests showed a small difference in calculated speed of sound (a bias error) between SUPERZ and SonicWare that varied as a function of pressure. SonicWare is known to include changes to the AGA-8 algorithm published in 1994 (the publication date of the SUPERZ code is 1986).

The two-state energy meter algorithm was rewritten to incorporate the most recent standard for sound speed calculation, AGA-10 (American Gas Association [2003]). Tests with the modified algorithm were then performed to investigate the effects of precision uncertainties in

sound speed ranging in magnitude from 0.01 to 1 ft/s. Values of sound speed for a chosen gas were calculated using either the AGA-10 computer code or SonicWare. (Values of sound speed calculated using SonicWare were shown to agree with AGA-10, to within the limit of 50 ppm specified for compliance with AGA-10.) The calculated values were recorded to six decimal places, then rounded to the nearest 0.001 ft/s, 0.01 ft/s, 0.1 ft/s, and 1.0 ft/s and input to the algorithm. The resulting errors in computed nitrogen concentration were recorded as a function of the precision in the sound speed values. Best results were found when the error in the input speed of sound was less than ± 0.1 ft/s.

2.5 MULTIPLE-STATES METHODS

One further modification of the two-state method was also evaluated. Independent laboratory tests indicated that in practice, a raw signal acquisition rate of 250 MHz would be required to obtain ±0.1 ft/s accuracy in measured sound speed from the two-state nitrogen determination method. Because this data acquisition rate is impractical to achieve, two complementary methods were developed using the 50 MHz acquisition rate existing in the sound speed electronics. The first method improves the resolution of sound speed by interpolating along a polynomial fitted to the ultrasonic signal cross-correlation function. This method can be implemented within a data logger instead of within the sound speed electronics, allowing the method to be optimized more easily.

The second method is based upon the generally accepted practice of making replicate, independent measurements of a quantity to reduce the uncertainty in the mean value of all the samples. That is, instead of measuring the speed of sound, pressure and temperature at only two thermodynamic states, the number of states can be increased to a larger number. Under this approach, measurements of sound speed at two states give one measurement pair for the two-state method (State 1 and State 2), while three states give three measurement pairs (State 1 and State 2, State 1 and State 3, State 2 and State 3). Similarly, four states give six measurement pairs; five states give ten pairs measurement pairs; six states give 15 measurement pairs; and seven states give 21 measurement pairs. The effect of increasing the number of states would be to reduce the precision uncertainty in the mean value of sound speed by approximately the square root of the number of measurement pairs. As an example, it was found that sound speed measurements at 0.1 ft/s accuracy, taken at 25 psi intervals between 50 psia and 200 psia, would produce values of nitrogen content accurate to within 0.005 mol% and heating values accurate to within 0.7 Btu/scf. It was decided that measurements would be taken at a total of seven different pressures over the pressure range allowed by the current chamber design.

At this point, it was concluded that no further algorithm development was necessary within the project scope of work. It appeared that the multiple-states method, together with an interpolation procedure for improving the accuracy of the sound speed measurement, would permit the inferential determination of nitrogen concentration consistent with the project accuracy goals.

This page is intentionally blank.

3. SPEED OF SOUND SENSOR

3.1 PROTOTYPE ULTRASONIC TRANSDUCER

Design improvements were identified in 2001 for improving and upgrading the performance of the prototype ultrasonic transducer used in the speed of sound sensor. This prototype transducer was used in the laboratory tests of the energy meter module presented in Section 6.0 to gain early information on the environmental performance of the current energy meter module configuration, as well as to further evaluate the low temperature performance of the speed of sound sensor and its ultrasonic transducer. Although the performance of the speed of sound sensor was adequate for conducting the laboratory tests, the Etalon Model CIA-3525-SB2 266-kHz prototype ultrasonic transducer exhibited certain operating deficiencies that confirmed the need for the planned improvements and provided more specific information for defining the needed improvements. In this respect, the transducer was first found to have a non-uniform radiation beam pattern which resulted in unbalanced illumination of the two reflecting faces in the speed of sound test chamber. This problem, discovered after experiencing difficulties with the cold temperature environmental tests, caused the pulse reflection from the second, more distant reflector face to be higher in amplitude than that from the first reflector. Bench tests on the speed of sound sensor revealed that this non-uniformity made the ultrasonic reflections dependent on the angular position at which the transducer was installed in the test chamber. Figure 3-1 shows one of several bench test measurements of the prototype transducer radiation beam cross-section, recorded to quantitatively evaluate the problem.

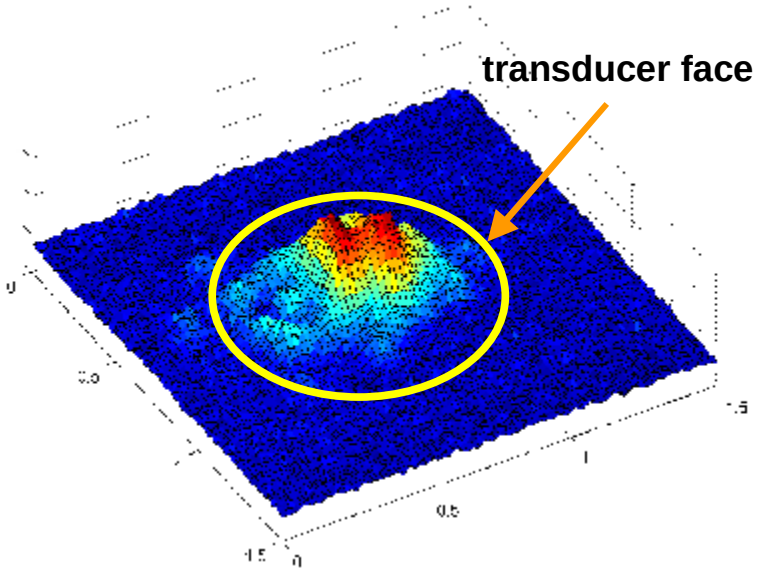

Figure 3-1. Sound radiation amplitude cross-section of the Etalon Model CIA-3525-SB2 prototype ultrasonic transducer beam pattern, measured three inches in front of the transducer face (tested in air at room temperature and pressure).

This discrepancy was not observed during any of the speed of sound sensor tests performed in 2001, apparently because the angular orientation of the transducer in the speed of sound test chamber was such that approximately equal parts of the active transducer beam were incident on the two reflecting faces. Furthermore, the unbalanced illumination problem did not introduce errors in the ultrasonic pulse travel times or in the measured speed of sound at room temperature or at higher temperatures. Additional bench tests were performed to confirm the angular orientation sensitivity in the speed of sound chamber and to identify and restore the transducer to its most favorable orientation for further energy meter module testing.

The prototype ultrasonic transducer was found to have an additional low temperature discrepancy (discussed in Section 6.2) in which the amplitude and number of oscillatory cycles in the pulse gradually increased as the operating temperature was lowered below room temperature. This effect corresponds to a reduction in spectral bandwidth and an attendant increase in transducer transmitting sensitivity (i.e., an increase in transducer Q). This effect is suspected to be associated with a temperature-dependent change in the elastic modulus of the epoxy fill material used in the composite ultrasonic transducer fabrication and possibly in other polymer bonding materials used at the element mounting perimeter in the transducer housing. The increase in number of cycles in the two reflected pulses degrades the ability of the speed of sound signal processing technique to accurately discriminate the true coherence peak in the cross correlation function from adjacent correlation peaks located at approximately one oscillation period before and after the true peak. This lack of discrimination can cause 'cycle skipping' errors in the indicated speed of sound. However, for testing purposes, these low temperature effects on the ultrasonic pulse waveforms were not totally disruptive since, by careful inspection of sample ultrasonic pulse waveforms recorded during the tests, the cycle-skip errors could be identified and corrected in the data analysis. The experience gained from these evaluation tests has led to well-defined temperature requirements for the improved ultrasonic transducer design.

3.2 NEW ULTRASONIC TRANSDUCER

The scope of work planned for upgrading the ultrasonic transducer in 2002-2003 included the procurement of an improved version of the Etalon Model CIA-3525-SB2 prototype transducer as a step toward optimizing the operation of the energy meter speed of sound sensor. The deficiencies of the prototype transducer described above provided important additional evidence for seeking these improvements. Therefore, based upon the transducer bench tests performed in 2001-2002 and the laboratory tests performed in 2002-2003, specifications were developed for a new custom-designed ultrasonic transducer, as follows.

New Transducer Technical Specifications:

Active face diameter:	1.0 inch.
Transducer housing:	1.25 in. OD x 1.25 in. L, with 1.375 in. OD flange on rear.
Center frequency:	400 kHz.
Bandwidth (-6 dB):	Minimum > 75 % of center frequency. Goal of 100 % of center frequency.
Pulse waveform:	Three cycles of center frequency, or less, in time duration with trailing oscillations at least 90% below pulse peak amplitude.
Gas coupling:	Efficient acoustic coupling into gaseous media at 50 psia and higher pressures.
Sensitivity:	Maximum practical source-receiver sensitivity (minimum sensitivity: +20 dB S/N for pulse reflections from rigid planar reflector in 50 psia air placed 2.5 in. from transducer face).
Beam uniformity:	±5% or less variation in amplitude over active face.
Face alignment:	Planar active face aligned within ±0.5 degrees perpendicular to housing axis.
Pressure rating:	Pressure-equalized transducer housing with active element exposed to pressure on front and back surfaces (maximum operating pressure: 2,500 psia).
Temperature rating:	Operating temperature range of 0°F to 140°F.

This list of technical specifications was submitted to Etalon Corporation and to Ultran Laboratories, Inc. for quotations. The transducer operational functions associated with the energy meter speed of sound measurements were described to both manufacturers via telephone discussions to ensure accurate understanding of the requirements. Etalon Corp. responded with a bid to develop the specified transducer device. Ultran proposed the use of a modified 500 kHz off-the-shelf transducer similar to the Ultran Model NCT-505 device previously tested in the speed of sound sensor in 2001 and found to be unsatisfactory. Prior to placing an order with Etalon, SwRI project personnel visited Etalon Corp. in Lebanon, IN to further discuss the transducer requirements and to explain the anticipated market opportunities related to future commercialization of the natural gas energy meter and related benefits that could accrue from the new transducer development.

The new transducer design pursued by Etalon was a departure from the previous 266 kHz transducer design, in that it was aimed at gaining increased operating bandwidth by increasing the center frequency and by improving the impedance match between the relatively high mechanical impedance of the active transducer face and the relatively low acoustic impedance of the gas. Southwest Research Institute assisted in the early stages of this design effort by providing detailed information on the acoustic impedance of transmission-grade natural gas over the specified range of operating pressures and temperatures. The essential features of the transducer design were described by Etalon as consisting of a rectilinearly diced type-2 composite piezoelectric disk made of lead zirconate titanate piezoceramic material, with the diced grooves filled with epoxy material selected for its stable physical properties when exposed

to the specified range of operating temperatures. After fabricating the filled composite structure, the face surface was lapped to a smooth surface finish and was coated with a thin layer of low acoustic impedance material selected to provide a proper acoustic match between the transducer material and natural gas at 50 psia pressure. The thickness of this matching layer was adjusted experimentally to provide the best attainable ultrasonic pulse signal waveform when tested in air at room temperature and pressure.

The new transducer produced by Etalon was delivered to SwRI in December 2003 for acceptance testing. The basic performance characteristics of the new unit were listed by Etalon as follows:

- Active face diameter: 1.0 inch
- Housing design: As specified
- Center frequency: 357 kHz
- Bandwidth (- 6 dB): 56 kHz (16 % of center frequency).

On receiving the new transducer, SwRI personnel first tested it in the laboratory to determine the uniformity of its radiation beam pattern. This test showed the transducer to have a uniform and axially symmetrical sound radiation pattern. The transducer was then installed in the speed of sound test chamber for tests in a natural gas mixture consisting of 85 mol% methane, 5.8 mol% ethane, and 5.5 mol% carbon dioxide at pressures ranging from 15 psia to 100 psia at room temperature (the speed of sound of the gas at 75 psia was 1,361.8 ft/sec). These tests were performed using a Matec Model TB1000 ISA ultrasonic transceiver system operating at excitation frequencies in the range of 250 kHz to 450 kHz with various pulse durations ranging from 0.1 μsec to 1.6 μsec.

Tests in the speed of sound chamber showed the two reflected waveforms to have excessive ringing effects consisting of more than 20 oscillatory cycles each, causing the pulse waveform received from the near reflection face to extend nearly to the initiation time of the reflection received from the second reflector face (a time extent of about 50 μsec). The frequency spectrum of this pulse was centered at approximately 350 kHz and had an effective bandwidth of approximately 60 kHz, corresponding to 17 percent of the spectrum center frequency. The narrowness of this spectrum and several strong spectral amplitude variations were responsible for the ringing effects in the pulse waveforms. The new transducer and the associated speed of sound sensor electronics system were unable to derive an accurate value of the time difference between the reflected pulses because of correlation cycle skipping errors related to the narrow bandwidth.

On the basis of the pulse waveform tests described above, the new transducer was found to be unacceptable for use in the energy meter module. The test results were communicated to Etalon Corporation, and the transducer was returned for redesign or cancellation of the order without performing any additional acceptance testing.

3.2.1 Ultran Labs 500-kHz Transducer

An Ultran Labs Model NCT-55 500-kHz stock-item ultrasonic transducer was purchased as a possible alternative to the poorly performing Etalon second-generation transducer. Bench tests of the Ultran 500 kHz transducer using both tone-burst excitation and spike-impulse excitation revealed that it had excessive oscillatory ringing response, and was ineffective in providing an accurate value of the time difference between the two reflected pulses because of correlation cycle skipping errors.

3.2.2 Ultran Labs 1-MHz Transducer

An Ultran Labs Model NCT-510 1-MHz ultrasonic transducer, previously purchased and tested in 2001, was re-evaluated under controlled bench test conditions using the newly developed 2002-2003 speed of sound test chamber and electronics system. These tests were performed using tone-burst excitation signals at frequencies of 600 kHz and 1.2 MHz. The most favorable results were obtained at 1.2 MHz because of the transducer's 1-MHz natural resonance frequency response. Because the tone-burst electronics system was not capable of being incrementally tuned to the transducer center frequency of 1.06 MHz, a 'spike-impulse' ultrasonic transmitter circuit having a peak impulse voltage of 180 V-pk and rise time of 4 nsec was used to drive the transducer at its impulse resonance response frequency. This mode of excitation demonstrated that the transducer had a pulse-echo bandwidth of 293 kHz and was capable of producing acceptable sound speed measurements in rich and lean natural gas mixtures at pressures above about 70 psia.

Figure 3-2 shows the pulse-echo response versus pressure as obtained using the Ultran 1-MHz transducer excited by the spike-impulse transmitter in two certified natural gas mixtures. The transducer responses were recorded using 64-waveform averaging to gain usable signal-to-noise ratios for accurate speed of sound analysis. The composition of the two gases, designated as test gas A and test gas D, are listed in Table 3-1. The two reflected pulses in each trace are very similar in shape, having approximately three oscillatory cycles (approx. 3 μsec time duration). However, the relative amplitudes of the first and second reflections in each trace are significantly different because of differences in viscous absorption by the gas of the 1-MHz ultrasonic pulse signals over the differential reflector spacing, $\Delta D = 0.500$ in., and differences in the acoustic impedance match between the transducer and the two gas compositions. In particular, the attenuation rate in test gas A is significantly higher than that in test gas D, as indicated in Table 3-2 at test pressures of 65 psia and 100 psia. From these estimated attenuation rates, the approximate pulse-echo transmission coefficient at the transducer face is 0.255 for test gas A and 0.368 for test gas D, corresponding to a specific acoustic impedance of about 20 kRayl at the matching layer surface on the transducer face.

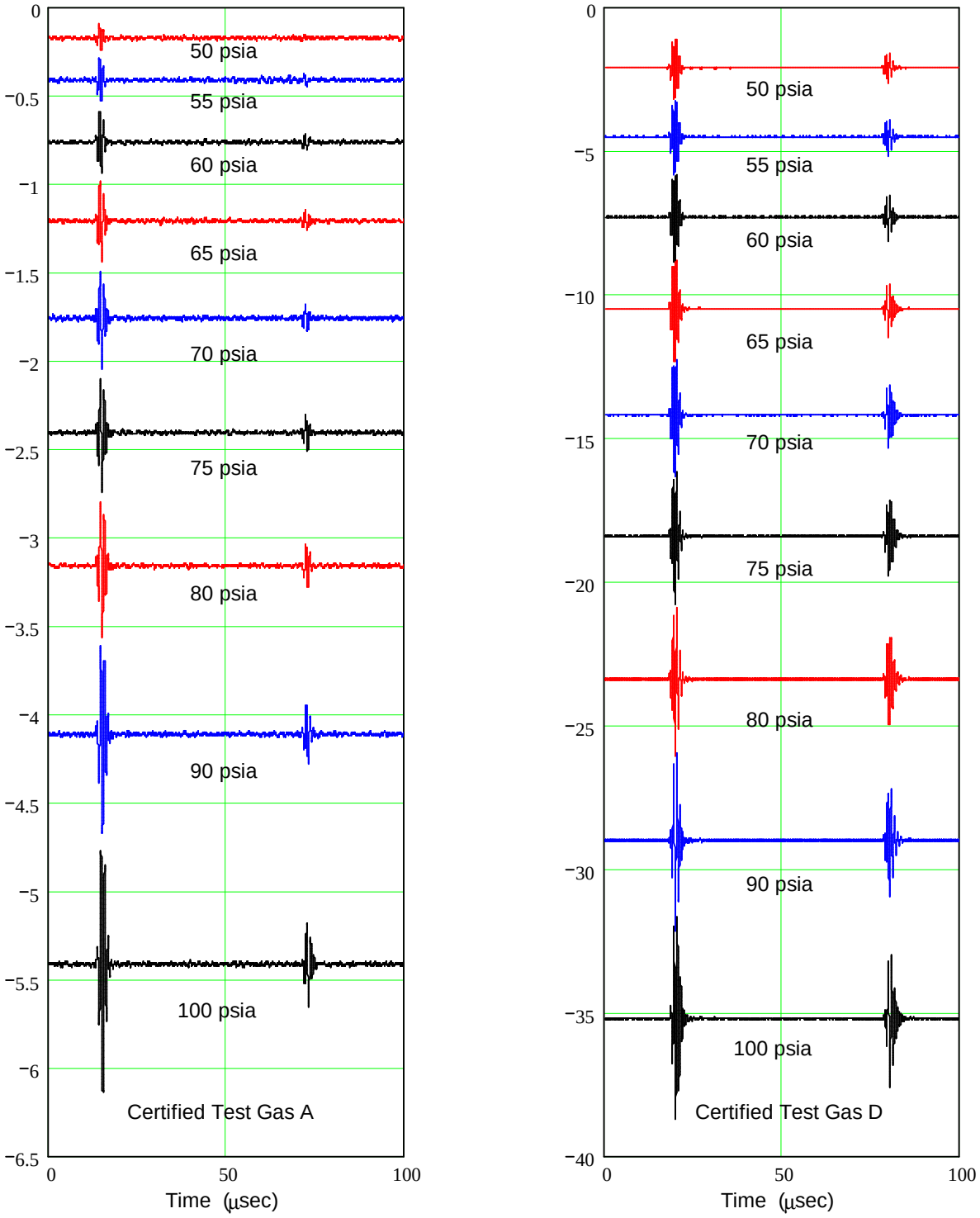

Figure 3-2. Examples of pulse-echo reflection waveforms obtained using the Ultran NCT-510 1-MHz ultrasonic transducer in test gas A and test gas D (T » 73°F).

Table 3-1. Compositions of certified test gases A and D.

Gas Constituent	Concentration – Gas A (mol%)	Concentration – Gas D (mol%)
Methane	96.6500	90.0811
Ethane	1.0200	6.6200
Propane	0.3100	1.1200
Isobutane	0.0000	0.0960
n-Butane	0.0000	0.0940
Isopentane	0.0000	0.0495
n-Pentane	0.0000	0.0990
n-Hexane	0.0000	0.0200
n-Heptane	0.0000	0.0201
n-Octane	0.0000	0.0103
Nitrogen	1.0000	1.2900
Carbon Dioxide	1.0200	0.5000
TOTAL	100.0000	100.0000

Table 3-2. Approximate pulse-echo attenuation rate for 1-MHz pulse signals in test gas A and test gas D (T » 73°F).

Gas Pressure (psia)	1-MHz Attenuation Rate Test Gas A (dB/in.)	1-MHz Attenuation Rate Test Gas D (dB/in.)
65	12.07	5.68
100	9.39	3.93

Figure 3-3(a) shows the separate frequency spectra of the two reflected signals in the relatively low attenuation test gas D. The differences in these spectra illustrate the small loss of high frequency content in the second reflection compared with that of the first reflection caused by viscous absorption along the slightly longer travel path. Figure 3-3(b) shows the calculated cross correlation function for the two reflected pulse waveforms.

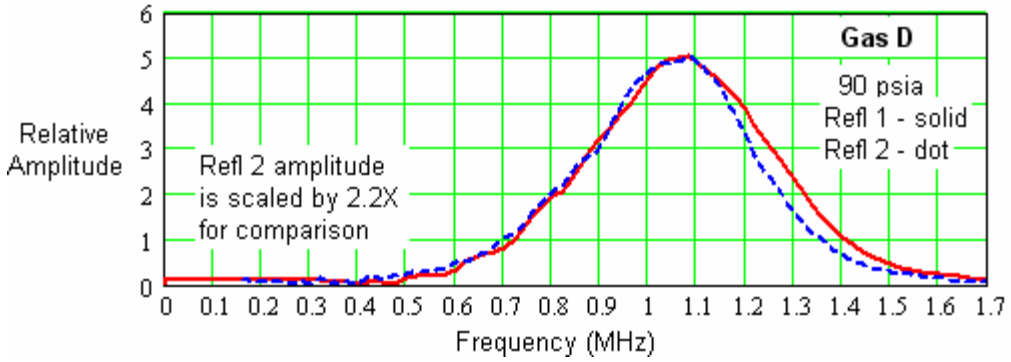

(a) Frequency spectra

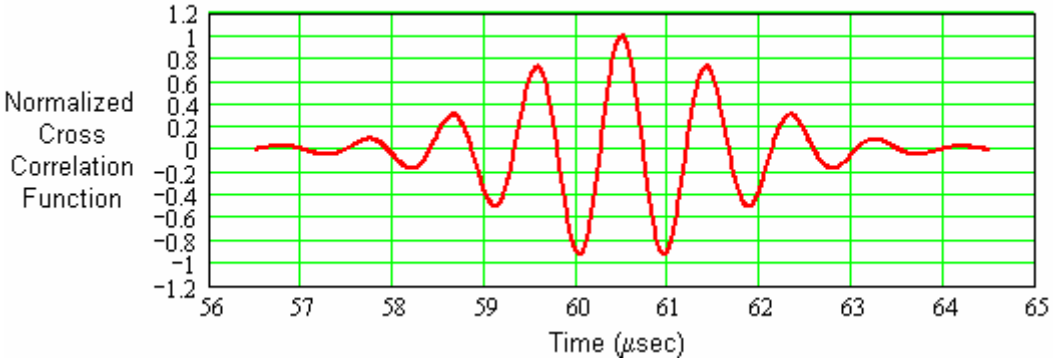

(b) Cross correlation function

Figure 3-3. Frequency spectra and cross correlation function for 1-MHz pulse reflections in test gas D at P = 90 psia, T = 75°F.

With the use of spike-impulse excitation, the effective performance of the Ultran Labs Model NCT-510 transducer, although higher in operating frequency than specified in the Etalon second-generation design, was considered to be potentially acceptable for use in the prototype speed of sound sensor system. Bench test data acquired during this evaluation was also used in later signal processing model studies to develop software methods for improving the accuracy and resolution of the time difference derived from the cross correlation function and the signal-to-noise ratio of the ultrasonic signals.

3.3 SPEED OF SOUND SENSOR ELECTRONICS

The speed of sound sensor electronics system is contained on a single circuit board that generates and processes, by dedicated firmware, ultrasonic signals for deriving the speed of sound in the test gas contained in the sound speed sensor test chamber. This system excites and receives ultrasonic reflection signals from the ultrasonic transducer and dual reflector target, digitizes and stores the reflection waveform data, determines the speed of sound from the

measured travel time from the known reflector targets, and transfers output information through serial ports to either a remote computer or digital display. Power for the circuits is derived from a 24-VDC, 1-ampere power supply. Figure 3-4 shows a block diagram of the sensor electronics system.

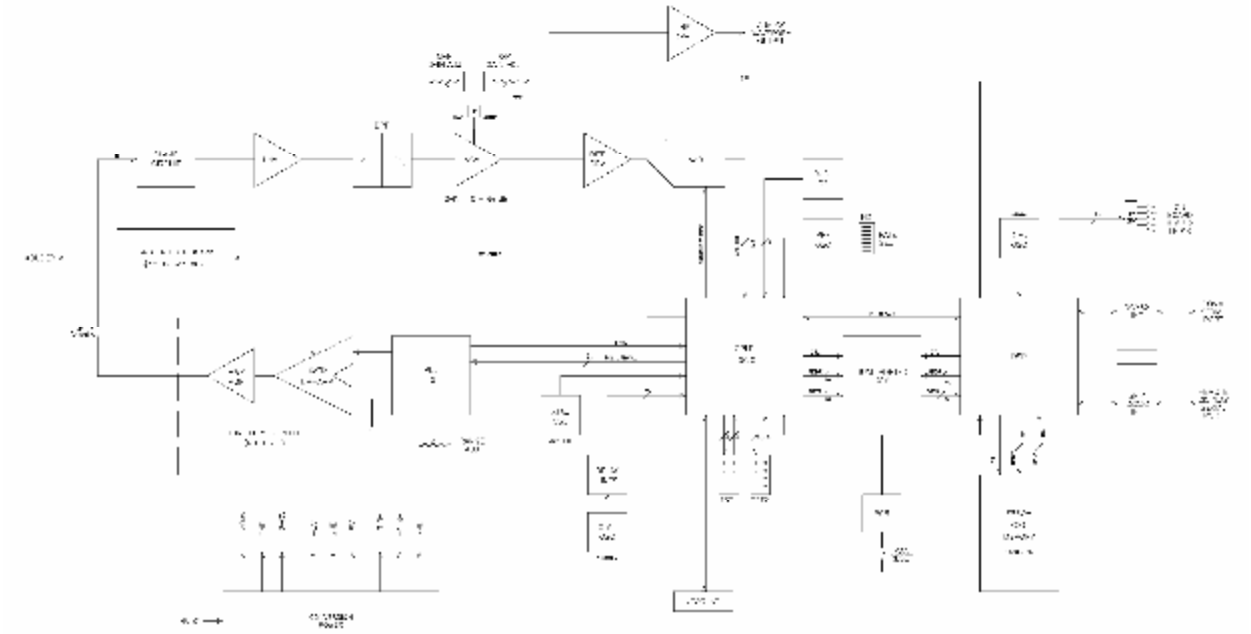

Figure 3-4. Block diagram of the speed of sound electronics system.

3.3.1 Tone-Burst Generator

Excitation of the ultrasonic transducer is performed by several circuit elements that combine to generate a high-voltage sinusoidal pulse signal, programmable to have one or two oscillatory cycles starting and ending at zero crossings. The elements of this tone-burst generator include a phase-locked loop function generator (PLL FG), crystal oscillator (XTAL OSC) reference for the PLL FG, switched operational oscillator (SW'D OP-AMP), and a power amplifier (PWR AMP), in addition to associated logic contained in a complex programmable logic device (CPLD).

In operation, the PLL FG generates a sinusoidal signal phase-locked to the XTAL OSC frequency. The XTAL OSC signal is fed to the CPLD, enabling it to be divided in binary increments either by reprogramming the CPLD or inserting jumpers in header pins of TST2 as listed in Table 3-3 for selecting the ultrasonic tone-burst frequency. The PLL FG also provides a sync pulse to mark the zero-crossing point of each sinusoidal cycle.

Table 3-3. Jumper assignments at header TST2.

Description	Pins 1-2	Pins 3-4	Pins 5-6	Pins7-8
PLL FG Ref. Freq.				
150 kHz	Open	Short		
300 kHz	Short	Open		
600 kHz	Open	Open		
1200 kHz	Short	Short		
High-Voltage Power Supply				
Enable				Short
Disable				Open

The CPLD counts the zero-crossing sync pulses to determine when to switch the output of the SW'D OP AMP to zero, thereby gating only the selected number of sine wave cycles to the PWR AMP. Zero-crossing counts begin at the positive edge of the pulse-repetition oscillator (PRF OSC) signal and stop the tone burst when the selected number of zero crossings is completed. Normally, the pulse repetition rate is set at either 20 or 40 pps as determined by jumper-selected binary control of the PRF OSC. The PWR AMP amplifies the low-level tone-burst signal to approximately 350 V-pp to drive the transducer. The PLL FG circuit changes the output tone-burst frequency to a very low value following the transmitted tone-burst to reduce cross-feed of the residual sine wave signal into the receiver while reflection signals are being received. Changing to the lower frequency shifts the offending signal out of the receiver passband.

3.3.2 Waveform Receiver

For each tone burst pulse applied to the transducer, a reflected signal is returned to the transducer from the dual-reflector target and converted to a low-level analog signal. This analog signal is first amplified by a low-noise preamplifier (LNA), passed through active high-pass and low-pass filters forming a band-pass filter (BPF), and then amplified further by an adjustable-gain amplifier (VGA), to produce a signal level suitable for digitization. The amplified analog signal is also fed to a remote line driver (LINE DRV) output terminal to allow the received signal to be displayed or recorded by an oscilloscope. Since the receiver is connected directly to the transducer and PWR AMP output, the high-voltage excitation pulse also appears at the receiver LNA input. To avoid damage to the LNA, the receiver input is protected by the CLAMP CIRCUIT. The CLAMP CIRCUIT limits the LNA input signal to a safe receiver operating level.

The BPF is made up of two independent filter modules. One module is designed for high-pass operation and the other for low-pass operation. Each module is on a separate small circuit board that plugs into the main circuit board to allow replacement if other filter characteristics are needed. The BPF is normally designed to pass the frequency spectrum of the ultrasonic pulse signal and attenuate other signals and noise outside of the passband. The VGA can provide up to

80 dB additional signal amplification, as governed either by a manual gain control or by a digitally controlled potentiometer (DCP). A digital signal processor is designed to provide serial peripheral interface (SPI) communications to the DCP for gain control. Selection of either manual or DSP gain control is by jumper on the circuit board. The SPI gain control function is not currently programmed into the DSP, necessitating that only manual gain control be used in the present prototype speed of sound sensor system.

3.3.3 Waveform Digitizer

Digitization of the reflected waveforms is accomplished by an analog-to-digital converter (A/D) driven from a differential amplifier and clocked at the sampling frequency by logic control in the same programmable device (CPLD) that generates the sampling frequency from the XTAL OSC operating at 100 MHz. The VGA signal is first converted from a single-ended signal to a differential signal required by the A/D. The A/D converter produces a 12-bit digital representation of the analog signal which is fed to the CPLD at the selected sampling rate (presently set at 50 MSamples/sec). The CPLD then transfers the digitized signal to one port of a dual-port memory. A DELAY LINE circuit between the 100-MHz XTAL OSC and the CPLD facilitates proper synchronization of the memory-write control signals with the digitized data signals.

When enabled by the DSP, the A/D converter digitizes the waveform and the digitized signal is delayed by 80 μsec after the start of the next PRF cycle. Waveform digitization then continues for a receiving period of 640 μsec. This waveform data string is written to the dual-port memory. The digital signal delay and receiving period are determined by logic timers in the CPLD and are in-circuit programmable.

3.3.4 Dual-Port Memory

The dual-port memory is used to collect and store the 12-bit received waveform data. Digitized data from the CPLD is written to one port and read by the DSP via the alternate port. The memory is capable of storing up to 64,000 18-bit words but only 12 bits are used. When waveform acquisition is complete, the CPLD logic sets an interrupt flag in the DSP to alert the DSP that a new waveform is available in memory and is ready for DSP acquisition. No new waveform data will be written to memory until the DSP reads the data and notifies the CPLD by setting a flag indicating that a new waveform may be digitized and stored. With this mode of control, the pulse repetition of the ultrasonic analog system may occur, without consequence, at a higher rate than the rate at which the DSP actually reads the acquired waveforms.

3.3.5 Digital Signal Processor

The DSP acquires digital waveform data from the dual-port memory when available and alerts the CPLD when waveform acquisition is complete. The DSP then performs the following functions:

1. Averages sixteen repetitive waveforms;
2. Determines the approximate sample point representing the leading edge of the first reflection signal;
3. Applies cross correlation analysis to compute the lag-time delay, Δt, of the second reflection signal;
4. Computes the speed of sound, v_G, in the test gas using the cross correlation lag time delay between the two reflected waveforms and a stored value of the differential distance, ΔD, between the two reflecting targets;
5. Transfers the speed of sound information using MODBUS protocol to the COMM SERIAL PORT via the RS232 interface for transfer to a remote computer;
6. Transfers the speed of sound information to a remote numerical display via a second serial interface (SPI/RS232 INT) (this function is not presently implemented in the DSP software);
7. Controls the VGA gain through a local on-board SPI dedicated to automatically adjusting the digital potentiometer (this function is not presently implemented in the DSP software).

The DSP program is initiated by an electronically programmable memory (EPROM). This non-volatile memory is 128kB by 8B in size and contains the program-execute instructions. The execute instructions are read immediately following a power-up reset (POR) or manual reset command (via remote push-button switch connected to header H3).

3.3.6 CPLD Logic

Logic required for circuit timing and control is provided in a single complex programmable logic device (CPLD) as described above. This device can be reprogrammed via an on-board standard Joint Test Action Group (JTAG) interface port. Certain circuit operating parameters can be changed, such as the number of cycles in the tone burst signal and the tone-burst repetition frequency. Changing the tone-burst repetition frequency is accomplished by readjusting the PLL FG range potentiometer. For diagnostic purposes, internal signals within the CPLD are fed to the test pins on header TST1. The designated diagnostic signals currently assigned to the pins on TST1 are listed in Table 3-4.

Table 3-4. Pin assignments on header TST1.

Pin	Description
1	Unassigned
2	Unassigned
3	Unassigned
4	Unassigned
5	TBKILL
6	PF7 (data-available interrupt to DSP)
7	F12 (data-acquired flag from DSP)
8	CHA (sync)

3.3.7 Spike-Impulse Transducer Excitation

A supplemental mode of operation to excite the ultrasonic transducer at its impulse resonance was devised using a two-stage capacitor discharge circuit controlled by SCR switching to provide a negative voltage impulse having an impulsive voltage of 180 V-pk, a leading-edge rise time of 4 nsec, and a trailing decay time duration of 160 nsec. This circuit is fabricated as a separate electronics module and requires a +100VDC power supply and +15 VDC for proper operation. Figure 3-5 shows the spike-impulse transmitter circuit diagram and an oscilloscope trace illustrating the generated impulse signal when terminated by a 50-ohm resistive load.

The spike-impulse transmitter circuit may be operated at pulse repetition rates up to about 3 kpps. However, in the present prototype speed of sound sensor, trigger pulses at a programmed rate of 40 pps are derived from the speed of sound sensor electronics circuit board (TP10). When the circuit is activated to generate spike-impulse excitation of the ultrasonic transducer, the tone-burst transmitter on the main circuit board is deactivated by disabling its high-voltage power supply by jumper control at pins 7-8 on header TST2.

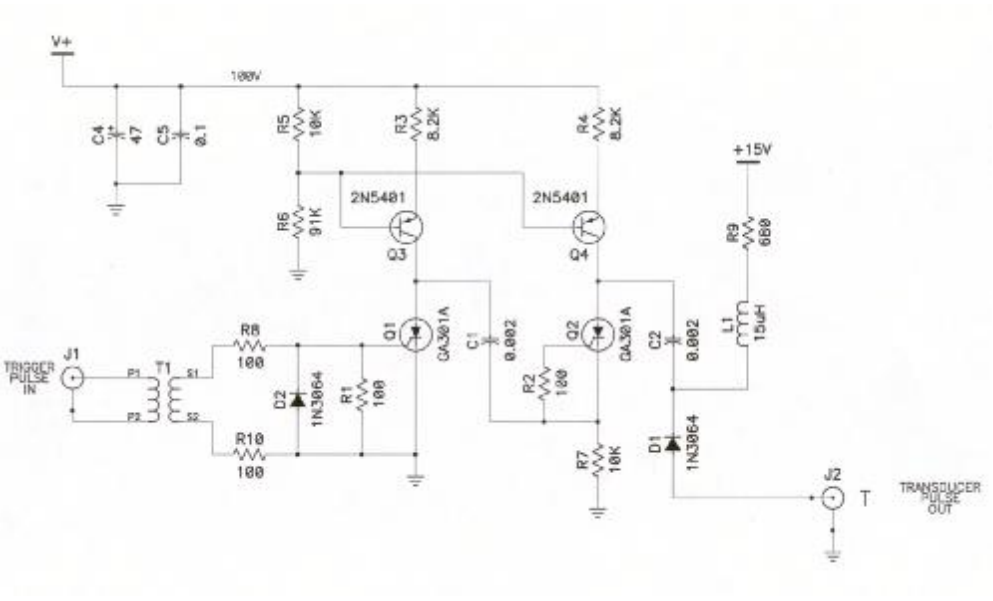

(a) Spike-impulse transmitter circuit diagram

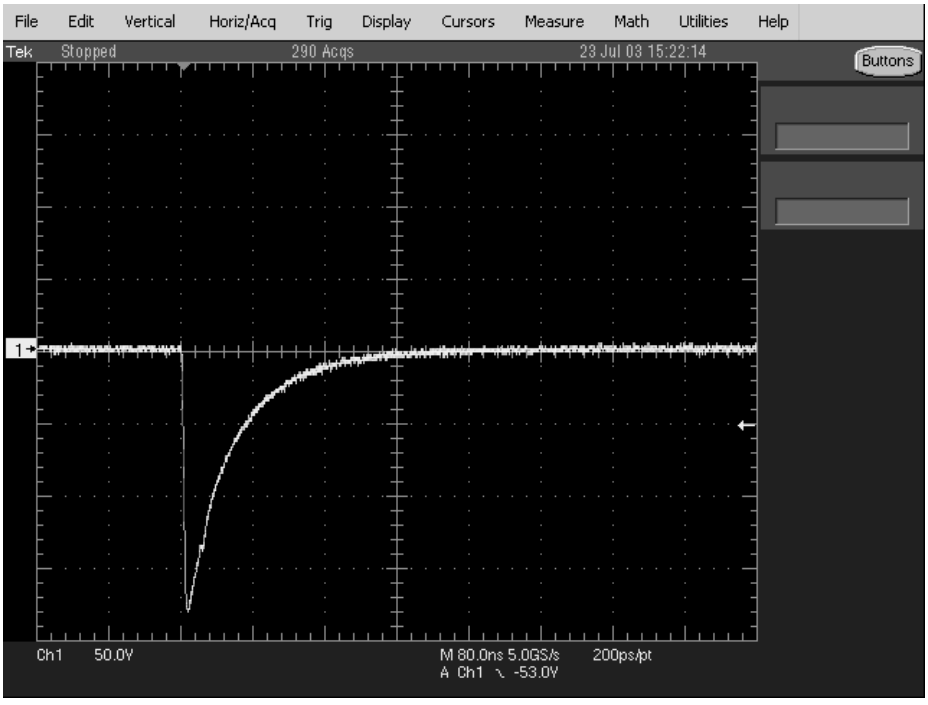

(b) Output pulse into 50-ohm resistive load

Figure 3-5. Spike-impulse transmitter circuit diagram and oscilloscope trace of circuit output pulse.

3.4 SPEED OF SOUND SIGNAL PROCESSING

3.4.1 Background and New Requirements

The target accuracy for inferential determination of the standard volumetric heating value of processed natural gas for custody transfer is ΔH_v = ±1 Btu/scf. Sensitivity studies of the inferential algorithm in 2001 demonstrated that the following accuracy tolerances in input parameters would produce the target accuracy in heating value:

- Pressure: ± 0.20 psia
- Temperature: ± 0.20°F
- Speed of Sound: ± 0.88 ft/sec
- CO_2 Concentration: ± 0.05 mol%
- N_2 Concentration: ± 0.05 mol%.

As discussed in Section 2, in the absence of a sensor for directly determining nitrogen concentration in natural gas, a viable alternative is to merge the determination of nitrogen with the determination of the gas molecular weight and standard volumetric heating value in an expanded multiple-state inferential analysis. Although this approach eliminates the need for a nitrogen sensor, it requires that the remaining four input parameters be measured at two or more independent thermodynamic states. Furthermore, a quantitative assessment of this approach indicated that the accuracy and resolution of the speed of sound parameter must be upgraded significantly from the realizable value of Δv_G = ± 0.88 ft/s demonstrated in 2001 to a new requirement of Δv_G = ± 0.1 ft/s or better. If this measurement accuracy can be successfully achieved, the two-state inferential analysis has the potential to provide two principal outputs: (1) nitrogen concentration with an accuracy of ± 0.05 mol%; and (2) standard volumetric heating value with an accuracy of ± 1 Btu/scf.

As reported by Kelner *et al.* [2004], the uncertainties in sound speed measurement may be separated into two categories: (1) accuracy considerations, and (2) instrumentation resolution considerations. That work identified and evaluated several intrinsic second-order error effects associated with time-of-flight measurements in gases, including velocity dispersion caused by viscous attenuation and molecular relaxation that could potentially affect the precision of the measured difference in time of flight between the two reflections and, hence, introduce errors in the derived speed of sound. Phase delays associated with diffraction effects in the near field of the ultrasonic transducer were also analyzed. These were found to be relatively small, and largely cancel when the times of flight of the two reflections are subtracted. Moreover, any residual phase-related time delay error is fixed when the ultrasonic operating frequency is specified and, therefore, will be compensated for when the speed of sound sensor is calibrated using a test gas having an accurately known composition and sound speed at the calibration test conditions.

The molecular relaxation dispersion errors, i.e., speed of sound dependency on frequency and pressure, were pointed out to be largely dominated by the dispersion effects associated with the high concentration of methane in natural gas. Therefore, based on the dispersive frequency-pressure relationship for methane, when the sensor is operated at a fixed frequency within a bounded pressure range where the velocity dispersion effects are approximately constant versus pressure, the dispersion will have the same small second-order distortional effect on the ultrasonic waveforms but will be approximately independent of pressure. In this case, the effects of molecular relaxation can also be expected to be approximately compensated for when the sound speed sensor is calibrated. Calibration is accomplished by operating the sensor using a test gas having a known composition and a known speed of sound, v_{Gc}, at the sensor test conditions to experimentally determine the time difference, Δt_c, between the two ultrasonic reflections and adjusting the effective reference value of the reflector spacing to be $\Delta D_c = v_{Gc} \cdot \Delta t_c$ for use in analyzing other test gases.

Resolution errors in the derived speed of sound are dependent on the sampling frequency used to convert the analog ultrasonic waveforms to digital form, combined with any temperature drift in the digital clock that sets the sampling frequency, plus any thermal variations in the distance between the two reflecting target faces. For example, when the digitized waveforms are recognized as discrete time signals having a time resolution of $\delta(\Delta t) = \pm 1/f_s$, the calibrated velocity relationship becomes

$$v_G = \frac{2\,\Delta D_c}{\Delta t \pm \dfrac{1}{f_S}} \tag{3-1}$$

where f_s = digital sampling frequency. Since any uncertainties in the parameters determining v_G are independent of one another, the RMS fractional error in sound speed is

$$\frac{dv_G}{v_G} \approx \sqrt{\left(\frac{d(\Delta D_c)}{\Delta D_c}\right)^2 + \left(\frac{d(\Delta t)}{\Delta t}\right)^2 + \left(\frac{d\ f_S}{\Delta t\ f_S{}^2}\right)^2}\ . \tag{3-2}$$

By design, the temperature sensitivity of the sensor system is minimized by using materials and circuit components having negligible or compensated temperature dependence, making the thermal errors $\delta(\Delta D_c)$ and δf_s negligible. Hence, the fractional error in sound speed depends primarily on the numerical time resolution imposed by the digital sampling frequency as expressed by

$$\frac{d\,v_G}{v_G} \approx \pm \frac{1}{\Delta t\ f_S}\,. \tag{3-3}$$

For typical sound speed values of 1,400 ft/sec, the time difference between the two reflections for ΔD_c = 0.500 in. is Δt = 59.500 μsec, resulting in the discrete numerical resolution limits shown in Table 3-5 below.

Table 3-5. Typical numerical resolution of speed of sound sensor system.

Sampling Frequency (MSamples/sec)	δv_G for v_G = 1,400 ft/sec (ft/sec)
25	± 0.933
50	± 0.467
100	± 0.233
200	± 0.167
250	± 0.093

Therefore, to obtain sound speed resolution of less than δv_G = ± 0.100 ft/sec, the sampling frequency must be increased to about 250 MSamples/sec. Although attainable, this sampling frequency is impractical in most industrial electronics applications because of system complexities, reduced sample word size (amplitude resolution), and cost. Nevertheless, on the basis of making the sampling rate as high as practical, the prototype electronics system designed in 2002 was made capable of providing either 25 or 50 MSamples/sec, with the experimental system adjusted to operate at 25 MSamples/sec in accordance with the sound speed resolution projected in the 2001 inferential algorithm studies related to single-state sensor measurements. This operating sampling rate was increased to 50 MSamples/sec in 2003 to provide improved resolution in the prototype sensor for tests related to two-state sensor measurements. From these tests, the 12-bit, 50-MSample/sec A-to-D conversion section of the prototype electronics system was demonstrated to be practical and cost effective for use in the speed of sound sensor.

A practical alternative to increasing the sound speed resolution by increasing the digital sampling rate to 250 MSamples/sec is to introduce a method by which the sample points at, say, 50 MSamples/sec are interpolated to yield appropriate intermediate values between the electronically sampled data points. The most flexible and advantageous approach to this requirement is to apply the interpolation process to the cross correlation function, with its predictable analytical features, rather than to apply it to the raw data represented by the recorded ultrasonic waveforms.

3.4.2 Accuracy and Resolution Considerations

An unavoidable link between sound speed accuracy and data resolution not addressed above is the effect of random noise in the sensor system. Noise superimposed on the ultrasonic waveforms perturbs the true sampled values represented in the waveforms, and those perturbations are propagated through the signal processing steps to appear as noise-induced errors in the derived time delay between the two reflection waveforms. With sound speed resolution limits on the order of 70 ppm now required, the effects of noise interference were evaluated during 2002-2003. This was done by modeling the overall speed of sound sensor operation with random noise interference added to experimental examples of the ultrasonic waveforms. This approach allowed the signal-to-noise ratio of the measured ultrasonic waveforms to be included in the assessment of parameters affecting the performance of the sound speed sensor. To examine the impact of signal-to-noise ratio on sound speed accuracy, the

modeling process was first revised to provide the desired resolution in the time difference between reflections before investigating the effects of noisy ultrasonic waveforms.

3.4.3 Time-of-Flight Interpolation

A statistically determined interpolation of the time shift corresponding to the maximum value of the cross correlation coherence lobe may be obtained by fitting a second-degree polynomial, i.e., a parabola, to the sample points comprising the positive lobe of the cross correlation function. Figure 3-6 shows the cross correlation function between two 1-MHz ultrasonic reflections recorded at a pressure of 100.35 psia and a temperature of 75.55°F in test gas D. For consistent results in interpolating the coherence maximum lag-time, Δt, in different test gases, the cross correlation function is normalized to its maximum amplitude as resolved by its discrete sample points.

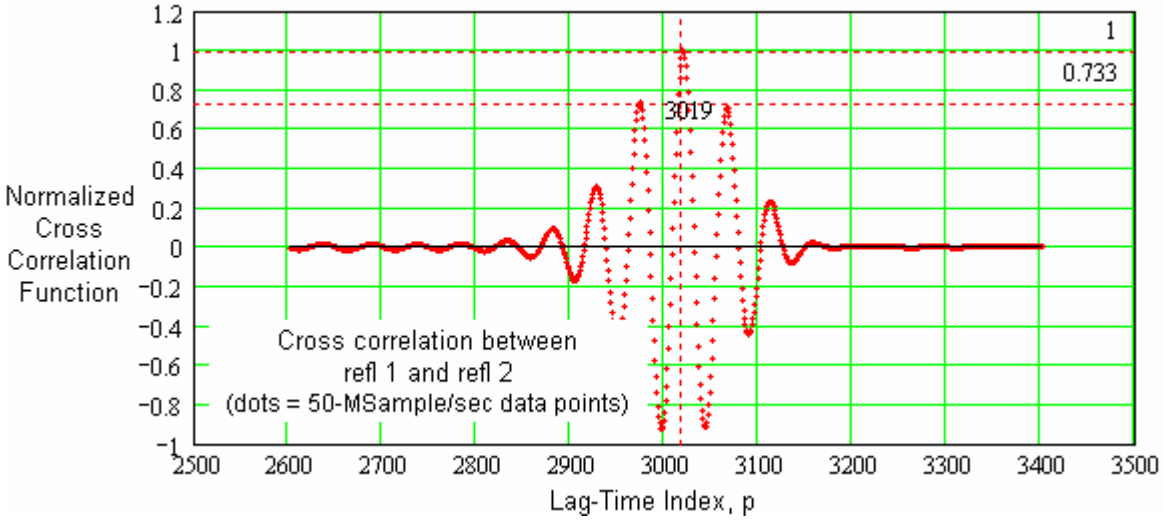

Figure 3-6. Cross correlation between reflected ultrasonic waveforms recorded in test gas D at P = 100.35 psia and T = 75.55°F.

Test gas D was a relatively low attenuation gas at the 1-MHz ultrasonic operating frequency and was selected for use in the interpolation analysis because of its high signal-to-noise ratio. Using the AGA-10 equation of state, the calculated reference speed of sound in test gas D for the indicated pressure and temperature conditions was calculated to be 1,377.325 ft/sec.

The lag-time shift at the sample point closest to the coherence maximum, $p_{max} = 3019$, is

$$\Delta T = \frac{p_{\max}}{f_S} = 60.40\ m\,\mathrm{sec}\,. \tag{3-4}$$

The corresponding speed of sound, for $2 \cdot \Delta D_c = 1.000$ inch, is

$$v_{gasD} = \frac{2\Delta D_c \cdot \left(1/12\right)}{\Delta T} = 1379.691 \text{ ft/sec}. \tag{3-5}$$

Values of p_{max} increased or decreased by 1 lead to the resolution limit imposed by the 50-MSample/sec signal sampling rate (± 0.457 ft/sec). However, a more accurate coherence maximum point exists between lag-time points p_{max} and p_{max} ± 1. This maximum coherence point may be found by a curve-fit interpolation applied to the positive coherence lobe of the correlation function.

Figure 3-7 shows an expanded view of the positive sample points defining the correlation coherence lobe. There are 23 positive-valued sample points in the example correlation derived from waveforms recorded at 50 MSamples/sec (possibly up to 24 positive points can occur in other waveform examples). The cross correlation function is symmetrical about the coherence maximum and, although it has an exact analytical expression involving trigonometric functions related to the ultrasonic waveform frequency and bandwidth, its isolated positive coherence lobe can be represented with good accuracy by a generalized parabola of the form

$$f(t) = a_1 + a_2 t + a_3 t^2. \tag{3-6}$$

Alternatively, using the relation, $\tau = p/f_s$, this function may be expressed in terms of the correlation lag-time sample-point index, p , as

$$f(p) = a_1 + a_2 p + a_3 p^2. \tag{3-7}$$

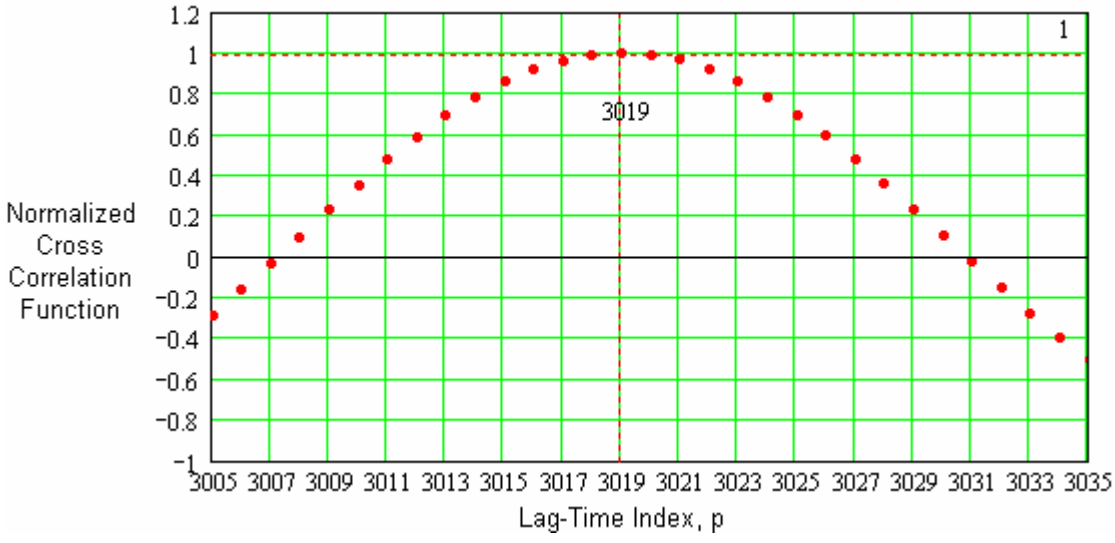

Figure 3-7. Expanded view of positive lobe of normalized cross correlation function.

This second-degree polynomial is amenable to accurate curve fitting using the method of least squares, implemented using the least squares normal equations. With this direct

arithmetical method, the residuals between an optimally fitted analytical parabolic curve and the corresponding points to which it is fitted are minimized, resulting in a unique "most probable" fit to the data. In the present application, the symmetry of the correlation function about the true coherence maximum point ensures that the τ- or *p*-axis coordinate of the vertex of the fitted parabola will accurately coincide with the most probable coherence maximum lag-time coordinate (i.e., the coherence lobe vertex) even though the amplitude values of the cross correlation function and the fitted parabola at the vertex coordinate may not be equal.

The normal equations required to solve for the parabola coefficients, a_1, a_2, a_3, in Equation (3-7) are

$$\begin{aligned} A_1 a_1 + B_1 a_2 + C_1 a_3 &= D_1 \\ A_2 a_1 + B_2 a_2 + C_2 a_3 &= D_2 \\ A_3 a_1 + B_3 a_2 + C_3 a_3 &= D_3 \end{aligned} \tag{3-8}$$

where:

Coordinate terms, A_n, B_n, C_n, and ordinate values, D_n, for n = 1, 2, 3 in Equation (3-8) are:

$$A_1 = \sum_{j=J1}^{J2} 1 \qquad B_1 = \sum_{j=J1}^{J2} j \qquad C_1 = \sum_{j=J1}^{J2} j^2 \qquad D_1 = \sum_{j=J1}^{J2} f(j)$$

$$A_2 = B_1 \qquad B_2 = C_1 \qquad C_2 = \sum_{j=J1}^{J2} j^3 \qquad D_2 = \sum_{j=J1}^{J2} f(j) \cdot j$$

$$A_3 = C_1 \qquad B_3 = C_2 \qquad C_3 = \sum_{j=J1}^{J2} j^4 \qquad D_3 = \sum_{j=J1}^{J2} f(j) \cdot j^2$$

Index j = 1 . . . 23 corresponds to the lag-time coordinate index, p, over the positive values of the coherence lobe; and

J1 . . . J2 = the range of points used in the data fitting process.

The data point values representing the cross correlation function are such that the normal equations will be subject to excessive numerical round-off errors. As noted above, the values of the abscissa are large ($p \sim 3000$) and appear in factors raised to the fourth power whereas values of the ordinate are less than unity and appear at only first power. This numerical unbalance may be eliminated by shifting the cross correlation data points nearer to the abscissa origin to avoid the numerically large magnitude values during the curve fitting calculations and then translating the result back to the original abscissa position. That is, the 23 positive data points of interest are identified and shifted to begin at the origin using a new index, *j*. The actual number of points, *J*1 . . *J*2, used in the curve fit is made selectable to obtain the best fit to the set of positive values. Because of the curvature differences between the cross correlation function and a parabolic curve near the zero crossings, the number of points will be fewer than the total number in the positive set (in this case, $J2 - J1 \leq 17$ for an accurate fit).

The normal equations may be solved by determinants to yield deterministic arithmetic expressions for the parabola coefficients as follows:

$$\Delta = A_1B_2C_3 + B_1C_2A_3 + C_1B_3A_2 - C_1B_2A_3 - B_1A_2C_3 - A_1B_3C_2$$

$$a_1 = \frac{1}{\Delta}\cdot\left(D_1B_2C_3 + B_1C_2D_3 + C_1B_3D_2 - C_1B_2D_3 - B_1D_2C_3 - D_1B_3C_2\right) \tag{3-9}$$

$$a2 = \frac{1}{\Delta}\cdot\left(A_1D_2C_3 + D_1C_2A_3 + C_1D_3A_2 - C_1D_2A_3 - D_1A_2C_3 - A_1D_3C_2\right)$$

$$a_3 = \frac{1}{\Delta}\cdot\left(A_1B_2D_3 + B_1D_2A_3 + D_1B_3A_2 - D_1B_2A_3 - B_1A_2D_3 - A_1B_3D_2\right)$$

Figure 3-8 shows the fitted parabola curve superimposed on the cross correlation sample points. This result illustrates the fitted curve after applying the least squares fit near the origin and shifting the resulting curve back to the correlation function range. The 17 points above the horizontal line represent the positive sample points in the range, *J*1 . . . *J*2, used in the data coefficients.

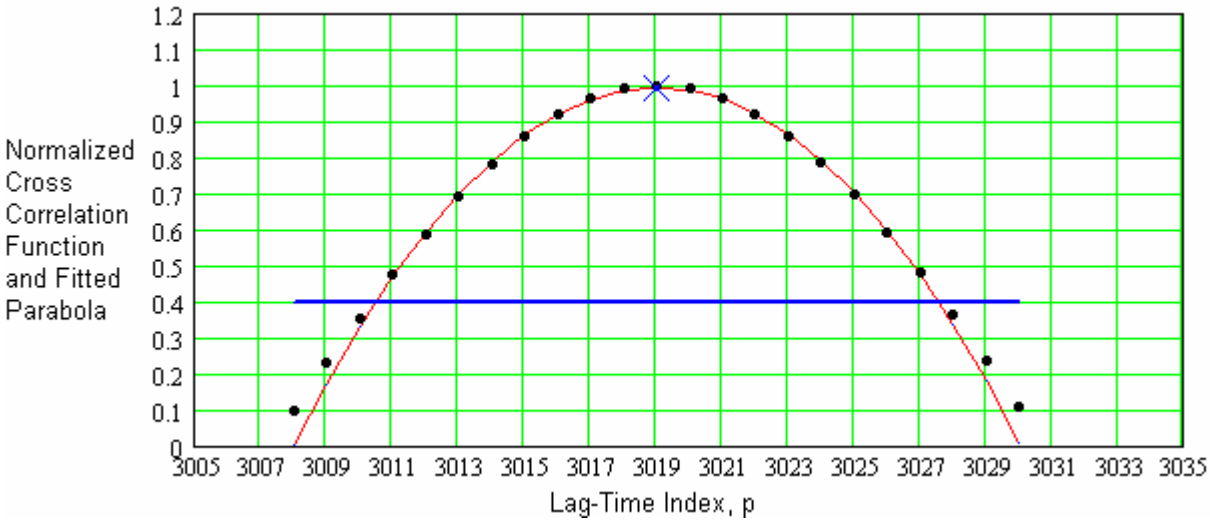

Figure 3-8. Cross correlation function (dots) and least squares fitted interpolation parabola (curved line). The parabola vertex is indicated by the X.

In practice, interpolated coordinate points on the entire parabola are not required to be calculated since the objective is only to determine the interpolated value of the parabola vertex point. The exact vertex point of the parabola may be found by differentiating Equation (3-7) and solving for the abscissa corresponding to the maximum value. By this procedure, the exact vertex point, indicated by "X" in Figure 3-8, has the coordinates

$$p_{\max} = -\frac{a_2}{2\,a_3} \qquad f(p_{\max}) = a_1 - \frac{a_2^{\,2}}{4\,a_3} \tag{3-10}$$

which, for this example, are

$$\left[p_{\max}\,,\, f(p_{\max})\right] = (3019.021\,,\, 0.994)\,. \tag{3-11}$$

The interpolated speed of sound in the test gas is then found using only p_{max} in the relation

$$v_G = \frac{2\,\Delta D_c}{\left(\frac{p_{\max}}{f_S}\right)} = \frac{2\times(0.500/12)\cdot \text{ft}}{\frac{3019.021}{50\,x\,10^6 \text{ samples/sec}}} = 1{,}380.138 \text{ ft/sec} \tag{3-12}$$

The value of p_{max} = 3019.021 found in this example happens to be very close to an actual sample point on the cross correlation function, suggesting that interpolation was not necessary. However, in other test gases or at other pressure-temperature conditions in the test gas, the interpolated value of p_{max} could fall anywhere within the range $3018 < p_{max} < 3020$.

3.4.4 Signal-to-Noise Requirements

Bench test data were collected using the 1-MHz ultrasonic transducer with spike-impulse excitation in several certified test gas mixtures. By selecting an example from these tests in which the signal-to-noise ratio was sufficiently high to provide an appropriately accurate determination of the speed of sound in the test gas in reference to the value calculated using the AGA-10 equation of state, the effects of noise contamination can be simulated. For this purpose, different ensembles of co-spectral noise interference were added to the ultrasonic waveform to simulate signals having various pre-defined signal-to-noise ratios by which sound speed calculations, including noise effects on the interpolation process, could be evaluated. Repetitive transient signal averaging was applied as a means for enhancing the signal-to-noise ratio in order to determine the amount of preconditioning required to effectively compensate for noise-contamination in the sensor signals. This noise reduction method must be implemented as part of the real-time analog-to-digital conversion and waveform memory storage process in the electronics system. In operation, the repetitive signals add coherently whereas any incoherent random noise adds in the RMS sense, resulting in a signal-to-noise ratio enhancement in the average. The process does not modify the wave shape of the signals being averaged.

3.4.5 Noise Contamination Model Analysis

Figure 3-9 shows a sample ultrasonic reflection waveform selected for signal-to-noise study from bench test measurements in test gas D. The signals were recorded using the 1.06-MHz NCT-510 ultrasonic transducer excited by a 180-Vpk spike-impulse transmitter signal. The receiver system had a 600-1,200 kHz passband followed by a 12-bit, 50-MSample/sec A-to-D converter and repetitive-signal-averaging buffer memory. The top waveform trace shown in

Figure 3-9 is the actual recorded ultrasonic waveform and has a minimal amount of noise contamination. The other waveform traces are the same signal waveform artificially contaminated with random noise having a 12:1 peak-signal-to-RMS-noise ratio defined as SNR1, in referring to the first reflection pulse.

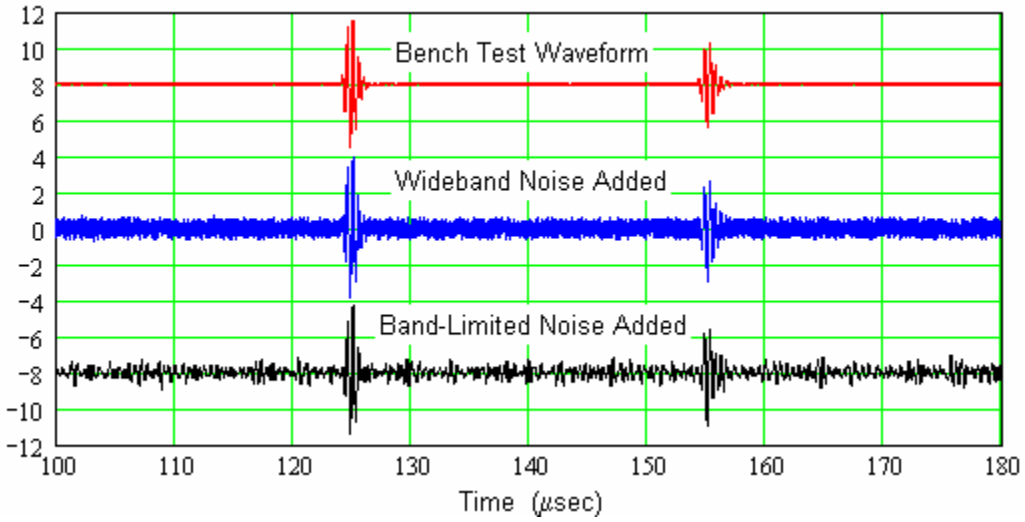

Figure 3-9. Ultrasonic reflection waveforms generated from test gas D for use in the noise-contamination model analysis.

Two noise-contamination conditions are represented in Figure 3-9: (i) wideband noise; and (ii) band-limited noise. These noise conditions can occur in practice, depending upon the point in the electronics system at which the noise interference might originate. For example, wideband noise is produced at a point in the system after the receiver band-pass filter. Band-limited noise interference, on the other hand, is wideband noise that has been filtered by the band-pass frequency response of the receiver system. For clarity in comparing these two noise cases, the RMS noise levels are adjusted to be equal so as to give the same peak-signal-to-RMS-noise ratio in each case. This reference condition allows the effects of noise interference to be compared on common terms, but with the two sources of noise independent of one another. Wideband noise typically originates as electronic circuit noise in the high-gain VGA post-amplifier, as time jitter in the A/D converter, and as least-significant-bit digitization noise inherent in the 12-bit analog-to-digital amplitude resolution of the recorded waveforms. Band-limited noise is primarily attributable to electronic circuit noise generated in the LNA receiver preamplifier and in the resistive component of the ultrasonic transducer internal impedance, plus noise generated in the band-pass filter electronic circuits. The band-pass filter selected for use in the band-limited noise case was a six-pole Butterworth filter with low and high cut-off frequencies of 600 kHz and 1,540 kHz, respectively, selected to minimize frequency distortion of the ultrasonic waveforms.

Experience with the prototype speed of sound sensor system during the various bench tests showed that the residual noise in the recorded waveforms had a bandwidth significantly greater

than that of the ultrasonic receiver system band-pass filter and, therefore, the wideband noise simulation results are considered to be the most representative of the present sound speed sensor system. The results obtained using band-limited noise simulation can be translated, approximately, to an equivalent wideband noise condition ahead of the receiver band-pass filter but having a RMS value approximately seven times higher than the wideband noise shown in Figure 3-9. The factor of seven is empirically associated with the selected receiver band-pass filter characteristics.

The two classes of noisy signals, with various specified signal-to-noise ratios, were processed by computing the noise-contaminated signal cross correlation function, interpolating the coherence maximum time-of-flight difference between the two reflections, and computing the measured speed of sound. By increasing the signal-to-noise ratio to a level at which the error in derived speed of sound exceeded the target value of $\Delta v_G = \pm 0.10$ ft/sec, the minimum acceptable ultrasonic waveform signal-to-noise ratio for each noise contamination condition was determined.

The noise modeling results for wideband noise contamination are presented in Figure 3-10, showing the derived speed of sound versus peak-signal-to-RMS-noise ratio of the input waveforms. These results show that noise-induced errors in sound speed clearly decrease with increasing signal-to-noise ratio but are still present at signal-to-noise ratios as high as SNR1 ≥ 200:1. However, at this limit the sound speed accuracy is approximately $\Delta v_G = \pm 0.01$ ft/sec, an accuracy tolerance that is about an order of magnitude better than the target value required in the energy meter application. A practical minimum signal-to-noise ratio at which the target accuracy of $\Delta v_G = \pm 0.10$ ft/sec can be achieved reliably in test gas D is estimated to be about SNR1 ≥ 20:1 for the case of wideband noise contamination.

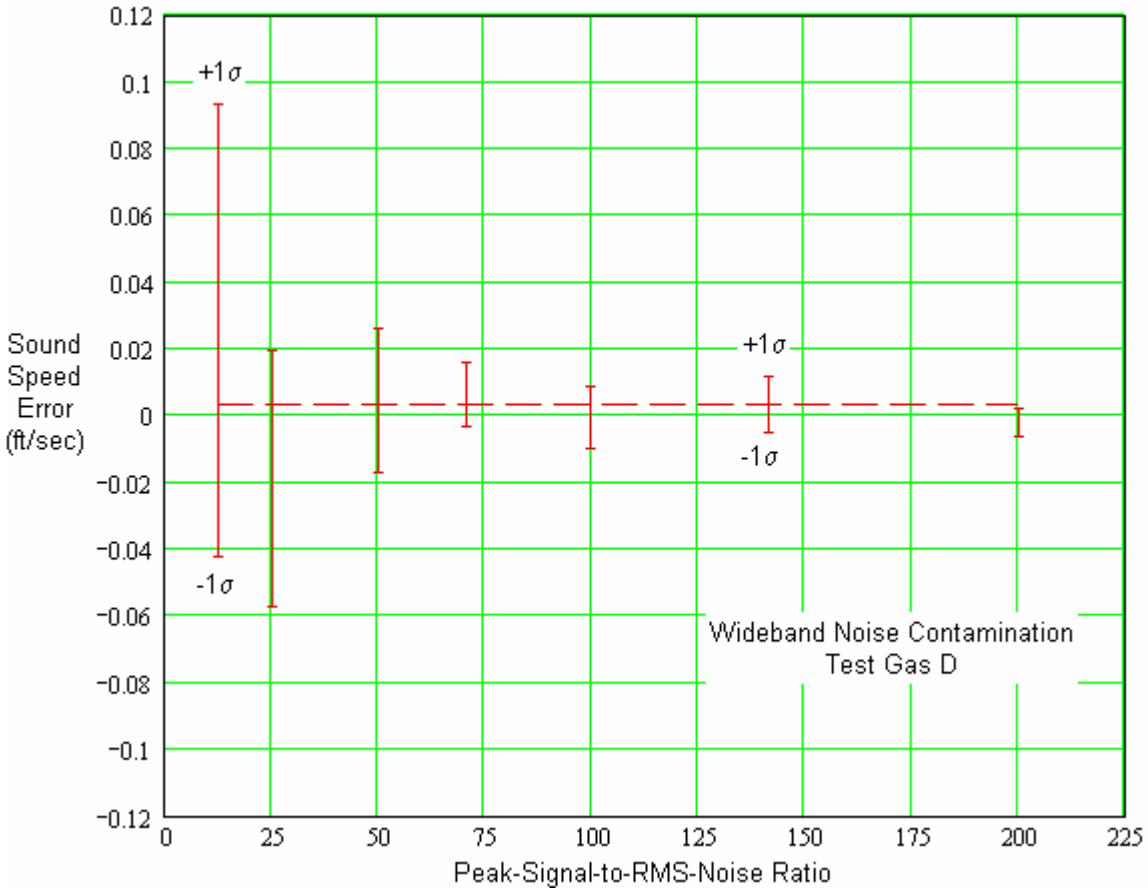

Figure 3-10. Interpolated speed of sound versus signal-to-noise ratio SNR1 for wideband noise contamination in test gas D.

Figure 3-11 presents the noise modeling results for band-limited noise contamination, showing the derived speed of sound versus peak-signal-to-RMS-noise ratio of the input waveforms. The minimum signal-to-noise ratio for reliable speed of sound sensor accuracy of $\Delta v_G = \pm$ 0.10 ft/sec in this case is estimated to be approximately SNR1 ≥ 60:1 peak-signal-to-RMS-noise, a level about three times higher than that derived for wideband noise contamination. Although the noise-induced errors decrease with increasing signal-to-noise ratio, the actual error levels are about three times higher than those in the wideband noise case. The reason for this difference is that the band-limited noise energy is more fully contained within the same frequency range as the pulse signal reflections and, hence, has a greater perturbation effect on the cross correlation function. In this band-limited noise case, the sound speed error appears to be approximately $\Delta v_G = \pm$ 0.03 ft/sec for SNR1 ≥ 200:1.

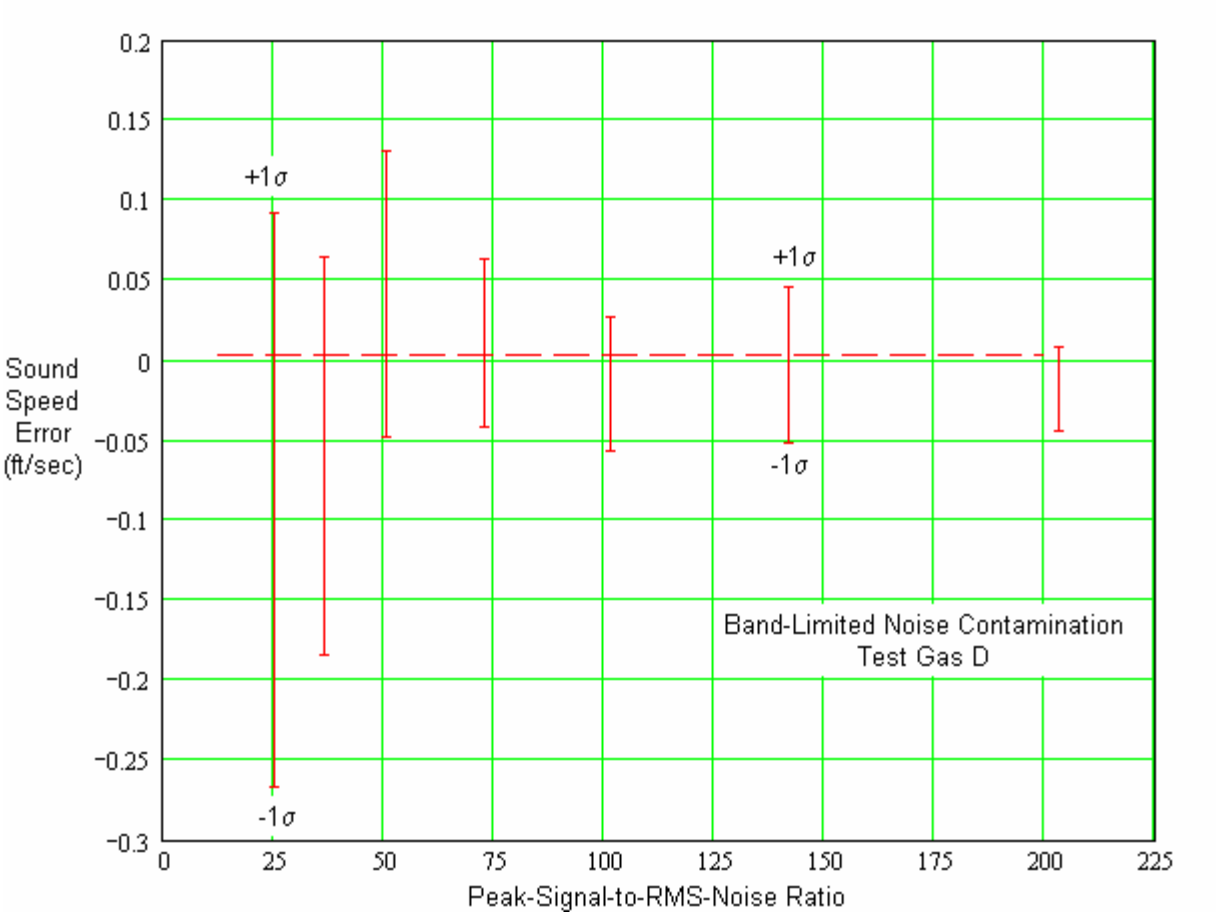

Figure 3-11. Interpolated speed of sound versus signal-to-noise ratio SNR1 for band-limited noise contamination in test gas D.

A further consideration regarding the sound speed error results shown in Figures 3-10 and 3-11 is the effect of ultrasonic attenuation and its associated reduction of the signal-to-noise ratio of the second pulse reflection. That is, the impact of contaminating noise on the cross correlation function is dependent on the signal-to-noise ratios of both reflections and, hence, viscous damping losses in the test gas will play a practical part in the sound speed measurement accuracy, particularly when the transducer operating frequency is as high as 1 MHz. Referring to Figure 3-2, test gas A exhibits a much greater attenuation loss than test gas D and, since the two-state inferential method requires sound speed measurements at low and high pressures, the noise-induced errors in test gas A at pressures in the range of 65-70 psia represent a possible worst case.

The noise-contamination model analysis was repeated using bench test data obtained using test gas A at P = 70.05 psia and T = 73.12°F. The attenuation rates in Table 3-2 indicate that the attenuation loss in test gas A is about 6 dB greater than that in test gas D over the pressure range of 65 – 100 psia. Therefore, the signal-to-noise ratio of the second reflection in test gas A will be about one-half that of test gas D over the same pressure range. Additionally, however, the absolute effect of attenuation loss over the complete pulse-echo path in the gas test chamber acts

to reduce the peak-signal amplitudes in test gas A by a factor of about four in comparison with those in test gas D. Therefore, if the noise contamination conditions are constant when testing the two gases, as may be assumed, the noise impact on sound speed measurements in test gas A are very likely to be greater.

Figures 3-12 and 3-13 show the derived speed of sound versus peak-signal-to-RMS-noise ratio for wideband and band-limited noise contamination for test gas A. For wideband noise contamination, the results in Figure 3-12 indicate that the minimum signal-to-noise ratio for reliable speed of sound sensor accuracy of Δv_G = ± 0.10 ft/sec in test gas A is estimated to be approximately SNR1 ≥ 50:1 peak-signal-to-RMS-noise. This level is about 2.5 times higher than that derived for wideband noise contamination in the low-attenuation test gas D shown in Figure 3-10. Figure 3-12 also shows that, although the sound speed error decreases with increasing signal-to-noise ratio, the rate of decrease is significantly less than that observed for the lower attenuation condition in test gas D, indicating that the signal-to-noise ratio of the second reflection is the critical parameter affecting high-accuracy sound speed measurements.

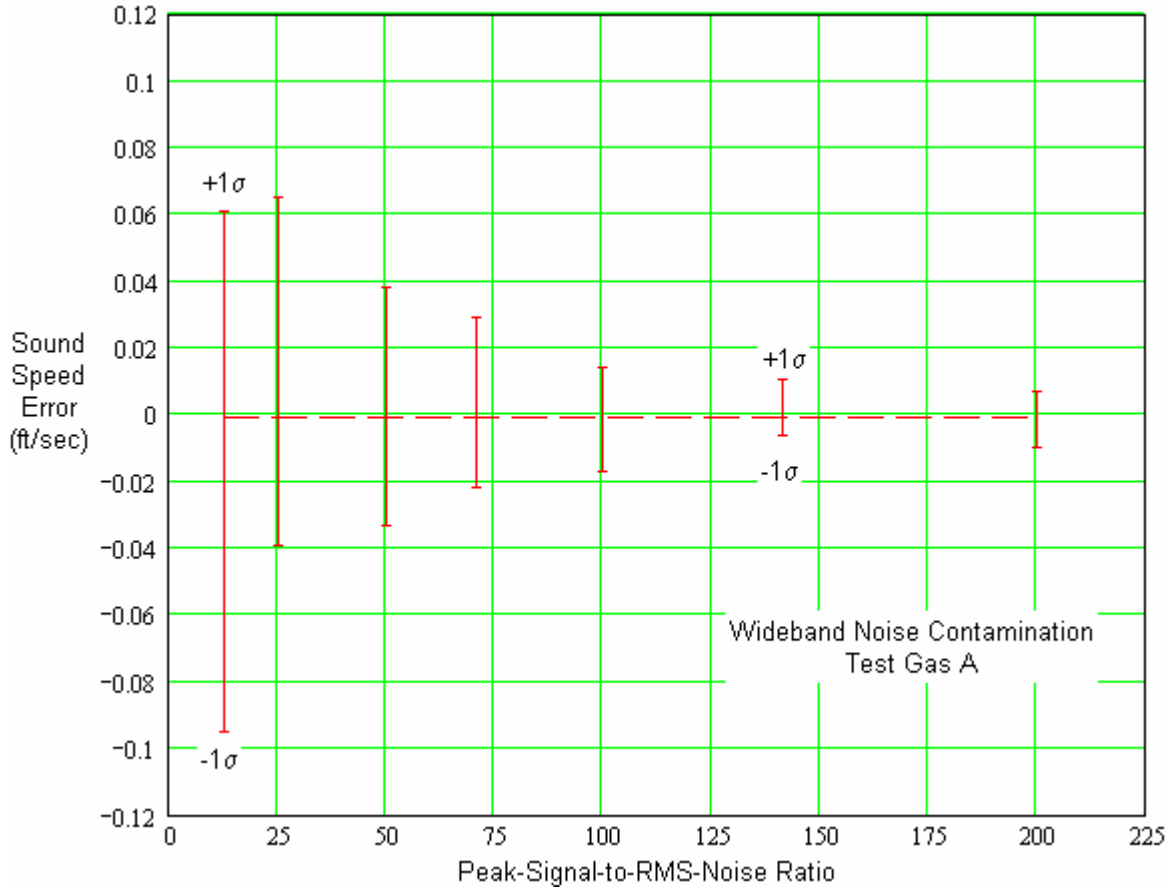

Figure 3-12. Interpolated speed of sound versus signal-to-noise ratio SNR1 for wideband noise contamination in test gas A.

The effects of band-limited noise are noticeably greater in test gas A than in test gas D. Figure 3-13 shows that the minimum signal-to-noise ratio for reliable sound speed sensor accuracy of Δv_G = ± 0.10 ft/sec in test gas A is approximately SNR1 ≥ 140:1. This value is about 2.3 times higher than the 60:1 signal-to-noise ratio required in test gas D, further indication that in-band noise effects on the second reflection waveform become increasingly critical in gas compositions having higher ultrasonic attenuation.

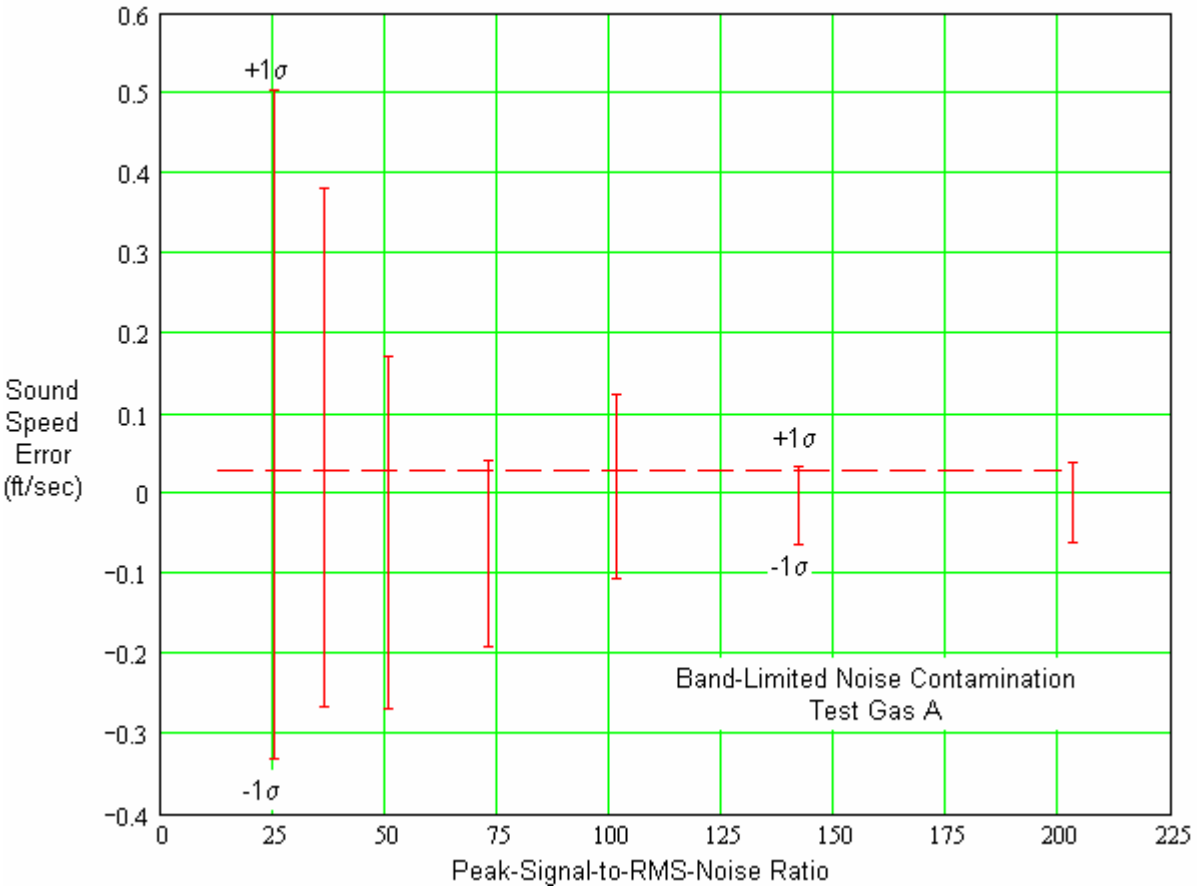

Figure 3-13. Interpolated speed of sound versus signal-to-noise ratio SNR1 for band-limited noise contamination in test gas A.

3.4.6 Signal-to-Noise Ratio Enhancement

As noted in the preceding section, precision sound speed measurements are strongly dependent on the signal-to-noise ratio of the recorded ultrasonic waveforms. Table 3-6 summarizes the derived minimum signal-to-noise ratios for sound speed measurements accurate to within Δv_G = ± 0.10 ft/sec for wideband and band-limited noise contamination conditions in the low and high attenuation test gases used in the noise model studies. The SNR1 and SNR2 values in Table 3-6 refer to the positive-peak-signal-to-RMS-noise ratio of the first and second reflections, respectively. The signal-to-noise ratio of the second reflection is reasonably

consistent as the governing parameter for achieving the desired sound speed accuracy of Δv_G = ± 0.10 ft/sec.

Table 3-6. Minimum ultrasonic waveform signal-to-noise ratio guidelines for speed of sound accuracy of Δv_G = ± 0.10 ft/sec (T » 73°F).

Noise Contamination	Test Gas A (high attenuation)		Test Gas D (low attenuation)	
	SNR1	SNR2	SNR1	SNR2
Wideband (65 psia)	50 : 1	12.5 : 1		
Wideband (100 psia)			20 : 1	13 : 1
Band-Limited (65 psia)	140 : 1	35 : 1		
Band-Limited (100 psia)			60 : 1	38 : 1

All of the ultrasonic waveforms used in the speed of sound interpolation analysis and in the noise contamination studies were recorded using a signal averaging oscilloscope capable of enhancing the signal-to-noise ratio of the test data. The recorded signal-to-noise ratios were in the range of about 50:1 for test gas A and about 170:1 for test gas D using 64 waveforms in the signal averages. The original ultrasonic waveforms had un-enhanced signal-to-noise ratios of about 6:1 at 65 psia to 11:1 at 100 psia in test gas A and about 20:1 at 65 psia to 22:1 at 100 psia in test gas D. Thus, when considering the minimum signal-to-noise ratios in Table 3-6, improving the signal-to-noise ratio of the ultrasonic signals in the speed of sound sensor is necessary for accurate results.

The noise contamination model described above was arranged to generate repetitive versions of the noisy waveforms and average them to simulate the repetitive-transient signal averaging process. Repetitive signal averaging is normally designed to progress in powers of two, since the idealized enhancement capability of the method increases as $\sqrt{N}$, where N is the number of waveforms in the average. In well-designed electronics systems, the waveform averaging process can be productive using averaging up to about 256 repetitions or more, depending upon the timing stability of the digital sampling circuits (time jitter in digital sampling can reduce the coherent averaging of the waveform signals of interest). However, when the contaminating noise is band limited, the averaging process is somewhat less effective and is dependent on the specific spectral properties of the signals and the interfering noise.

Figure 3-14 shows the results of repetitive-transient waveform averaging for a two-reflection waveform having an initial signal-to-noise ratio of 6:1. For additive band-pass filtered noise having the same frequency bounds as the ultrasonic receiver passband, an average of 256 waveform repetitions can reduce the noise by a factor of about 15, in comparison with the ideal factor of $\sqrt{256} = 16$ obtainable for wideband noise.

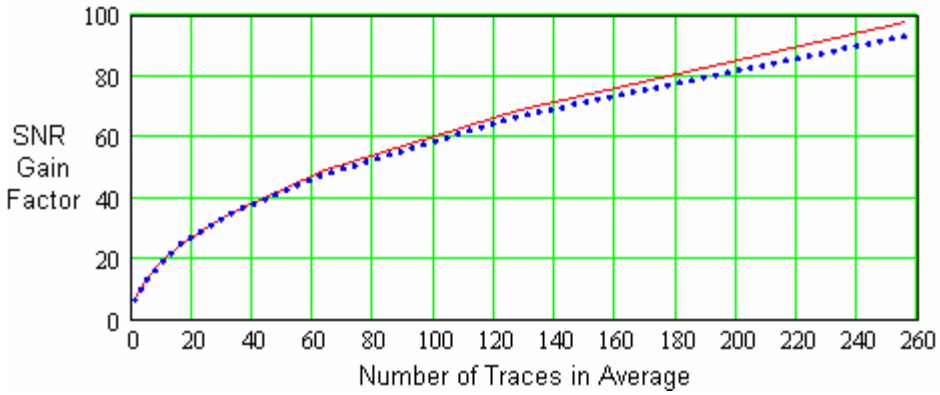

Figure 3-14. Improvement in ultrasonic waveform signal-to-noise ratio due to repetitive-transient signal averaging (initial SNR = 6:1).

Signal averaging was applied to the speed of sound interpolation analysis to demonstrate the ability to precondition noise contaminated signals having an initial signal-to-noise ratio of 12.5:1. Figure 3-15 shows results for wideband noise contamination of waveforms in test gas D similar to those in Figure 3-10, in which the parameter M is the number of waveforms used in the repetitive signal average. The sound speed accuracy and standard deviations, although derived using different random number ensembles as the contaminating noise, are essentially identical to those derived earlier in Figure 3-10. Figure 3-16 shows waveform averaging results for band-limited noise in test gas D similar to those in Figure 3-11. Results obtained for waveform averaging in test gas A were closely identical to those in Figure 3-12 and Figure 3-13 and are not presented here.

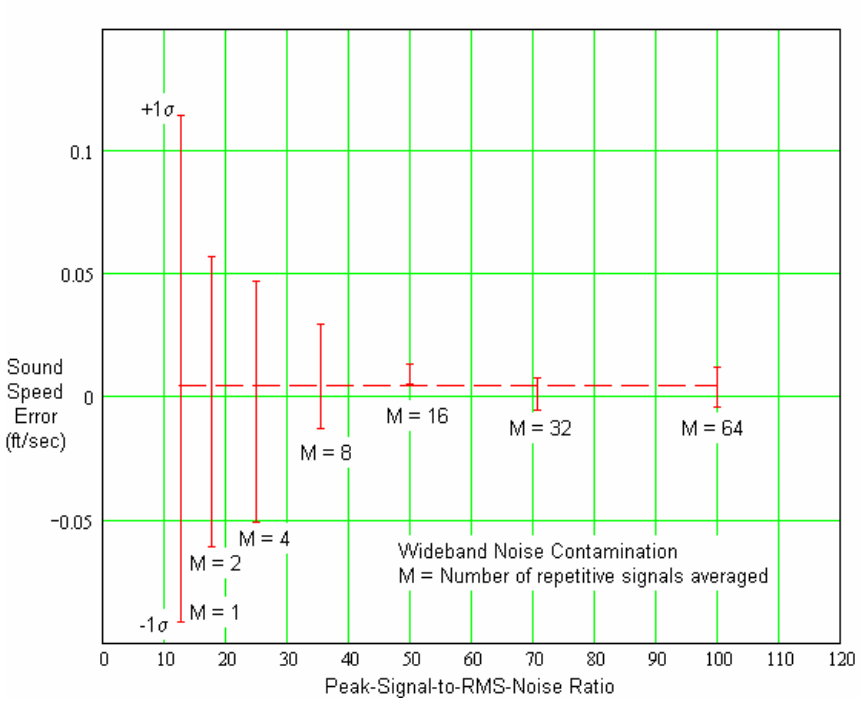

Figure 3-15. Interpolated speed of sound versus enhanced signal-to-noise ratio SNR1 for wideband noise contamination in test gas D. M = 1 corresponds to an initial signal-to-noise ratio of 12.5:1.

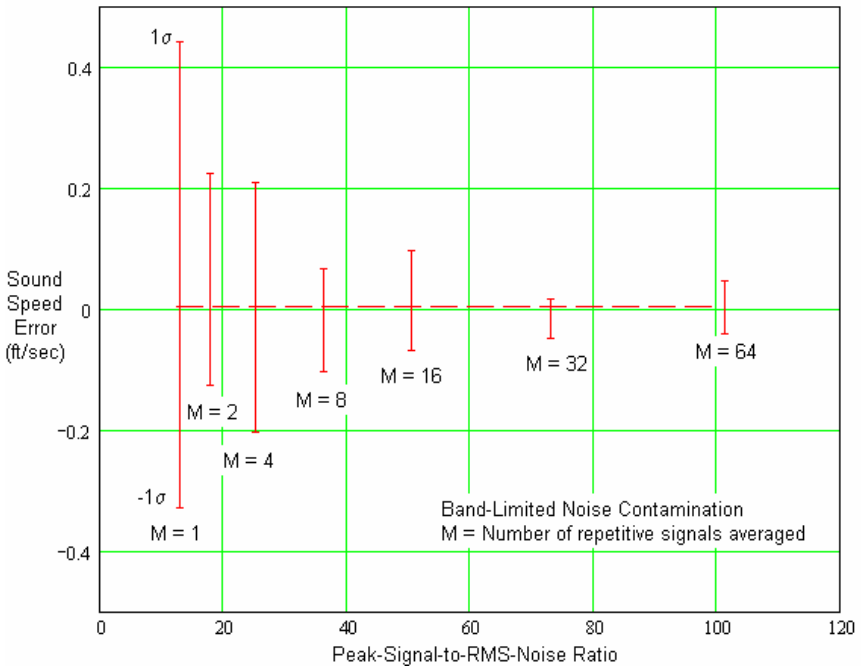

Figure 3-16. Interpolated speed of sound versus enhanced signal-to-noise ratio SNR1 for band-limited noise contamination in test gas D. M = 1 corresponds to an initial signal-to-noise ratio of 12.5:1.

This page is intentionally blank.

4. CARBON DIOXIDE SENSOR

4.1 CALIBRATION STUDIES

The carbon dioxide sensor presently used in the energy meter module is a nondispersive infrared absorption sensor manufactured by Vaisala Oy, Helsinki, Finland. The Vaisala Model GMP-221 Carbocap® sensor is equipped with interchangeable handheld probes to permit CO_2 measurements at either 0-10 mol% full scale (FS) or 20 mol% FS. The GMP-221 sensor is designed to operate at normal atmospheric pressure and is stable for operation over the temperature range of -4°F to 140°F. With appropriate corrections for pressure and temperature variations under normal atmospheric conditions, this sensor has a calibrated accuracy of ±0.05 mol% CO_2 with a nonlinearity of less than 0.5% of full scale. The sensor is factory calibrated at standard conditions of 1013 mb and 25°C (14.696 psia and 77.0°F).

The sensor transmitter electronics unit operates from a 24 VDC power supply and provides a standard 4-20 mA FS output current signal. The sensor probes, containing the optical sensing assembly and associated power and electronic control circuits, are 0.73 inch in diameter and 4.29 inches in length. The optical sensor assembly consists of a small tungsten filament lamp for producing the infrared source radiation and a photodiode infrared detector, mounted on opposite sides of a small gas flow channel. The photodiode is located behind an electrically tuned narrow band Fabry-Perot infrared filter, capable of passing optical wavelengths of either 4.26 µm (CO_2 absorption) or 3.90 µm (no CO_2 absorption) by which the relative absorption effect of CO_2 concentration in the gas is determined. The probe body and internal electronic module and electrical connector base are sealed by an encapsulating polymer potting compound.

The GMP-221 has been adapted for use in the energy meter module by means of a custom-designed CO_2 test chamber 2.75 inches in diameter and 5.125 inches in length, in which the handheld probe is inserted through a pressure-seal port and clamped in place with its connector base external to the test chamber. The test chamber has a helical groove machined within its cylindrical aluminum body, through which the test gas flows at a rate of 200 ml per minute or less to equilibrate the gas temperature to that of the chamber prior to entering the chamber for CO_2 measurements. The CO_2 test chamber also has dedicated pressure and temperature sensors to facilitate accurate corrections of the sensor readings.

Infrared absorption by the carbon dioxide in a gas mixture is a process that occurs at the molecular level in the gas. The CO_2 molecules respond selectively to certain wavelengths, selected in this sensor to be their strongest absorption band at 4.26 µm, and absorb part of the transmitted infrared energy. The absorbed energy is irreversibly converted to heat energy in the gas. This absorption process is directly related to the volume fraction of CO_2 concentration in the gas mixture. If the gas mixture is assumed to obey the ideal gas law, which is approximately true for natural gas at near-atmospheric pressure, then the volume fraction of CO_2 is also proportional to the partial pressure and to the mass fraction of the CO_2 content. Any of these quantities reduce to a fundamental measure of the molecular density (mole fraction) of CO_2 in the gas. Therefore, in principle, when the CO_2 sensor is operated at variable temperatures and

pressures that are within the normal range of atmospheric conditions, adequate temperature and pressure corrections may be obtained for the measurements of CO_2 content by applying independent calibration adjustments of the form:

$$X_{CO2sensor} = \frac{T_C}{P_C} x_{CO2} \tag{4.1}$$

where:

$x_{CO2} = \left[\frac{I_{CO2} - 4}{16}\right] \cdot FS_{CO2}$ = raw CO_2 sensor reading;

$T_C = \frac{T_F + 459.67R}{536.67R}$ = absolute temperature correction factor;

$P_C = \frac{P_{psia}}{14.696_{psia}}$ = absolute pressure correction factor;

I_{CO2} = sensor output current (mA);

FS_{CO2} = full-scale range of sensor probe (mol %);

T_F = gas temperature at sensor (°F);

P_{psia} = gas pressure at sensor (psia).

The scaling factor in Equation (4.1) is a first-order adjustment of the sensor reading, made to normalize it to the reference mole fraction at which the sensor was originally calibrated.

The GMP-221 sensor is stated by the manufacturer to have a small nonlinear error, typically about ±0.05 mol% for readings made with the 10 mol% FS probe and about ±0.1 mol% for readings by the 20 mol% FS probe. These errors are larger than the accuracy tolerance required by the inferential energy meter. Moreover, corrections of such nonlinear errors are not possible without knowledge of the nonlinear characteristics of the sensor response, which may be caused in part by the thermodynamic behavior of the gas and in part by the sensing instrument itself. As a consequence, in order to adapt the infrared absorption sensing technique for use in the energy meter application, it must be calibrated for operation at the temperatures and pressures anticipated in the energy meter module.

In its present mode of operation, the energy meter module is intended to operate at a predetermined regulated pressure (typically about 75 psia) adequate for accurate speed of sound measurements, and at temperatures characteristic of ambient conditions at various energy meter field installations (typically in the range of 0°F to 120°F). Further, a design goal in developing

the energy meter is to integrate the CO_2 sensor into the speed of sound sensor chamber, thereby eliminating the need for separate test chambers and separate pressure and temperature sensors for use with both the CO_2 and sound speed sensors. The CO_2 sensor must therefore be adapted to operate at pressures near 75 psia and ambient temperatures in the range of 0-120°F.

From a generalized point of view, the calibration process can be implemented by first demonstrating that the Vaisala GMP-221 sensor can respond effectively to a useful range of carbon dioxide concentrations in natural gas at operating pressures on the order of 70 – 80 psia, and then devising a suitable nonlinear compensating factor to adjust the normalized sensor readings. The resulting compensation factor will empirically equalize the combined nonlinear effects caused by the non-ideal behavior of the gas and any nonlinear characteristics of the sensing instrument. On the premise that the nonlinear effects are primarily associated with non-ideal gas behavior, changes in this CO_2 mole fraction dependence, whether caused by pressure or temperature, must be compensated for. The tests needed for this compensation can be performed by conducting sensor measurements on several gases having a range of CO_2 concentrations, either at constant temperature and variable pressure or at constant pressure and variable temperature. For convenience, the tests described in the next section were conducted on four test gases at room temperature and various pressures.

4.2 CALIBRATION TESTS AT ELEVATED PRESSURE

The CO_2 sensor was tested at pressures in the range of 15-150 psia in a small pressure vessel operated at room temperature in the MRF Calibration Laboratory. Figure 4-1 shows the pressure vessel test setup with the CO_2 sensor in place. In this arrangement, the CO_2 test chamber is installed in the pressure vessel with electrical connections for the 8-wire sensor probe and the 4-wire RTD temperature sensor brought out through a multiple-conductor electrical feed-through fitting in the cover plate. The cover plate also has three threaded connections for the gas inlet, the gas outlet, and pressure instrument wiring. The pressure vessel and electrical feed-through fitting have a pressure rating of 1,000 psia.

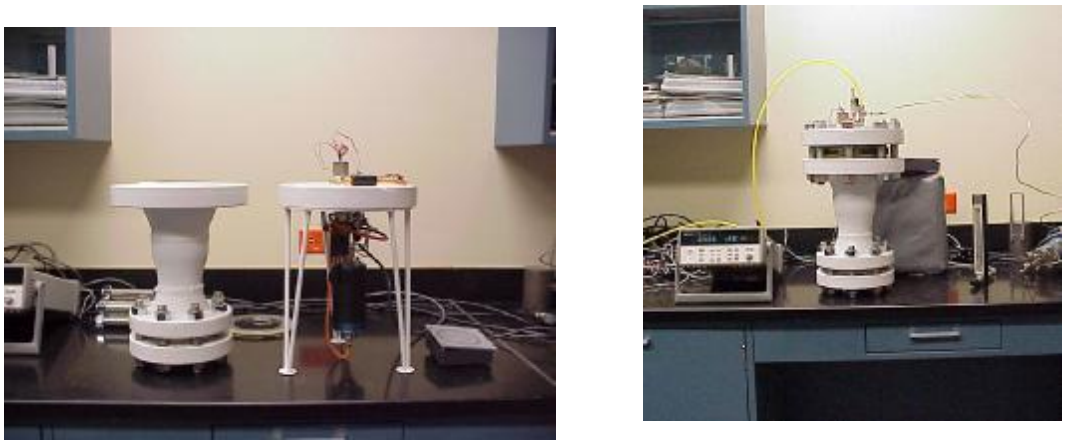

(a) Pressure vessel and CO_2 sensor. **(b) Assembled pressure vessel.**

Figure 4-1. Setup for carbon dioxide sensor pressure tests.

Four certified gases were used in the CO_2 sensor tests. Two of these gases were gas #3 and gas #8 listed later in this report in Table 6-2. The other gases consisted of a certified calibration gas containing 1.00 mol% CO_2 normally used in MRF flow loop tests, and a certified binary gas mixture containing 98 mol% methane and 2.00 mol% CO_2. The first three gases were tested over the pressure range of 15-150 psia at 10 psi pressure increments. The binary gas mixture was only available at a supply pressure of 70 psia. The GMP-221 sensor probe rated at 20 mol% FS was proof tested at pressures up to 150 psia with the first three gases. The sensor readings obtained in these tests for pressures of 50, 60, and 70 psia were combined with sensor readings of the binary gas mixture at 50, 55, 60, 65, and 70 psia to examine the nonlinear response of the sensor. All tests were performed under laboratory room temperature conditions ranging from 74°F to 76°F.

When operating above atmospheric pressure, the sensor full-scale measurement range will be reduced in approximate inverse proportion to the measurement pressure expressed in atmospheres. That is, a 20 mol% FS sensor designed for operation at one atmosphere pressure will have a range of approximately 4 mol% FS at 75 psia. This pressure dependence imposes a performance limit on the measurement range of the CO_2 sensor. This modified full-scale range may be changed further by any additional changes in sensitivity due to nonlinearity in the sensor itself.

The new and more comprehensive calibration procedure involves specifying the nominal pressure at which the sensor is to operate, and then performing calibration measurements on several test gases over a range covering the specified operating pressure. For best results, the test gases must have different CO_2 concentrations that span the intended range of sensor operation, and the specified operating pressure must not be so high as to prevent the sensor probe from responding to the highest concentration of interest. The number of test gases used in the measurements will govern the accuracy by which the nonlinear calibration correction formula may be fitted to the response of the sensor. Given such a series of test gas measurements, the raw CO_2 sensor readings are first normalized to the basic calibration reference corrections by applying the standard correction factor in Equation (4.1). Then, by regression analysis, an analytical relationship may be derived to match the sensor readings to the known concentration values. This formula may then be used as an interpolation equation for correcting sensor readings of other gases for the nonlinear characteristics of the sensor.

This calibration procedure was applied to the GMP-221 sensor using the four test gases mentioned above, with CO_2 content ranging from 0.25 mol% to 3.057 mol%. The range of CO_2 concentrations in these test gases permitted the sensor to be operated at pressures up to 70 psia without saturating the transmitter output current at the highest CO_2 content. The sensor readings were normalized to the calibration reference conditions, and third-order polynomial equations were derived for four cases: (1), all available test data on all gases (18 test readings); (2), (3) and (4), common pressure readings among all test gases at 50, 60, and 70 psia, respectively (4 test readings each). The calibration correction equations are of the form:

$$X_{CO2} = A\left(x_{CO2\,sensor}\right)^3 + B\left(x_{CO2\,sensor}\right)^2 + C\left(x_{CO2\,sensor}\right) + D \tag{4.2}$$

where $x_{CO2sensor}$ is the temperature and pressure corrected sensor reading computed from Equation (4.1). Table 4-1 lists the coefficients *A*, *B*, *C*, and *D* determined for each regression analysis.

Table 4-1. Regression coefficients for separate correction equations.

Analysis Case	Average Test Pressure	A	B	C	D
All Data 50-70 psia	59.931	1.37814790	-9.340000	0.650098	8.5642×10^{-4}
50 psia	49.940	101478948	-7.721469	0.657986	9.1170×10^{-4}
60 psia	59.915	117.271187	-8.010022	0.632115	8.7460×10^{-4}
70 psia	69.890	190.561017	-11.894645	0.666619	7.0966×10^{-4}

Figure 4-2 shows a plot of the four calibration correction equations indicating the overall nonlinear characteristics of the GMP-221 sensor. Figure 4-3 shows the residual differences between the separate pressure curves and the curve obtained using all test data. These residual errors fall within the ±0.05 mol% bounds required by the algorithm for adjusted CO_2 measurements, for CO_2 content up to about 2.5 mol% and sensor operating pressures up to about 70 psia. The residual error curves also indicate that a more exact correction equation could be obtained by including additional test gases having CO_2 concentrations of 1.5 mol% and 2.5 mol%.

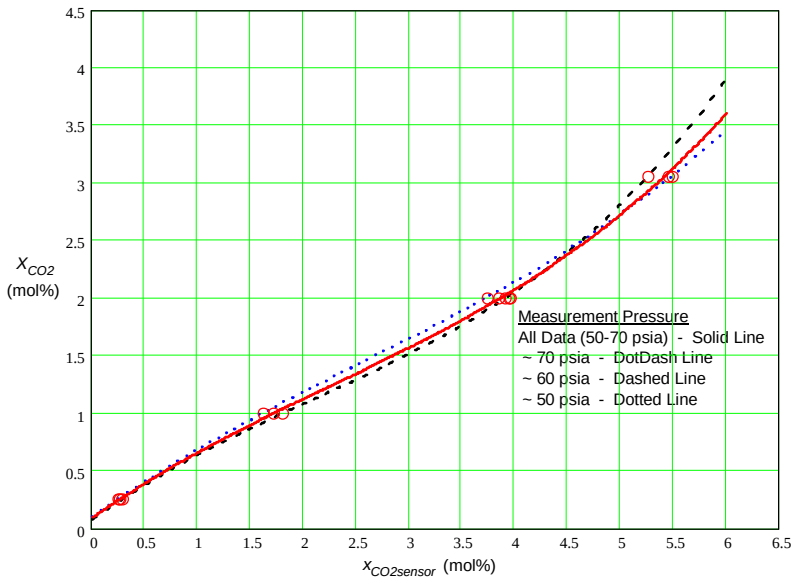

Figure 4-2. Nonlinear calibration characteristics of the Vaisala GMP-221 CO_2 sensor.

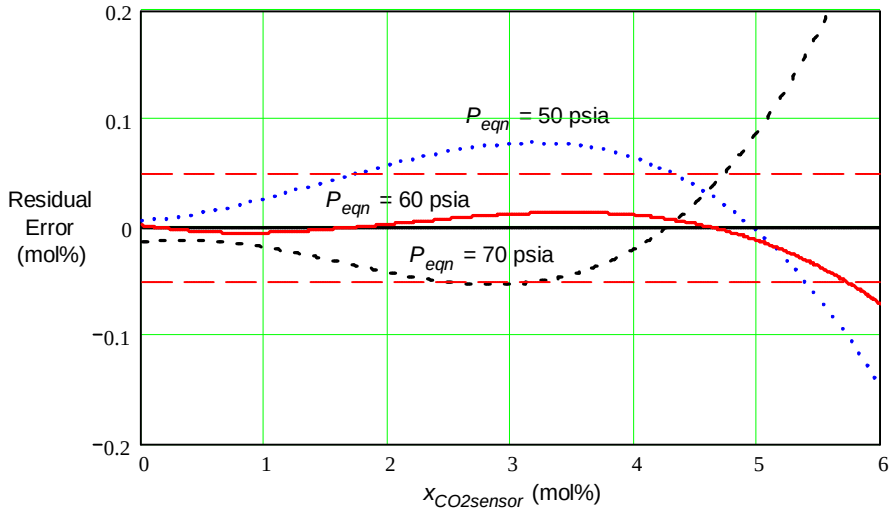

Figure 4-3. Residual errors in third-order polynomial correction equations for the Vaisala GMP-221 CO_2 sensor.

The similarities of the three correction curves for 50, 60, and 70 psia suggest that they might be scaled to provide improved correction accuracy in sensor readings taken at operating pressures that are within about 5 to 10 psia of the individual reference pressures. For this purpose, an empirical pressure-dependent scaling factor was applied to the regression coefficients of the third-order polynomials to yield a compensated CO_2 correction equation of the form:

$$X_{CO2} = SF \cdot \left[A(x_{CO2sensor})^3 + B(x_{CO2sensor})^2 + C(x_{CO2sensor}) + D\right] \tag{4.3}$$

where:

$SF = \left(\frac{P_{meas}}{P_{eqn}}\right)^{\pm p}$ = pressure correction scale factor;

P_{meas} = pressure at which the sensor reading was recorded;

P_{eqn} = pressure for which the correction equation was derived;

p = a fractional exponent whose sign is selected to make $SF < 1$.

The improvements gained by this scaling adjustment are demonstrated by using the regression equations for 60 psia and 70 psia to adjust the sensor readings for test gas #4 (CO_2 concentration: 2.00 mol%) at pressures of 60, 65, and 70 psia. Table 4-2 presents the corrected sensor readings without scaling (p = 0) and with values of p = 0.15, 0.20, and 0.25. The results

indicate that a value of p = 0.20 is appropriate for adjusting all of the readings into the desired ±0.05 mol% measurement tolerance, when the correction coefficients are applied to measurements within ±10 psia of the correction equation reference pressure.

Table 4-2. Scaling improvements using nonlinear correction equations on sensor readings from test gas #4 (CO_2= 2.00 mol%).

P_{meas} (psia)	Exponent p	P_{eqn} 60 psia	X_{CO2} Error	P_{eqn} 70 psia	X_{CO2} Error
60	0	---	---	2.02343	0.02343
	0.15	---	---	1.97804	-0.02196
	0.20	---	---	1.97077	-0.02923
	0.25	---	---	1.96353	-0.03647
65	0	2.05796	0.05796	2.02343	0.02343
	0.15	2.03329	0.03329	2.00121	0.00121
	0.20	2.02514	0.02514	1.99386	-0.00615
	0.25	2.01702	0.01702	1.98653	-0.01347
70	0	2.05796	0.05796	---	---
	0.15	2.01312	0.01312	---	---
	0.20	2.99760	-0.00240	---	---
	0.25	1.98221	-0.01779	---	---

A nonlinear correction equation of the form shown in Equation (4.3) was incorporated in the energy meter algorithm to properly adjust the sensor readings when operating at elevated pressure. For the anticipated energy meter configuration in which the CO_2 sensor probe element is incorporated into the speed of sound sensor test chamber, a final calibration equation based on tests using up to six references gases in the sensor range of interest is recommended.

This page is intentionally blank.

5. 2003 PROTOTYPE ENERGY METER SYSTEM

The 2003 prototype inferential gas energy meter system is designed to implement the two-state gas measurement technique described in Chapter 2. This chapter discusses the operation of the complete system.

5.1 TWO-STATE MEASUREMENT SYSTEM

The complete prototype system consists of a Gas Sensor Module, an Electronics and Communications Module, and a Master Control and Data Acquisition Module. Figure 5-1 illustrates the system in block diagram form, showing the three modules and their functional components.

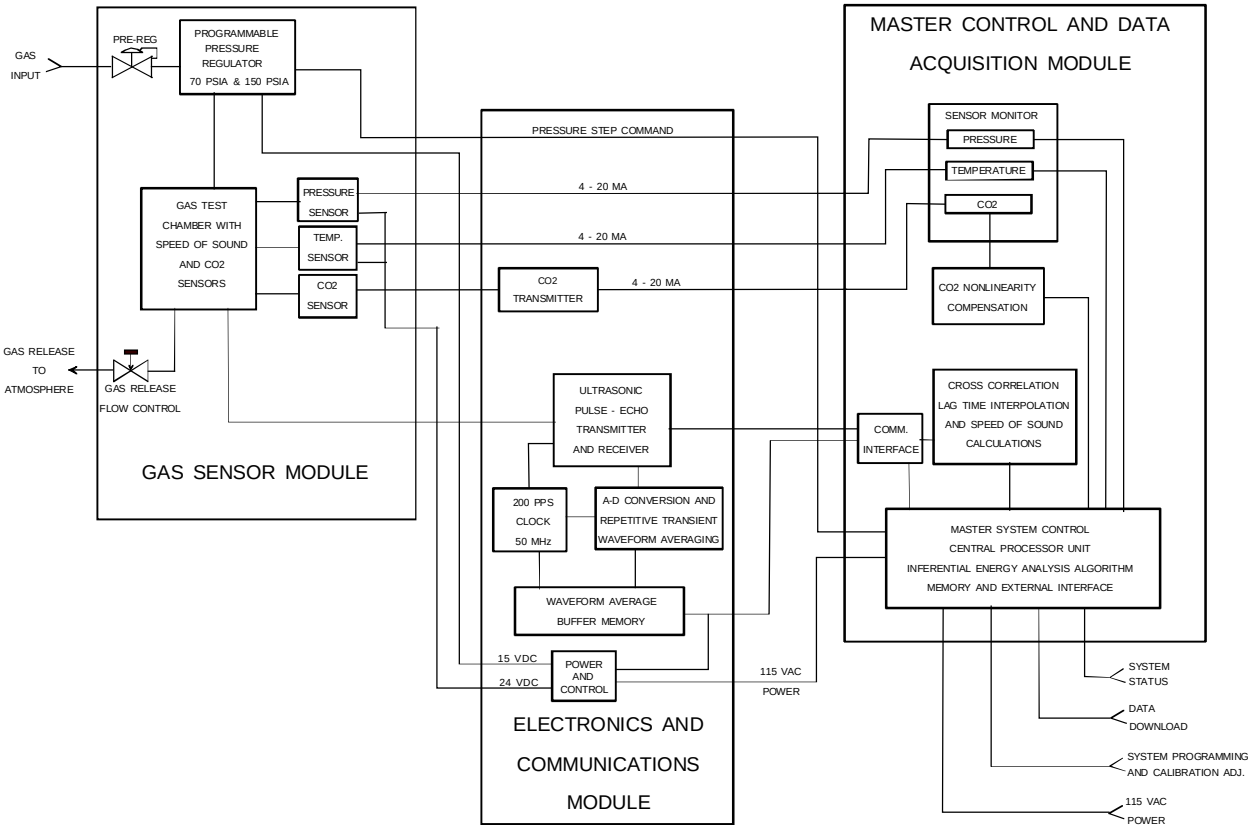

Figure 5-1. The 2003 inferential energy meter system.

5.1.1 Gas Sensor and Control Module

The Gas Sensor and Control Module is a hardware component intended to be installed as near as practical to the gas pipeline being monitored. The installation requires short small-bore

connecting tubing to minimize the lead-in gas volume between the pipeline flow and the module test chamber. The inlet source gas pressure must be approximately 175 psia for proper regulation of the module pressure to the high-pressure test state of 150 psia. For this purpose, the pipeline source pressure must be 200 psia or higher. The flow rate of gas released from the module to atmosphere is manually adjusted to approximately 20 cm^3/min (using a rotameter and restrictor valve) at the low-pressure test state of 70 psia. The gas release flow rate at the high-pressure state is then approximately 90 cm^3/min. When the module is operated at 45 seconds per pressure test state, the average gas release rate to atmosphere is 60 cm^3/min, and a complete volumetric turnover of gas in the test chamber will occur within a 12-minute time interval.

The Gas Sensor and Control Module was designed and fabricated in 2003 to adapt the previous energy meter module for two-state operation. Figure 5-2 shows the sensor layout, identifying each sensor component. Figure 5-3 shows a photograph of the two-state Sensor and Control Module assembly. An electronic pressure controller (Brooks Instrument, Model 5866E) is used in the two-state measurement system to set the pressure in the integrated speed of sound and CO_2 measurement chamber to any pressure state between 70 and 150 psia. The electronic pressure controller includes a proportional-integral control to adjust and maintain the pressure in the measurement chamber in response to a 1-5 VDC voltage command supplied by the Master Control and Data Acquisition Module. A 0.5-micron inlet filter protects the electronic pressure controller from contamination.

The transmitters for pressure (Rosemount Model 3051CA, 0–150 psia) and temperature (Rosemount Model 3144P, 0–100°C) provide continuous analog current readout signals, and the carbon dioxide sensor (Vaisala Model GMP221B, 0-20 mol%) provides a steady analog current readout that is updated at 2-second time intervals. To obtain carbon dioxide measurements at concentrations up to about 3 mol% in the test gas, the carbon dioxide sensor readings at the 70 psia low-pressure test state are used. The ultrasonic speed of sound sensor employs a pulse-echo transducer having a resonance frequency of approximately 1 MHz to generate oscillatory sound wave pulses having a time duration of approximately 4 μsec. These pulses are generated by applying a short-duration voltage impulse to the transducer, causing it to ring at its resonance frequency. The excitation impulse has a maximum voltage of 180 V-pk and a time duration of 0.1 μsec. The pulse repetition rate is 40 pulses/sec.

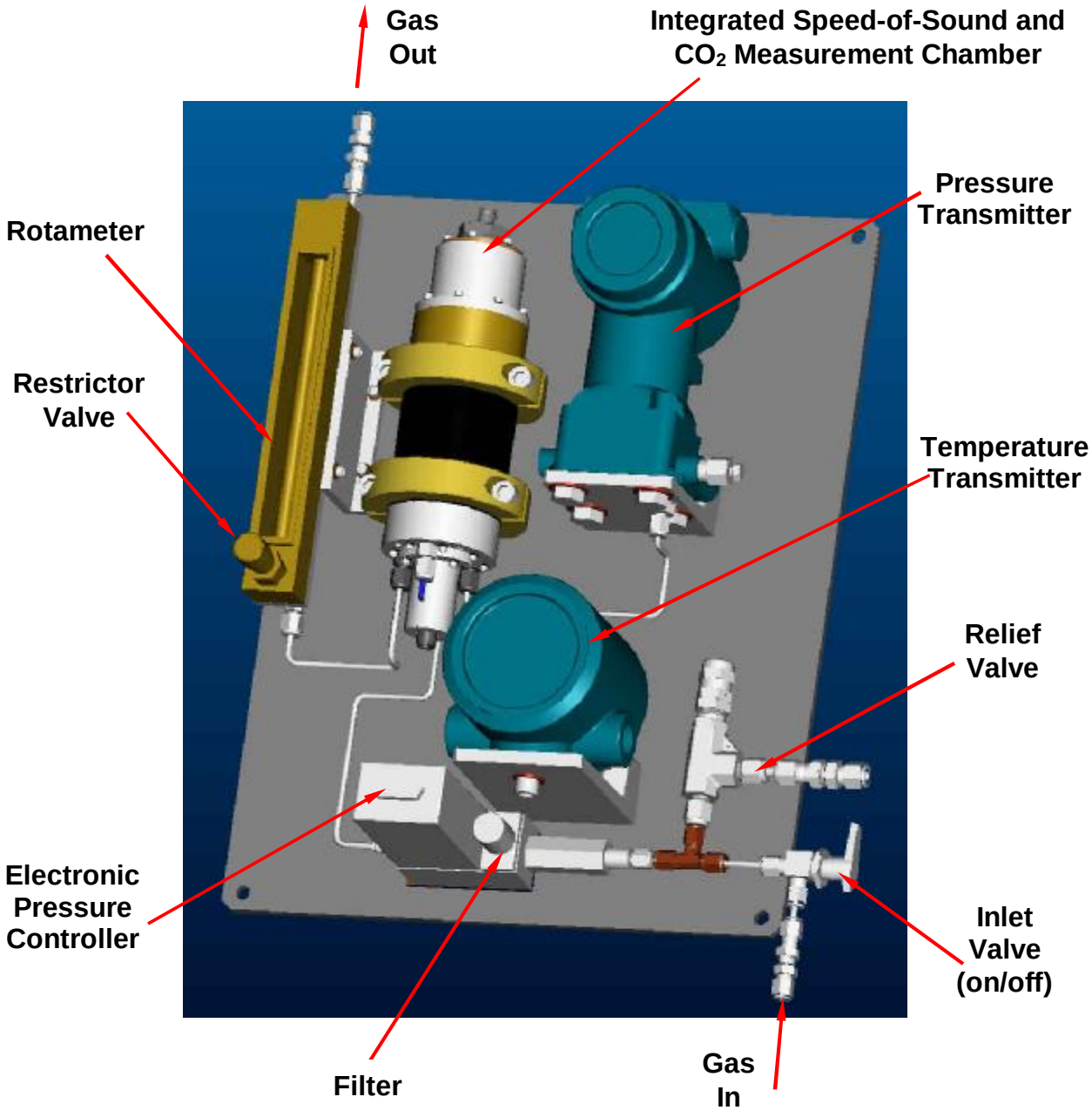

Figure 5-2. Gas sensor and control module component layout.

Figure 5-3. Assembled gas sensor and control module.

The ultrasonic signal receiver has a manually adjustable gain that is set for proper module operation at the pipeline installation site. The ultrasonic transducer is operated for only a few seconds near the end of each 45-second pressure state test interval. Power at 24 VDC is provided to the pressure, temperature, and carbon dioxide sensors, and at 15 VDC to the electronic pressure controller, from the Electronics and Communications Module.

5.1.2 Electronics and Communications Module

The Electronics and Communications Module shown in Figure 5-1 is a separate unit that may be mounted adjacent to the Gas Sensor and Control Module at the pipeline installation location or remotely connected via appropriate electrical cables. The sensor output circuits from the Gas Sensor and Control Module are routed through the Electronics and Communications Module to the Master Control and Data Acquisition Module. The clock section of the Electronics and Communications Module establishes the 50-MSample/sec A-D waveform sampling rate, the 40-

pulse/sec ultrasonic pulse repetition rate, and other timing control functions used in the waveform averaging process. The received waveforms are converted to 12-bit digital form at a 50 MSample/sec sampling rate (20 nsec time sampling interval). Each waveform trace contains 5,000 sample-point words which, when fully acquired, are transferred to a memory buffer where up to 256 successive traces are accumulated to form a 256 repetitive-trace average. Upon completion of the trace average accumulation, the averaged waveform is available for digital transfer to the Master Control and Data Acquisition Module.

5.1.3 Master Control and Data Acquisition Module

The Master Control and Data Acquisition Module shown in Figure 5-1 is a separate unit that may be remotely connected to the Electronics and Communications Module via appropriate electrical cables. This module is equivalent to conventional flow computer units and portable data logger units currently in use in the natural gas industry, but as described below, it is augmented to perform additional data processing functions required for inferential gas energy analysis. This module contains a sensor monitor section that converts the analog sensor signals to digital form for use in the subsequent inferential gas energy analysis. The pressure and temperature sensor readings, expressed in engineering units (psia and °F), are transferred directly to the algorithm processing section. The carbon dioxide sensor readings, expressed in mol%, are compensated for nonlinear sensor response at the State 1 test pressure of 70 psia before transfer to the algorithm processing section. The master control section of this Module commands the electronic pressure controller in the Gas Sensor and Control Module to change pressure states at appropriate times after acquiring the sensor readings and ultrasonic waveforms collected during the preceding test state.

A digital communications interface is also controlled by the master control section of the Module to request and receive averaged ultrasonic waveforms stored in memory in the Electronics and Communications Module. Received waveform files are fed to the speed of sound processing section where they are subjected to cross correlation analysis to obtain, as a first analysis step, the normalized correlation function between the two ultrasonic pulse reflections. This correlation function is then subjected to a second analysis step in which a regression is applied to fit a fine-resolution second-degree polynomial curve to the positive coherence lobe of the cross correlation function. The fitted polynomial represents the best statistical definition of the coherence lobe in the presence of any contaminating noise in the ultrasonic pulses. The polynomial also provides a means for numerically calculating the time-axis coordinate of the vertex of the polynomial curve, which corresponds to an accurately interpolated value of the correlation coherence lag time for the two reflected pulses. The sound speed in the gas at each pressure-temperature test state is then calculated by dividing the two-way reflection path distance by the derived time separation (correlation coherence lag time) between the two pulses. After the speed of sound in the test gas is computed for the two test states, these data and the associated pressure, temperature, and carbon dioxide sensor readings are input to the two-state inferential gas energy algorithm to derive the nitrogen concentration, the molecular weight, and the standard volumetric heating value of the test gas. These quantities, together with the carbon dioxide concentration, form the principal set of gas properties determined by the two-state gas energy measurement method.

Other useful parameters and system diagnostics are also derived from these data and the associated interim algorithm results, including standard gas density, gas compressibility, speed of sound at standard conditions, ambient module temperature, primary power fluctuations, module inert gas purge supply level, and date/time of data acquisition. These data are stored in nonvolatile memory for later download, and are also recorded on 3½-in. magnetic disk for archival data storage and retrieval. Primary power at 115 VAC is furnished to the Electronics and Communications Module via the Master Control and Data Acquisition Module. An external portable computer interface is provided at the Master Control and Data Acquisition Module to allow the energy meter system to be programmed to operate at specified pressure-step values, to adjust the data acquisition time intervals, to adjust the ultrasonic receiver gain and/or ultrasonic waveform averaging count, and to specify the stored and archived gas monitoring data parameters and other energy meter system diagnostic parameters.

5.2 INTEGRATED SOS AND CO_2 TEST CHAMBER

An integrated speed-of-sound and CO_2 measurement test chamber was designed and fabricated in 2003, based on the previous energy meter work and chamber designs. This integrated chamber continues to take advantage of the capability to precondition the gas temperature and gas flow to provide stable and uniform conditions for accurate speed-of-sound and CO_2 measurements. Figure 5-4 shows the design layout of the integrated chamber, and Figure 5-5 shows a cutaway graphic of the integrated chamber.

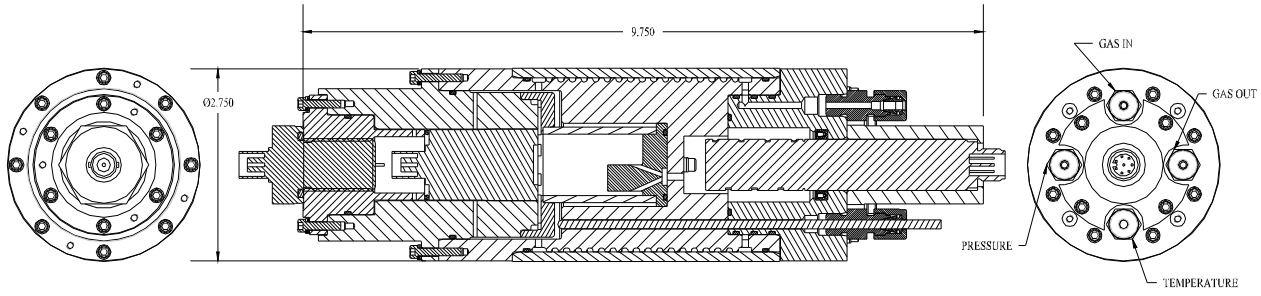

Figure 5-4. Design of the integrated speed-of-sound and CO_2 chamber.

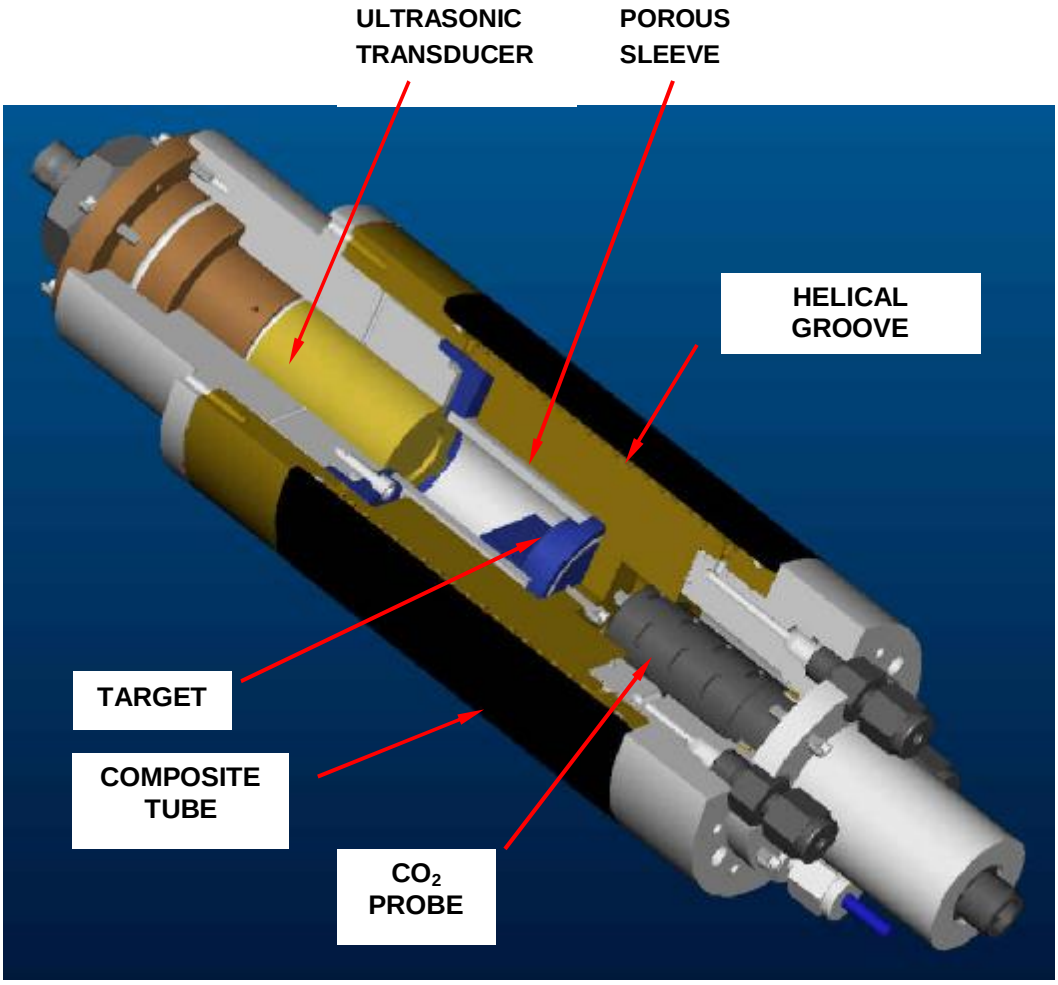

Figure 5-5. Cutaway graphic of the integrated speed-of-sound and CO_2 chamber.

Before entering the test volume of the integrated chamber, the gas travels through a covered helical groove machined into the outer surface of the aluminum chamber body that allows the gas to equilibrate to the temperature of the chamber. The integrated chamber acts as a semi-stable heat sink, subject to diurnal changes in ambient temperature. The helical groove is covered and pressure-sealed by a close-tolerance 0.125-in. thick cylindrical sleeve made of Black Almagon® graphite-epoxy material. The helical groove is 0.094 in. wide by 0.062 in. deep and provides an effective gas flow path length of approximately 125 in. which, for a gas throughput of 0.020 l/min laminar flow in the helical groove, gives a thermal equilibration dwell time of approximately 10 seconds. Because of this gas temperature preconditioning, the temperature of the gas entering the speed of sound measurement section of the test chamber is, for practical purposes, the same temperature as the body of the chamber. Upon exiting the helical groove, the gas enters an annular space formed by the inner chamber wall and a 0.1-in. thick porous sleeve made of 40%-density Duocel® aluminum foam. This porous sleeve serves as a diffusion interface to prevent the formation of any persistent gas circulation patterns in the chamber. An RTD temperature probe measures the gas temperature at the entrance to the annular space prior

to entering the sound propagation zone of the chamber volume. The overall length of the integrated speed of sound and CO_2 chamber is 9.75 in., and the outside diameter is 2.75 in.

The ultrasonic transducer is mounted entirely within the chamber, with small openings provided around the transducer housing to allow gas pressure to reach the back of the transducer and equalize the pressure on both sides of the active piezoelectric element. The chamber is designed to operate at pressures in the range of 50–200 psia, controlled by the electronic pressure controller. A machined dual-step reflector target is mounted opposite the transducer to provide two half-circle reflector faces having a 0.500-in. fixed separation distance. This target is made of Super Invar® material, which has a low coefficient of thermal expansion to minimize the effects of temperature on the reflector spacing. The distance between the transducer face and the nearest reflector face is designed to be 1.0 in., but may be made smaller by adding cylindrical spacers behind the target. The gas exits the speed of sound measurement section of the integrated chamber through ports in the reflector target and enters the CO_2 measuring volume of the integrated chamber.

The Vaisala Model GMP221B CO_2 probe that was used in the 2000-2001 energy meter module was selected for use in the 2003 integrated speed of sound and CO_2 chamber because of its superior technical specifications and advanced compensation design. The 0.73-in. diameter infrared absorption probe is mounted in one end of the integrated speed of sound and CO_2 chamber. The natural gas entering the CO_2 measuring chamber is output from the speed of sound section of the chamber and has already undergone temperature preconditioning prior to the speed of sound measurement. The CO_2 sensor probe passes through one end of the chamber and is sealed for pressure operation by a spring-energized seal. The CO_2 sensor probe is subject to the same gas pressure as is found in the speed of sound chamber (70-150 psia). However, the sensor is only activated for measurements during the 70 psia pressure state. The gas exits the integrated chamber via an outlet port located in the end of the chamber near the CO_2 probe.

Pressure and temperature measurement ports are located on the CO_2 probe end of the integrated chamber. As a result of the electronic pressure control and the low flow rate through the module, the test gas conditions in the speed of sound and CO_2 measurement sections of the chamber are maintained stable and uniform. The temperature and pressure of the gas in the chamber are measured and used in the energy analysis algorithm, and to correct the CO_2 sensor readings for variations relative to the sensor calibration reference conditions of 77°F and 14.696 psia.

5.3 DATA ACQUISITION AND CONTROL

The Master Control and Data Acquisition Module is designed to control the sequential operation of the energy meter pressure measurement states, activate the carbon dioxide and speed of sound sensors when required, monitor and record the pressure, temperature, and carbon dioxide sensor readings, and request, receive, and store the ultrasonic waveforms from the speed of sound sensor during each pressure testing state. The two-state testing sequence, requiring a nominal time period of 45 seconds at each state, represents the data acquisition cycle required to

determine the gas heating value and nitrogen diluent concentration. Certain computational operations using the data collected during the first testing state are performed during data collection in the second state. Similarly, computational operations using data collected and analyzed during both the first and second testing states are performed after the data acquisition process continues into State 1 of the next two-state testing cycle. In particular, the gas energy analysis in any given two-state testing cycle is completed during State 1 of the next two-state testing cycle.

Figure 5-6 presents a timing diagram describing the sequential functions performed by the Master Control and Data Acquisition Module during a complete two-state gas testing cycle. As shown in the figure, the initial action in the data acquisition sequence is to command the programmable pressure regulator to pressurize the Gas Sensor Module to State 1 and initiate pressure and temperature monitoring. The gas pressure and temperature in the test chamber undergo transient responses in attaining steady-state conditions in State 1. The pressure stabilization time, t_p, is typically in the range of 12-15 seconds for pressures of P_1 = 70 psia and P_2 = 150 psia, and the associated temperature stabilization time, t_t, is typically in the range of 20-30 seconds for both pressure states. The carbon dioxide sensor is activated at a time delay of approximately 15 seconds following the State 1 initiation command. This allows the sensor to stabilize its response to the carbon dioxide concentration at P_1 in advance of the recording of sensor readings. The pressure and temperature monitoring process during the State 1 stabilization period may be used to determine when gas pressure and temperature equilibration is complete, and thereby optimally initiate the subsequent data acquisition steps at State 1. Alternately, data acquisition at State 1 may be initiated after a preset time delay equal to or greater than the longest expected pressure-temperature stabilization time.

Following pressure and temperature stabilization at State 1, the Data Acquisition Window is activated, whereby the analog 4-20 mA pressure, temperature, and carbon dioxide sensor readings are collected at 2-second time intervals by the Master Control and Data Acquisition Module, scaled to engineering units in digital form (psia, ^oF, and mol%, respectively), and averaged over the Data Acquisition Window. The standard deviations of these readings are also computed to serve as Energy Meter system performance diagnostics. The State 1 Data Acquisition Window has a preset time duration in the range of 15-20 seconds.

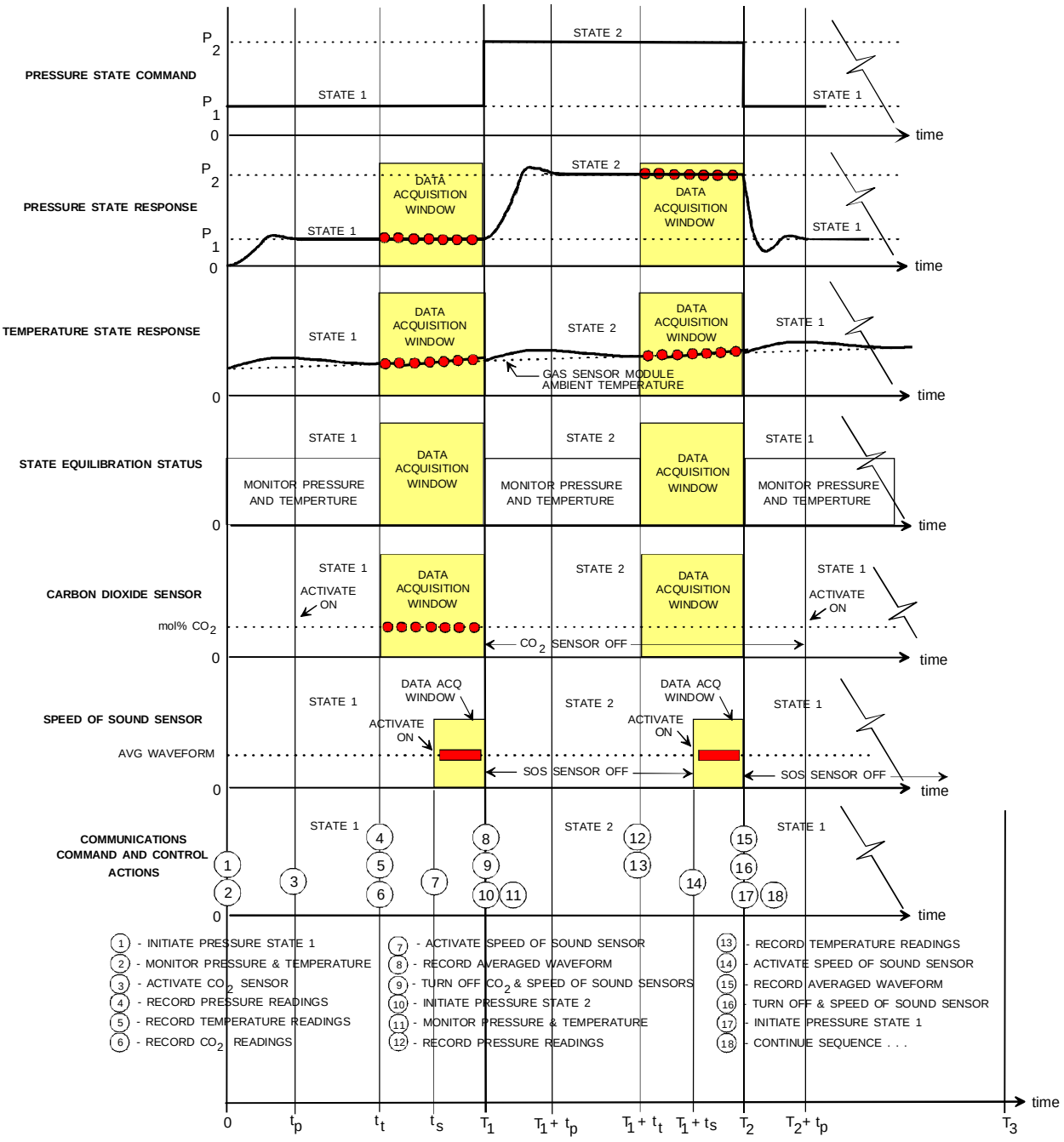

Figure 5-6. Data acquisition and control timing diagram for the two-state energy meter system.

During the second half of the Data Acquisition Window, the speed of sound sensor is activated at time t_s. At the ultrasonic transmitter pulse repetition rate of 40 pulses/sec, the speed of sound system collects repetitive sound reflection waveforms in 12-bit A-D converted form and sums these waveforms together in a signal-averaging buffer memory. This signal averaging process is programmable to provide averaging counts in powers of two ranging from 1 to 256. Adequate signal-to-noise ratios in the ultrasonic waveforms observed in most natural gas

mixtures are achieved using an averaging count of 256, requiring about seven seconds to acquire. At the end of the State 1 Data Acquisition Window, the Master Control and Data Acquisition Module requests and receives the averaged waveform in the form of a 5,000-word data file. The Master Control and Data Acquisition Module then deactivates the carbon dioxide and speed of sound sensors and commands the pressure regulator in the Gas Sensor Module to initiate pressure test State 2.

The data acquisition process at State 2 is equivalent to that at State 1, with the exception that the carbon dioxide sensor remains inactive during State 2. Figure 5-6 also illustrates the timing of the data acquisition events in State 2. Pressure changes between State 1 and State 2 occur as shown at times T_1 and T_2. Upon completing the data acquisition steps in State 2, the Master Control and Data Acquisition Module commands the pressure regulator in the Gas Sensor Module to initiate pressure test State1 to begin the next two-state test cycle. The time required to complete the data acquisition sequence for each two-state test cycle is approximately 90 seconds at testing pressures of 70 psia and 150 psia.

5.4 DATA RECORDING AND PROCESSING

Several data monitoring, data recording, and computational analysis functions are also performed during State 1 and State 2. Figure 5-7 illustrates these functions as they occur in the timing sequence shown in Figure 5-6. Dots in Figure 5-7 indicate data monitoring intervals in steps 1 and 7 and data recording events in steps 3-5, 16 and 17. Solid bars in steps 6 and 18 indicate transfer and recording of ultrasonic waveforms. Computations applied to pressure and temperature stability monitoring in State 1 and State 2, indicated by steps 2 and 8, are performed during each state. Computations applied to data recorded during State 1, indicated by steps 9-15, occur during State 2 (after time T_1). Computations applied to data recorded during State 2, indicated by steps 19-26, occur during the next State 1 (after time T_2). The computational operations are executed by compiled FORTRAN software routines applied to the recorded data files. The most intensive computations are associated with the waveform cross correlation calculations in steps 13 and 22 and the gas energy analysis in step 24. The sequence of all data processing computations performed in each pressure test state are expected to be completed within a time period less than the data acquisition and recording sequence in each test state. With computations related to data collected in State 2 performed during State 1 of the next two-state test cycle, the gas energy analysis results for each test cycle will be available within about 135 seconds or less after initiating each successive two-state test cycle.

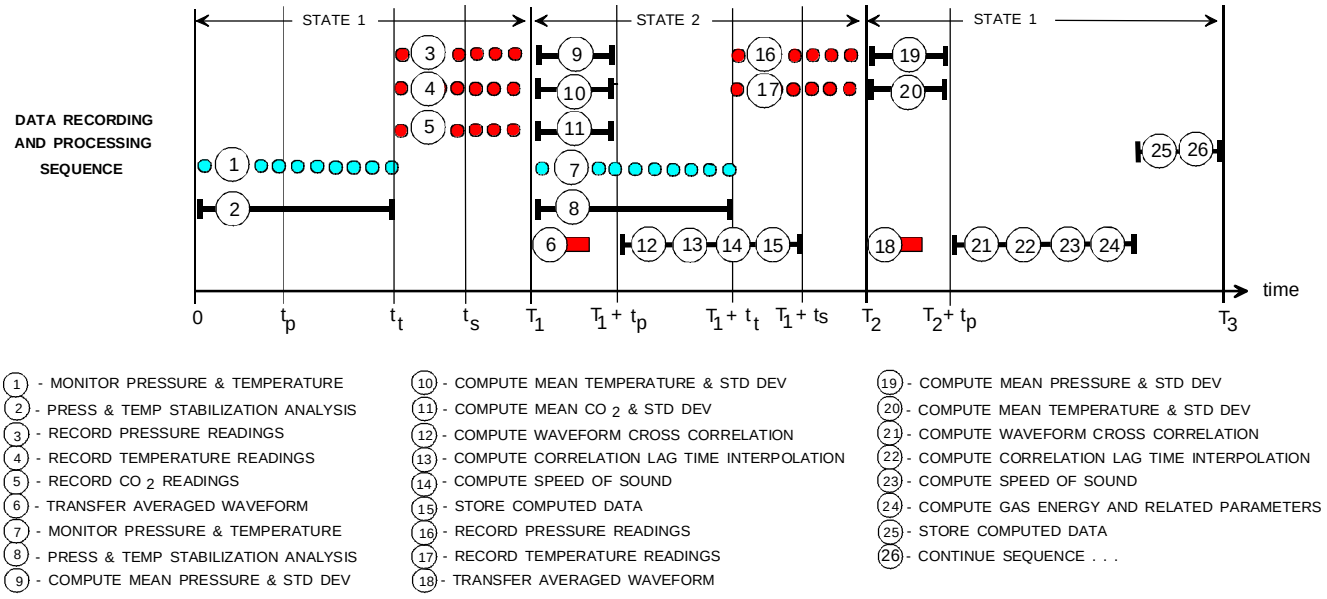

Figure 5-7. Data recording and processing sequence for the two-state energy meter system.

6. LABORATORY AND FIELD TESTING OF THE ENERGY METER MODULE AND ALGORITHM

6.1 LABORATORY TESTS OF THE SINGLE-STATE MODULE

In the energy meter development work of 2001, the module was tested in a laboratory setting to establish the sensors' accuracies and module capabilities. Carbon dioxide was added to standard transmission grade gas in various amounts (3.0, 6.0, and 9.0 mol%) to test the carbon dioxide and ultrasonic sensor and the algorithm capabilities under high concentrations of diluents. The testing was performed both indoors and outdoors, to study the module both in a room temperature setting and in fairly hot ambient conditions typical of south Texas in August. Through the results of the 2001 laboratory tests, sensor specifications and design parameters were developed and the module performance under indoor and outdoor temperatures was affirmed.

The laboratory tests for the 2002 project year were designed to determine the operational performance characteristics of the energy meter module, specifically in terms of gas diluent concentration and operating temperature and pressure. The module was tested under both "cold" and "hot" ambient temperatures to replicate temperature extremes common in field conditions, as well as in a mid-range temperature setting. These ambient temperatures were simulated using an environmental chamber available at Southwest Research Institute capable of providing a uniform temperature environment ranging from 40 to 120°F. The module operating pressure was also varied during the tests to determine the pressure and flow conditions for optimum sensor performance. Finally, gases with different amounts of nitrogen and carbon dioxide typical of transmission grade gas were used to study the effect of gas diluent concentrations on sensor performance and energy meter algorithm accuracy. By testing the effects of temperature, pressure and gas composition on the energy meter module, the laboratory tests established performance criteria that characterized the projected operation of the module in realistic field environments.

6.1.1 Test Conditions

The module was tested at three operating temperatures, 40, 80 and 120°F, and three operating pressures, 50, 75, and 100 psia. The high temperature was chosen based on the upper limit of summer temperatures in the United States. The low temperature reflected the lowest temperature that the natural gas blends used in the environmental tests could be subjected to without possible condensation of the heavier hydrocarbons within the energy meter module. The minimum operating pressure in the tests was selected based on the performance limit of the ultrasonic transducer in coupling acoustic energy into the gas. The regulated gas supply pressure in the speed of sound test chamber also determined the gas flow rate through the module; the vent flow rate to atmosphere was required to be set to approximately 200 ml/min when operating at 100 psia supply pressure. The nominal operating pressures and equivalent flow rates in the module for these tests are listed in Table 6-1.

Table 6-1. Laboratory test operating pressures and equivalent flow rates through the energy meter module.

Laboratory Test Pressures (psia)	Nominal Flow Rate through Module (actual liters/min)	Nominal Flow at Standard Conditions, 14.73 psia, 70°F (standard liters/sec)
100	0.208	0.0303
75	0.121	0.0235
50	0.107	0.0314

At the time of these environmental tests, the carbon dioxide sensor had not been tested or calibrated to operate at pressures above atmospheric conditions. Therefore, the CO_2 test chamber was located downstream of a needle valve at the outlet of the speed of sound chamber, to retain the specified operating pressure in the speed of sound measurements while regulating the gas flow to the CO_2 sensor to slightly above atmospheric pressure (~ 15.1 psia). The actual flow through the CO_2 chamber was equivalent to the flow at standard conditions listed in Table 6-1.

In addition to testing at various operational temperatures and pressures, eight different mixtures of natural gas were tested in the module. These mixtures were composed of the same base hydrocarbon mixture, but the nitrogen and carbon dioxide content was varied with respect to methane, the largest hydrocarbon component in the gas. The test gases were purchased from a calibration gas supplier who provided an accurate certificate of the gas composition, based upon gravimetric and gas chromatographic analysis. Table 6-2 shows the eight test gases with their various hydrocarbon and diluent concentrations.

Table 6-2. Eight certified test gas compositions used in laboratory tests of the energy meter module.

Component concentrations (mol%)	Test Gas 1	Test Gas 2	Test Gas 3	Test Gas 4	Test Gas 5	Test Gas 6	Test Gas 7	Test Gas 8
Nitrogen	0.253	0.251	0.250	5.517	7.028	5.519	7.006	3.057
Carbon dioxide	0.248	5.503	6.970	0.250	0.250	5.520	7.010	3.008
Methane	91.026	85.735	84.265	85.741	84.196	80.438	77.470	85.498
Ethane	5.845	5.892	5.904	5.867	5.900	5.896	5.900	5.833
Propane	1.504	1.498	1.493	1.504	1.506	1.504	1.495	1.488
Isobutane	0.402	0.402	0.401	0.403	0.401	0.403	0.403	0.400
N-butane	0.422	0.421	0.419	0.420	0.421	0.421	0.420	0.418
Isopentane	0.122	0.122	0.122	0.122	0.122	0.123	0.121	0.122
N-pentane	0.076	0.076	0.076	0.076	0.076	0.076	0.075	0.076
N-hexane	0.0695	0.0695	0.0695	0.0695	0.0695	0.0695	0.0695	0.0695
N-heptane	0.0232	0.0232	0.0232	0.0232	0.0232	0.0232	0.0232	0.0232
N-octane	0.0059	0.0059	0.0059	0.0059	0.0059	0.0059	0.0059	0.0059
N-nonane	0.0014	0.0014	0.0014	0.0014	0.0014	0.0014	0.0014	0.0014
Density (lb_m/scf) at 14.73 psia, 60ºF	0.0474	0.0514	0.0524	0.0491	0.0496	0.0530	0.0546	0.0504
Heating value (Btu/scf)	1107.07	1051.86	1038.43	1052.33	1037.63	999.32	969.12	1050.97

The total diluent content of each test gases ranged from 0.50 mol% to 14.0 mol%; most of the test gases contained at least 3.0 mol% carbon dioxide or nitrogen. The higher concentrations of nitrogen and carbon dioxide were intentionally selected to test the full-scale range of the sensors and the inferential algorithm. Figure 6-1 shows that four of the eight gases are outside of the algorithm design limits for total diluents, and six of the eight gases are outside of the range of diluents in typical transmission-grade gas. The gas compositions that exceeded the algorithm design limits provided a test of the energy meter module performance under high-diluent gas conditions more typical of production gases. Although transmission-grade gas doped to 9 mol% CO_2 was tested in the energy meter module during 2001, gases with high levels of nitrogen or high combined levels of nitrogen and carbon dioxide were not tested in the sensors prior to these laboratory tests.

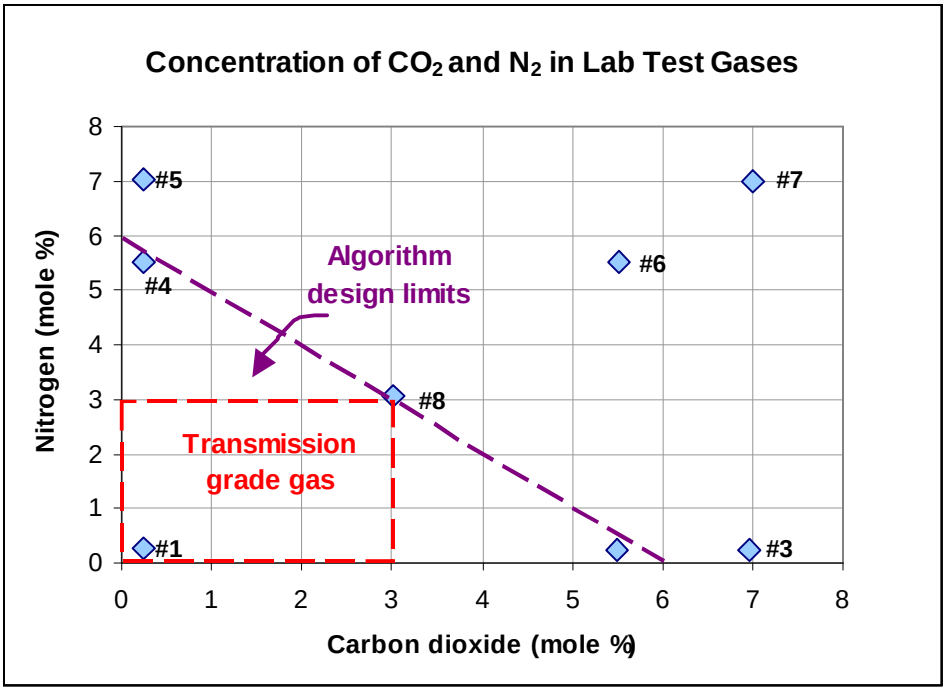

Figure 6-1. Concentrations of nitrogen and carbon dioxide in test gases with respect to energy meter algorithm design limits.

The laboratory test setup in the environmental chamber is illustrated in Figure 6-2. The energy meter module components exposed to controlled temperature conditions in the environmental chamber included the speed of sound test chamber, the CO_2 test chamber, the CO_2 sensor transmitter electronics, and separate pressure and temperature sensors and transmitter electronics in each sensor chamber. The speed of sound computer, which performed the ultrasonic signal generation, signal acquisition and analysis, was located outside of the chamber, as were the sensor data logger and a data transfer/storage laptop computer. The data logger recorded the pressure and temperature measurements for both sensor test chambers and the CO_2 sensor measurements at one-minute time intervals. Measurements from the speed of sound sensor were logged separately at five-second time intervals. Therefore, the test data were synchronized to within ±2.5 seconds of one another in the two data recording systems.

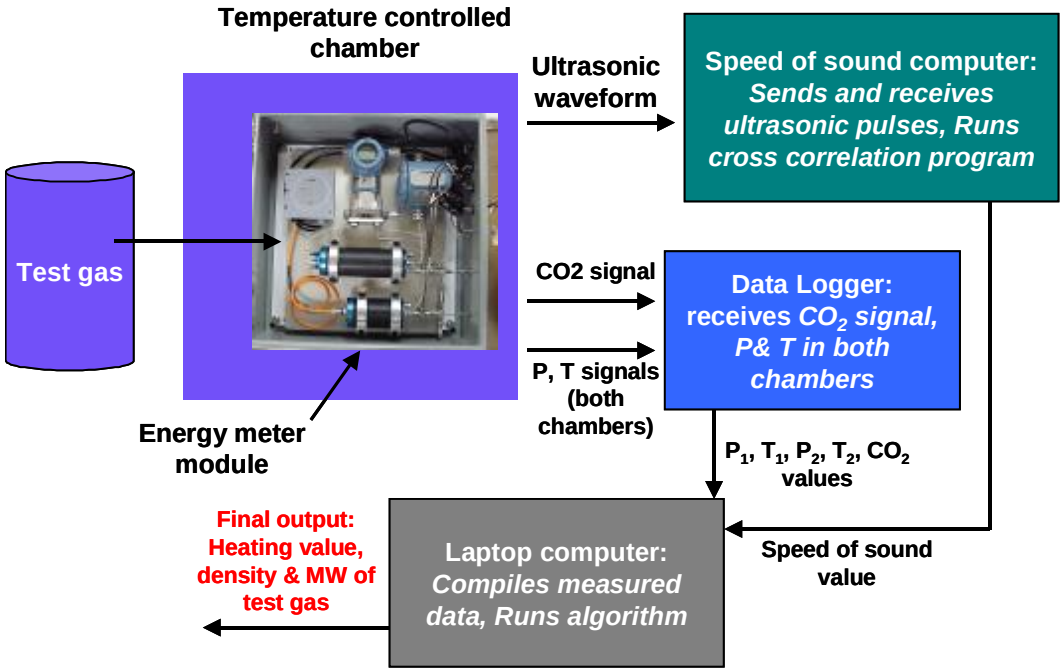

Figure 6-2. Laboratory test setup for environmental tests of the energy meter module.

6.1.2 Speed of Sound Sensor Results

The speed of sound test chamber and the ultrasonic transducer performed well under all of the various operational temperature and pressure conditions used in the laboratory tests. The ultrasonic transducer functioned adequately in generating and detecting the ultrasonic pulses in each of the tests, and the speed of sound computer, external to the environmental chamber, processed the data without problems. The speed of sound sensor provided measurements of the average speed of sound to within ±1.5 ft/s of computed values obtained using the SonicWare software package (Lomic [1998]) for the 40, 80, and 120°F temperature tests. Figure 6-3 and Figure 6-4 present the speed of sound sensor error over each fifteen-minute run for each test gas. As shown in these figures, a slight pressure bias occurred in both the low and the high temperature tests, but the error tolerance limits were maintained for all three test pressures across the spectrum of test gases. The gas compositions and high levels of carbon dioxide and nitrogen did not have a significant effect on the accuracy of the speed of sound measurements.

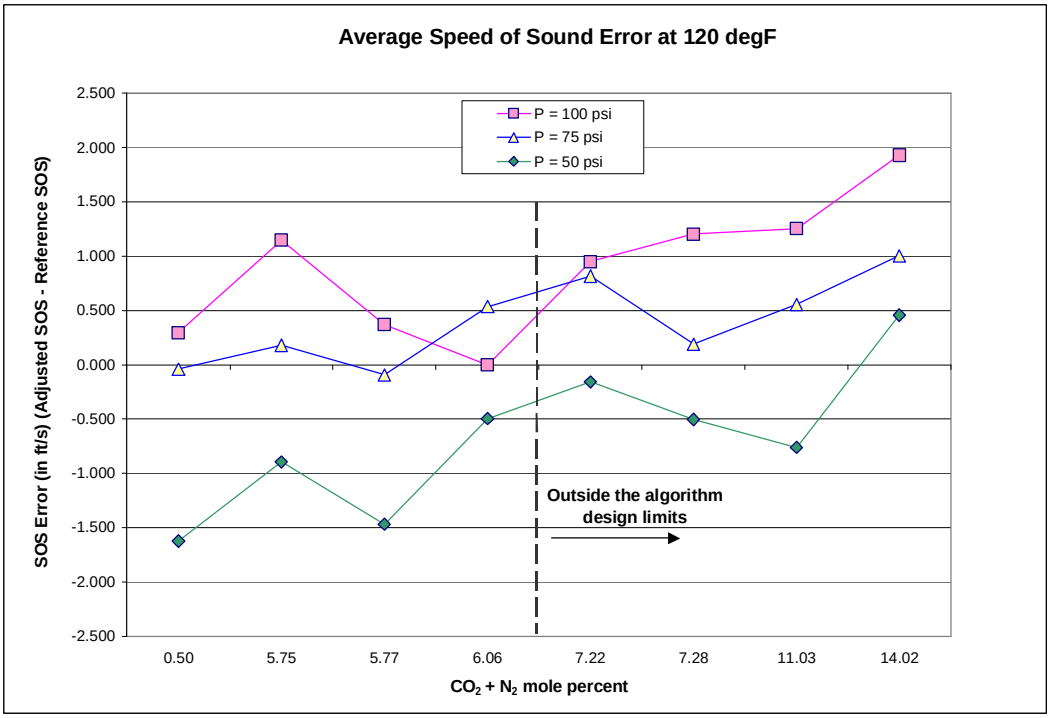

Figure 6-3. Average speed of sound errors in eight test gases at 120°F.

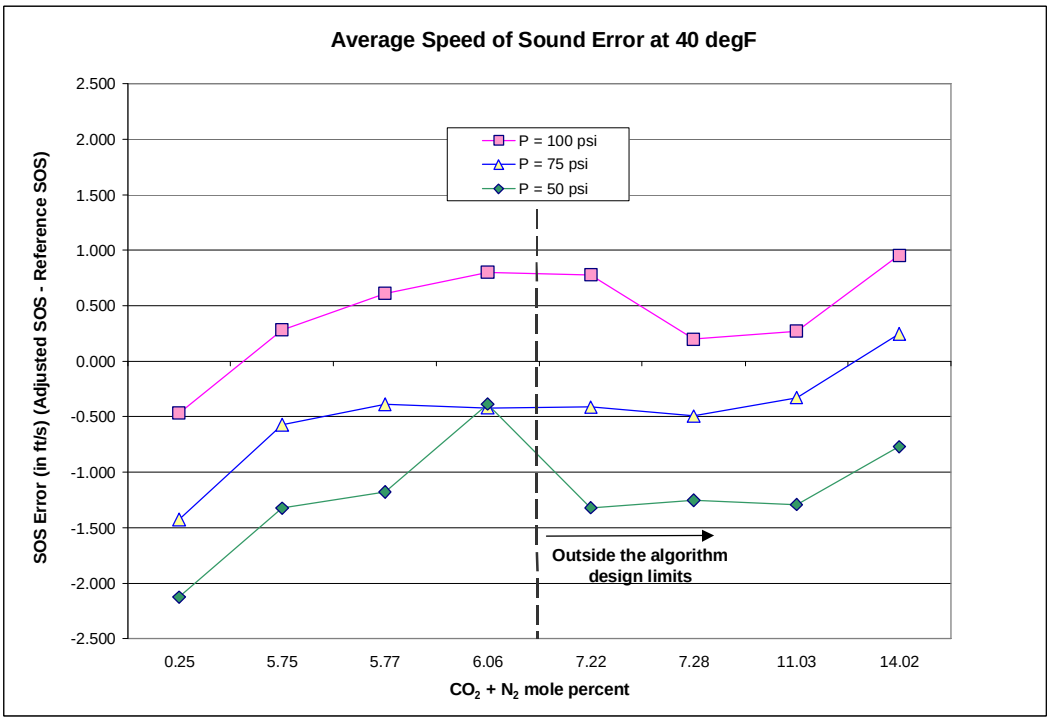

Figure 6-4. Average speed of sound errors in eight test gases at 40°F.

Despite the speed of sound sensor accuracy and the transducer functionality in the environmental temperature tests, a significant deficiency was detected in the performance of the ultrasonic transducer during these tests. The transducer did not provide uniform ultrasonic radiation and illumination of the reflection target faces within the speed of sound test chamber. Because of this nonuniform radiation pattern, the ultrasonic pulses reflected from the target faces were dissimilar, causing the cross correlation analysis to select the incorrect pulse time delay coherence peak for the reflected waveforms. Although errors of this type could not be prevented in the data analysis process, they were readily recognizable as 'cycle-skip' errors when they appeared in the recorded data and were manually removed before the final data analysis.

Figure 6-5 shows an example of two distorted reflected waveforms (top) caused by nonuniform radiation and the associated cross correlation function (bottom) for speed of sound measurements in test gas #8 at 80°F and 100 psia. As this figure reveals, two weaker but distinct ultrasonic reflections are present in the waveforms. These added pulse shape features produce secondary side envelopes in the cross correlation function. The principal dissimilarity in the two waveforms is the unequal number of cycles in the leading parts of the reflected pulses. This distortion tends to stretch the central envelope of the cross correlation function on the time-lag axis, resulting in the main correlation peaks being very comparable in amplitude. When this occurs, the speed of sound computer may select the "wrong" peak (i.e., the second highest peak rather than the highest peak in Figure 3-3), thus introducing a 'cycle-skip' error in the speed of sound reading. Based on the exhibited degradation in the ultrasonic transducer, additional bench tests were performed on the ultrasonic transducer to validate its nonuniform radiation pattern, and a requirement for beam pattern uniformity was added to the new transducer specifications for the 2002 project. The details of these ultrasonic transducer tests are discussed in Chapter 3.

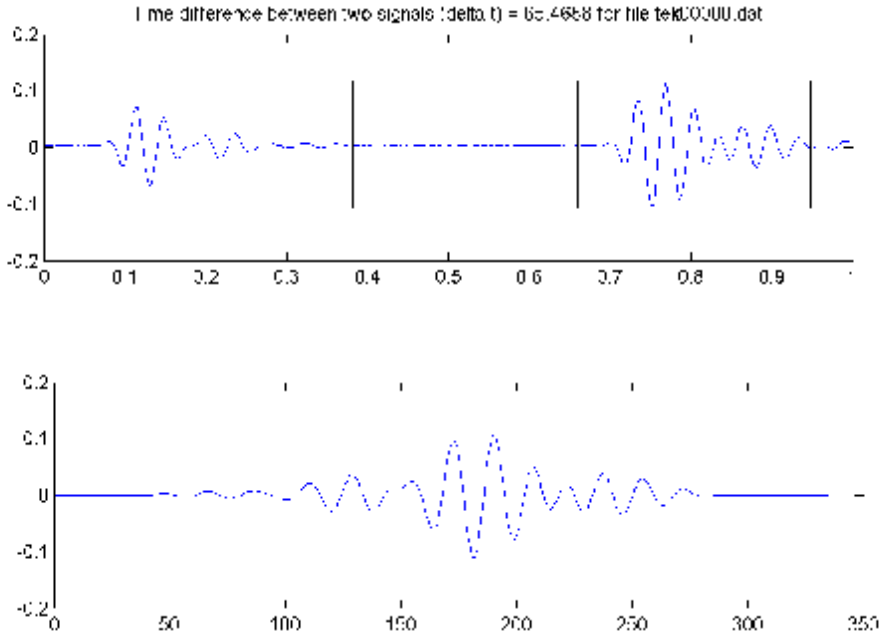

Figure 6-5. Ultrasonic waveform of first and second reflections for test gas 8 at 80°F and 100 psia (*top*); cross correlation function generated by the reflections (*bottom*).

The speed of sound errors occurred occasionally in the low and high temperature tests, but more frequently in the readings recorded for the mid-range temperature tests. In general, the tests at 80°F revealed less accuracy in the sensor determination of the sound speed. Figure 6-6 shows the results of the mid-range temperature tests. The disparity in accuracy between the tests at 40 and 120°F and the tests at 80°F is a direct consequence of the degradation in the ultrasonic transducer and, as indicated by the test results at other temperatures, should not be considered an inherent operational deficiency of the speed of sound sensor at mid-range temperatures.

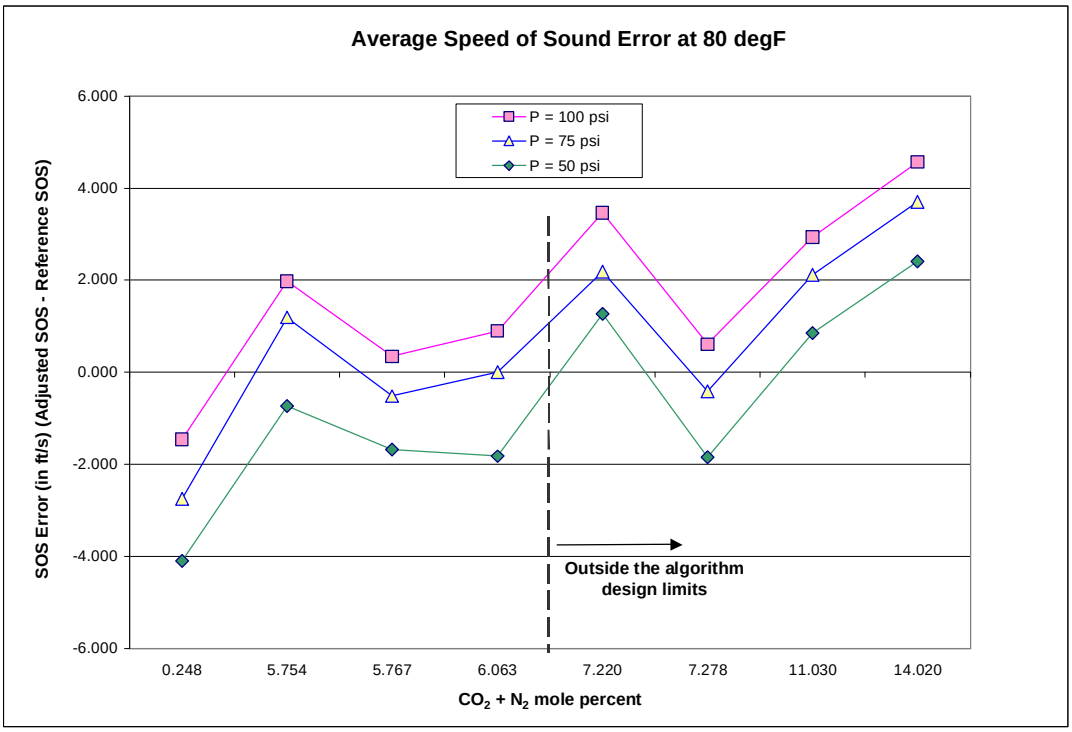

Figure 6-6. Average speed of sound errors in eight test gases at 80°F, exhibiting increases due to distortion of the ultrasonic transducer radiation beam.

Individual speed of sound sensor readings were recorded at 1-minute time intervals for each fifteen-minute test run in the eight test gases. Figure 6-7 through Figure 6-9 show sequential sensor reading errors in each test gas at 100 psia and all three test temperatures. The first five sensor readings in these figures should be disregarded because of the transitional purging of the preceding test gas and the associated stabilization time. Beyond this transition period, the readings fluctuate more and the measurement error increases as the operational temperature is increased. At 40°F and 80°F, the speed of sound error is within ±0.5 ft/s of the reference value, while at 120°F the sensor error variation is more pronounced, increasing to ±1.0 ft/s in some cases. Though the 120°F error averages were approximately equal to the 40°F error averages, the precision and steadiness of the sensor readings is poorer at the higher temperature. The same error trends observed in the high temperature test at 100 psia were also observed in the 50 and 75 psia pressure tests.

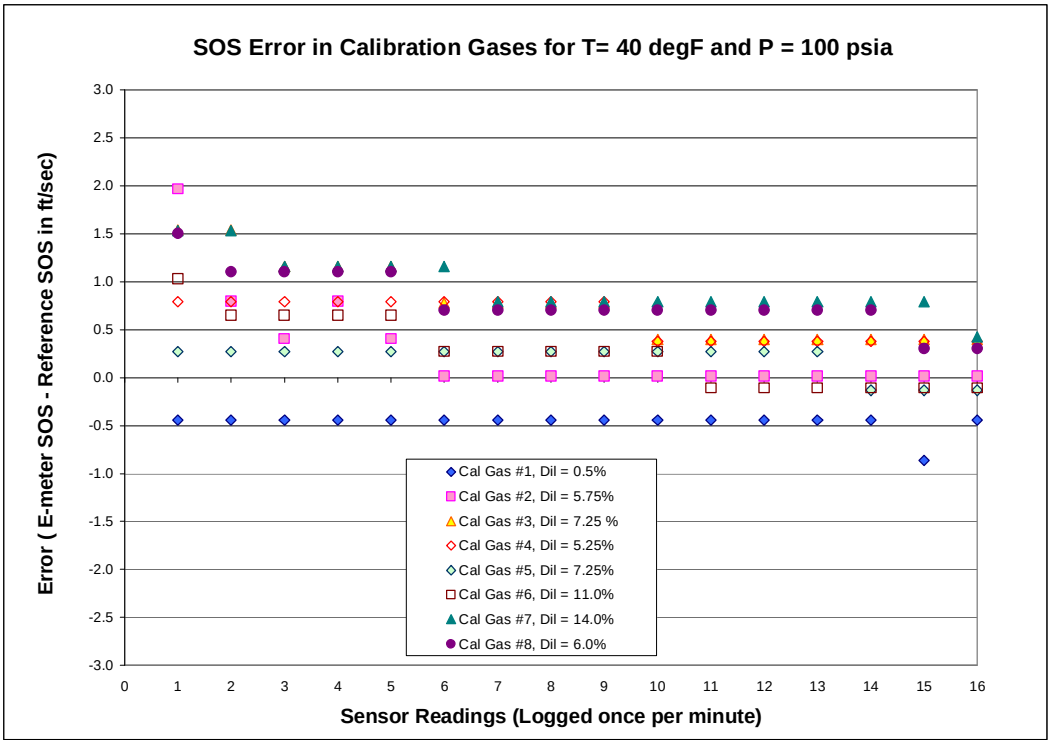

Figure 6-7. Errors in sound speed sensor measurements for eight test gases at 40°F and 100 psia.

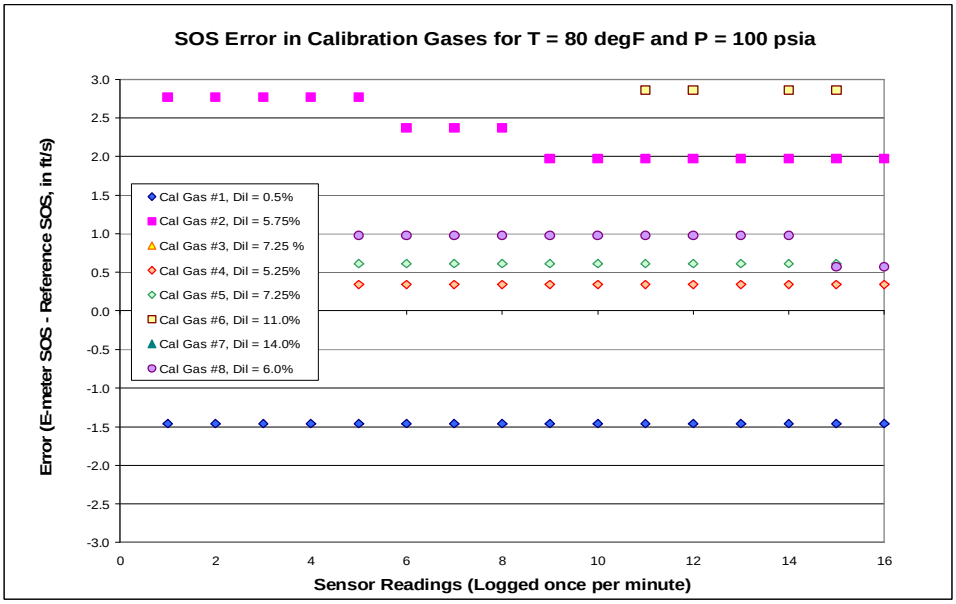

Figure 6-8. Errors in sound speed sensor measurements for eight test gases at 80°F and 100 psia.

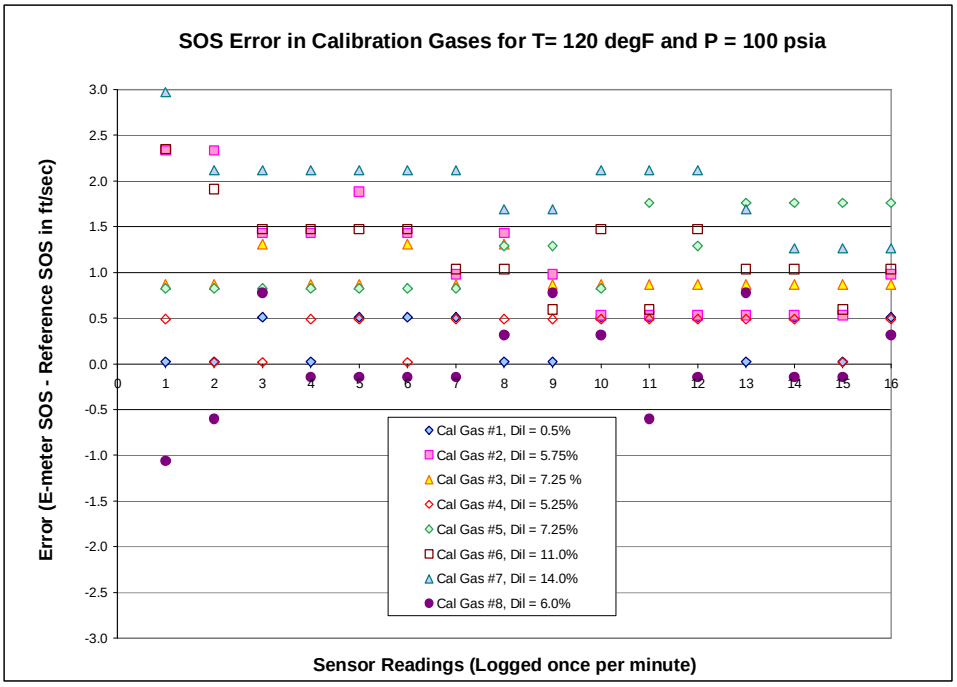

Figure 6-9. Errors in sound speed sensor measurements for eight test gases at 120°F and 100 psia.

The increase in speed of sound sensor errors at higher temperatures is primarily caused by alterations in the reflected ultrasonic pulse waveforms at different temperatures. Different ambient temperatures apparently affect the transducer radiation, as may be observed in the waveforms recorded for a particular test gas at the three test temperatures. Figure 6-10 and Figure 6-11 show the two reflections from the transducer at 40 and 80°F in test gas #4 at a pressure of 100 psia. The waveforms recorded at 40°F were somewhat higher in amplitude and required an adjustment in receiver gain for convenient display; however, the waveform shapes are noted to be affected by temperature. The waveforms at 40°F have excessive "ringing" in the trailing secondary pulse, making the first pulse arrival time and the pulse envelope itself less distinct and effectively reducing their bandwidth. These trends toward increasing amplitude interference from the trailing parts of the reflected pulses did not cause disruptive speed of sound measurement problems in the laboratory tests described here, but at temperatures below 40°F the problem could become more severe. In contrast, the waveforms at 120°F have significantly less secondary ringing and interference following the first pulse arrival. The indicated performance limitations of the ultrasonic transducer have led to specifications for an improved transducer design developed for more stable operation over a wider temperature range, typically 0 – 140°F.

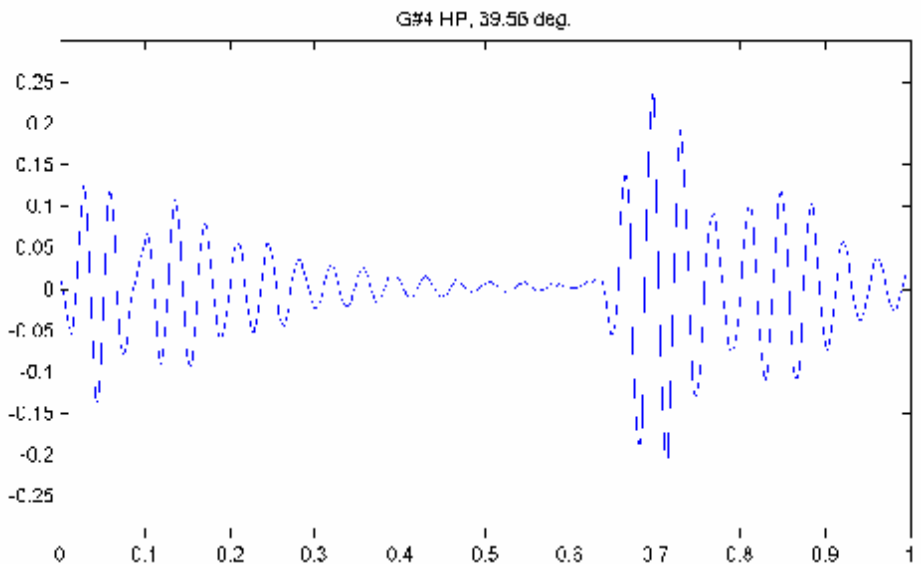

Figure 6-10. First and second reflected waveforms for test gas #4 at 40°F and 100psia.

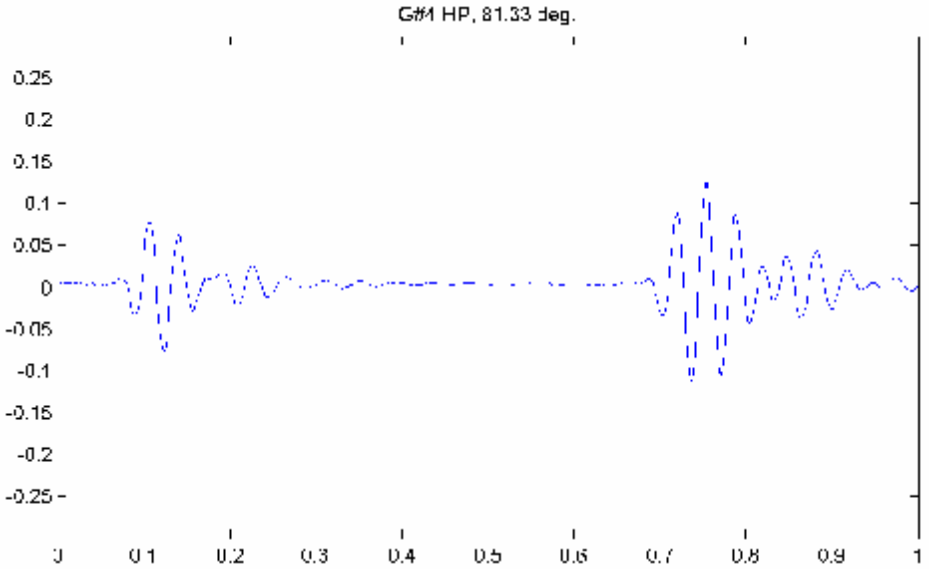

Figure 6-11. First and second reflected waveforms for test gas #4 at 80°F and 100psia.

The laboratory tests were beneficial in characterizing the ultrasonic transducer performance over a useful range of temperatures and pressures. The speed of sound sensor performance and accuracy was maintained over a reasonably wide range of operating temperatures (40 to 120°F) and operating pressures (50-100 psia). Operating pressure did not appear to affect the sensor performance, though a slight pressure shift was noted. However, the sensor operating temperature had a noticeable affect on the sensor performance by altering the shape of the reflected ultrasonic waveforms at the lowest test temperature and by affecting the steadiness of the sensor readings at the highest test temperature. In addition, the laboratory test results revealed that differences in the eight test gas compositions had only slight, if any, effects on the

speed of sound sensor measurements. Based on these tests, the speed of sound sensor performs well in natural gas mixtures containing low and high concentrations of nitrogen and carbon dioxide diluents in the range of 0.50 to 14.0 mol%. The accuracy and stability of the speed of sound sensor in such high diluent environments supports the possible future development of the energy meter for use in production-grade pipeline applications.

6.1.3 Carbon Dioxide Sensor Results

The carbon dioxide sensor used in the energy meter module was a commercial unit (Vaisala Model GMP-221, 10 mol% FS) designed and calibrated for normal operation at standard pressure and temperature. For use in the energy meter module, this sensor was adapted to operate at near atmospheric pressure within the carbon dioxide sensing chamber. The sample gas passing through the speed of sound test chamber also passes through the CO_2 test chamber via a preset metering needle valve that maintains the sensor pressure at approximately 15 psia. The CO_2 sensor chamber contains dedicated pressure and temperature sensors by which the sensor calibration may be adjusted to provide more accurate measurements of CO_2 concentrations. Although the metering valve is effective in reducing the gas supply pressure to approximately one atmosphere in the CO_2 test chamber, the supply pressure governs the gas flow through both test chambers, making the response time of the CO_2 sensor dependent on the module supply pressure. Following these laboratory environmental tests, additional work was performed to extend the operating pressure range of this CO_2 sensor to approximately 70-80 psia, to allow it to be an integral part of the speed of sound sensor chamber and thereby eliminate the need for a separate CO_2 test chamber.

Figure 6-12 through Figure 6-14 present the CO_2 sensor readings for recorded fifteen-minute test runs conducted on the eight gases at operating conditions of 75 psia and 40, 80, and 120°F. These data are corrected for temperature and pressure in the CO_2 test chamber using the conventional linear temperature scaling adjustments recommended by the sensor manufacturer. The data points represent sensor readings taken at one-minute time intervals. The figures are shown on the same scale for accurate comparison. In some of the curves, the sensor readings do not become stable until late in the test run because of the transition time required to purge the previous test gas from the chamber. The sensor error results shown in these figures at the module operating pressure of 75 psia were essentially the same as those observed at pressures of 50 and 100 psia, since the CO_2 chamber pressure was regulated to approximately 15 psia in each case

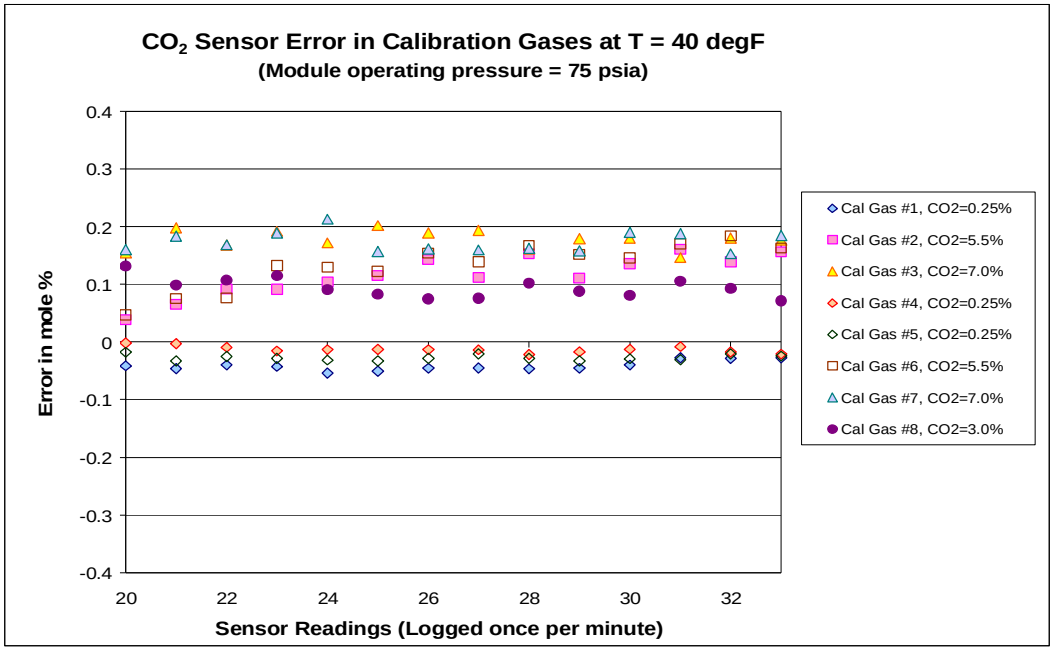

Figure 6-12. Carbon dioxide sensor measurement errors for test runs at 40°F and 75 psia.

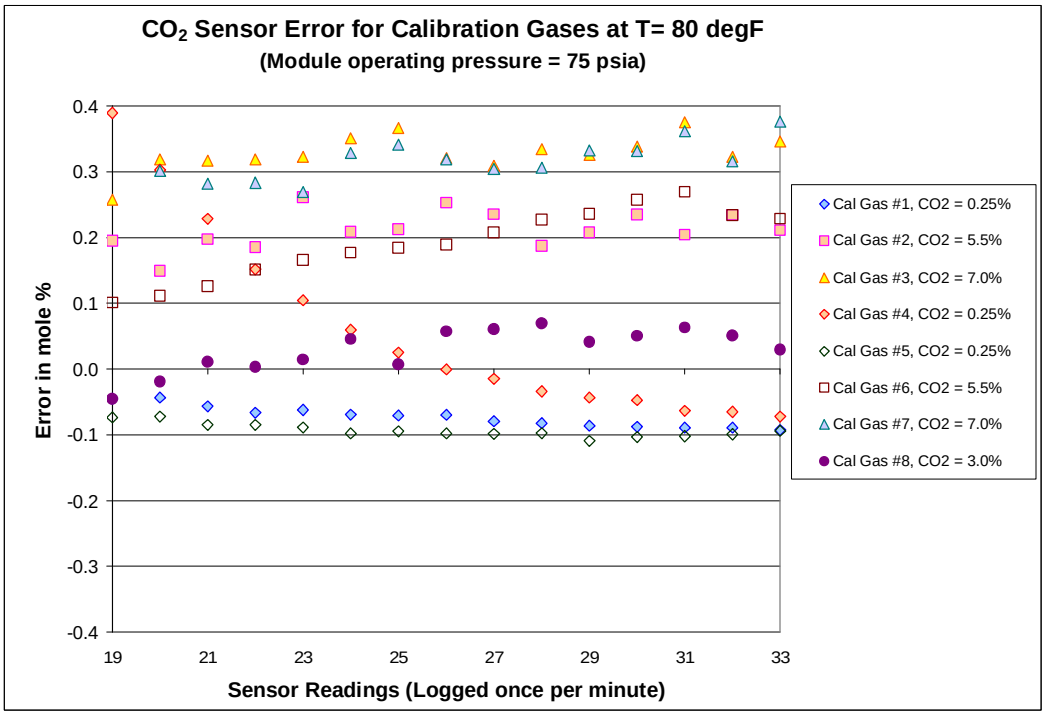

Figure 6-13. Carbon dioxide sensor measurement errors for test runs at 80°F and 75 psia.

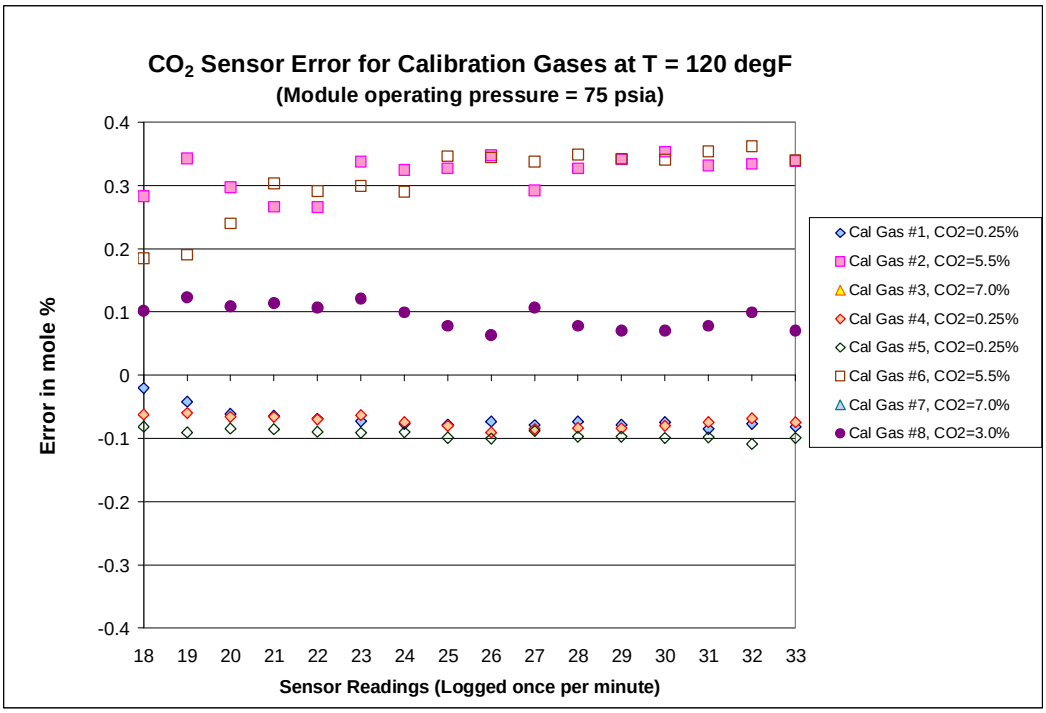

Figure 6-14. Carbon dioxide sensor measurement errors for test runs at 120°F and 75 psia.

These figures indicate relatively well stabilized CO_2 sensor readings, especially during the last half of each test run, but also show increasing variability and a tendency for increasing error offsets in the test gases having higher CO_2 concentrations. In particular, the readings for the four test gases having concentrations of 3 mol% CO_2 and lower, the two test gases having 5.5 mol% CO_2, and the two test gases having 7 mol% CO_2, respectively, tend to cluster together in the plots for the three test temperatures.

Figure 6-15 shows the average carbon dioxide sensor errors derived from each 15-minute run for the eight test gases before application of the linear corrections for operating temperature and pressure. In these plots, the average errors apply to three test gases having 0.25 mol% CO_2, one test gas having 3.0 mol% CO_2, two test gases having 5.5 mol% CO_2, and two test gases having 7 mol% CO_2, with the module supply pressure set at three pressures (50, 75, and 100 psia) and three temperatures (40, 80, and 120°F). The metering valve between the CO_2 chamber and the speed of sound chamber was adjusted to provide a pressure of approximately 15 psia in the CO_2 chamber at a nominal flow rate of 200 ml/min with the module supply pressure and temperature at 75 psia and 80°F, and was not changed throughout the tests on the eight gases. The resulting pressure and flow rate in the CO_2 chamber were in the range of about 15.0 to 15.15 psia and 160 to 240 ml/min, respectively. The uncorrected pressure dependence of the sensor can be interpreted from Figure 6-15 by comparing the curves having different line styles. The uncorrected temperature dependence of the sensor is indicated in Figure 6-15 by the three groups of common-color curves for temperatures of 40, 80, and 120°F. These curves indicate that the accuracy of the sensor response to increasing concentrations of carbon dioxide is roughly proportional to the sensor reading but is also significantly dependent on the gas temperature as

the predominant variable in the tests. In particular, the less dense (higher temperature) gases appear to the sensor to contain a greater CO_2 content than their actual concentrations.

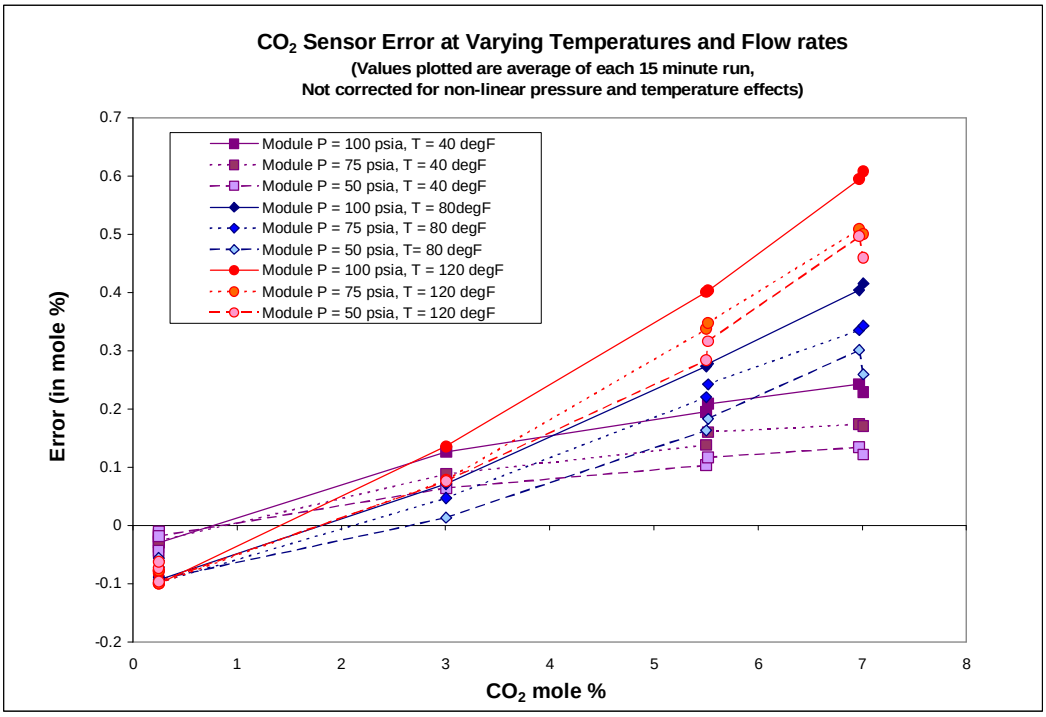

Figure 6-15. Average carbon dioxide sensor error at three test temperatures and pressures. For each test, the carbon dioxide sensor was operated at atmospheric pressure, while the module supply pressure was held at the indicated value. No temperature or pressure calibration corrections have been applied to the results.

On applying the linear corrections described in Section 4.1 for test gas temperature and pressure, the sensor errors in Figure 6-15 were reduced to within the energy meter module specification of ± 0.05 mol%, except for the gases having the highest CO_2 content. Figure 6-16 shows the residual error in the sensor response after applying these corrections at the module operating pressure of 75 psia. For the 40°F and 80°F tests, the errors are within the ± 0.05 mol% limit for all test gases. The error in the high temperature test is slightly greater than the sensor error limits for gases having more than 3 mol% CO_2, indicating that a more comprehensive nonlinear calibration correction is needed. Chapter 4 presents a complete description of the CO_2 sensor calibration process, including the linear temperature and pressure corrections applied above and nonlinear corrections required for operating the sensor at pressures in the range of 50-70 psia.

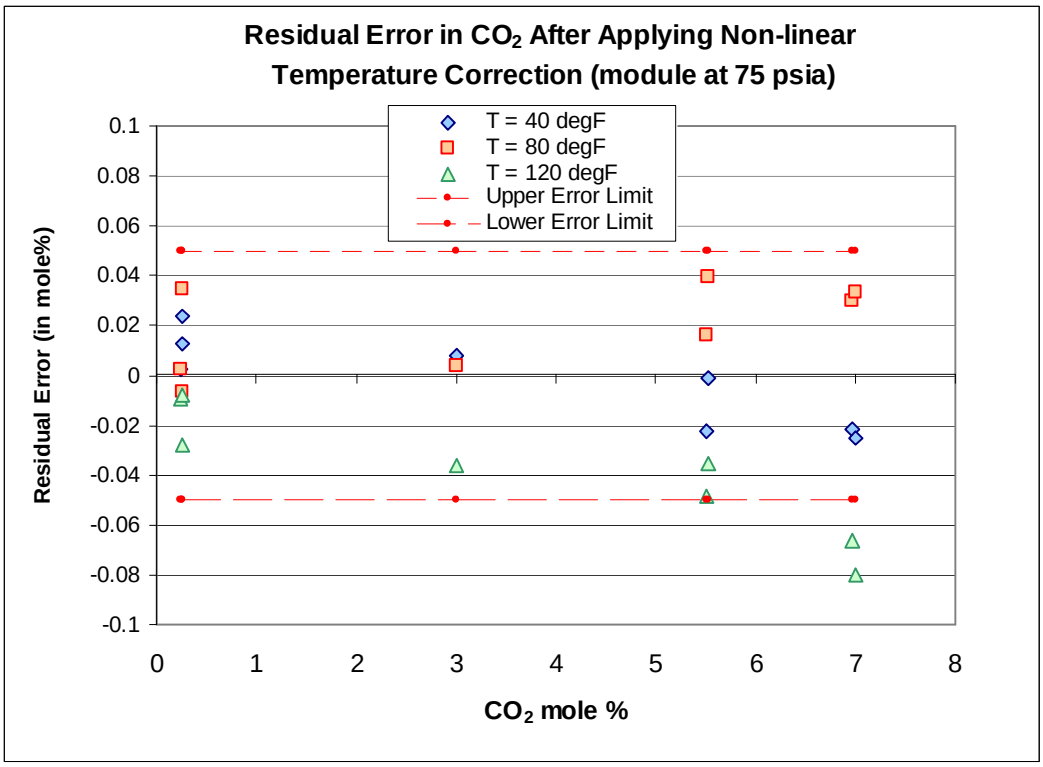

Figure 6-16. Residual error of carbon dioxide sensor after nonlinear temperature correction based on gas composition, at 75 psia.

These laboratory tests on the prototype energy meter module provided insight into the effects of operational temperature and carbon dioxide concentration on the CO_2 sensor performance. With the sensor operating at its normal atmospheric pressure rating, the effects of temperature in the range of 40-120°F introduce errors as high as 0.6 mol% before the linear temperature and pressure corrections are applied. The effects of temperature can be corrected by the conventional linear temperature correction factor to within an error range of ±0.05 mol% for typical transmission grade gas having CO_2 content up to 5.5 mol%. Residual errors remained after applying the temperature correction, and were noted to be related to the carbon dioxide concentrations in the test gases. This error was most noticeable for gases having CO_2 concentrations of 7.0 mol% when the sensor was operating at 120°F. The more comprehensive nonlinear correction process developed in Chapter 4 is designed to compensate for the nonlinear CO_2 dependence as well as to permit the sensor to be operated at higher chamber pressures in the 50-70 psia range. The linearly corrected sensor readings at constant temperature and the three operating supply pressures of 50, 75, and 100 psia exhibited small but noticeable offset errors that also increase slightly with CO_2 concentration for all of the test gases. With no other variables present in the CO_2 sensor chamber, these effects are attributed to the differences in gas flow rate.

6.1.4 Heating Value Error and Overall Module Performance

Laboratory test data on the measured speed of sound and carbon dioxide content obtained with the energy meter module operating at controlled environmental temperatures, plus the known nitrogen content of each test gas, were analyzed using the algorithm to derive the volume-based heating values of the eight certified test gases. The relatively wide range of diluent gas concentrations in the test gases and the wide operating temperature range used in the tests provided a realistic basis for establishing the performance capabilities of the prototype energy meter module

Figure 6-17 and Figure 6-18 present the gas heating value errors for the eight test gases determined from data taken during each 15-minute test run at 40°F and 100 psia. Figure 6-17 shows that test gases #1 and #4, each containing 0.25 mol% carbon dioxide, have more steady readings versus time than those recorded for test gases #2 and #3, having 5.5 mol% and 7.0 mol% carbon dioxide. Neglecting the gas purging transition effects in test gas #2, the heating values for the gases with lower CO_2 content vary only by about ±0.30 Btu/scf, while the values for the higher CO_2 gases fluctuate within ±1.0 Btu/scf. Figure 6-18 is consistent with these results, showing that test gases #5 and #8, with less CO_2 content, exhibit less scatter in their readings than test gases #6 and #7 having higher CO_2 concentrations.

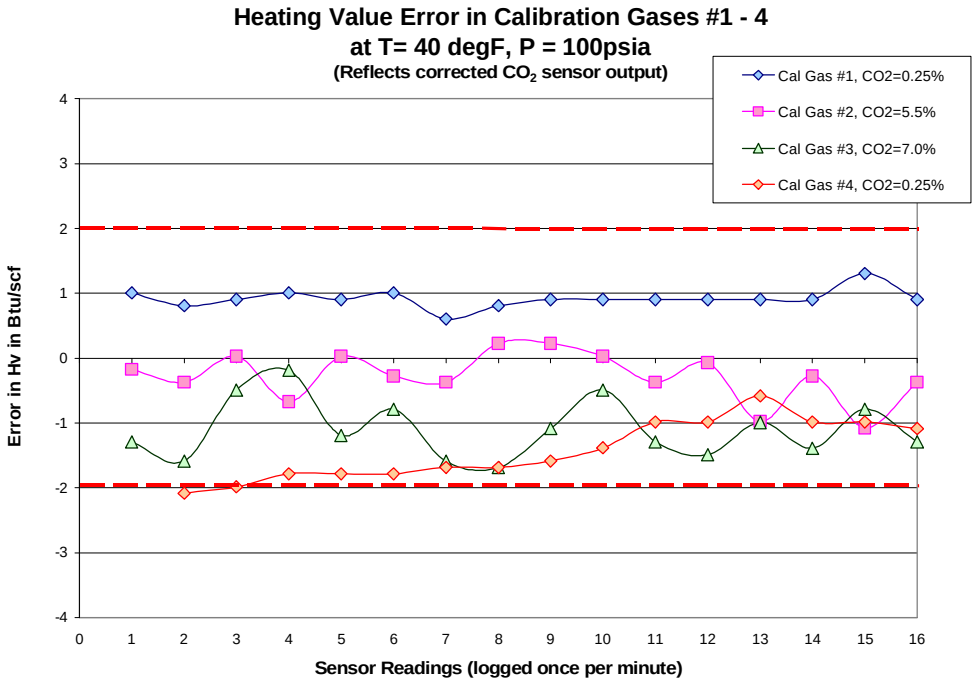

Figure 6-17. Heating value errors in test gases #1-#4 over 15-minute test runs at T = 40°F, P = 100 psia.

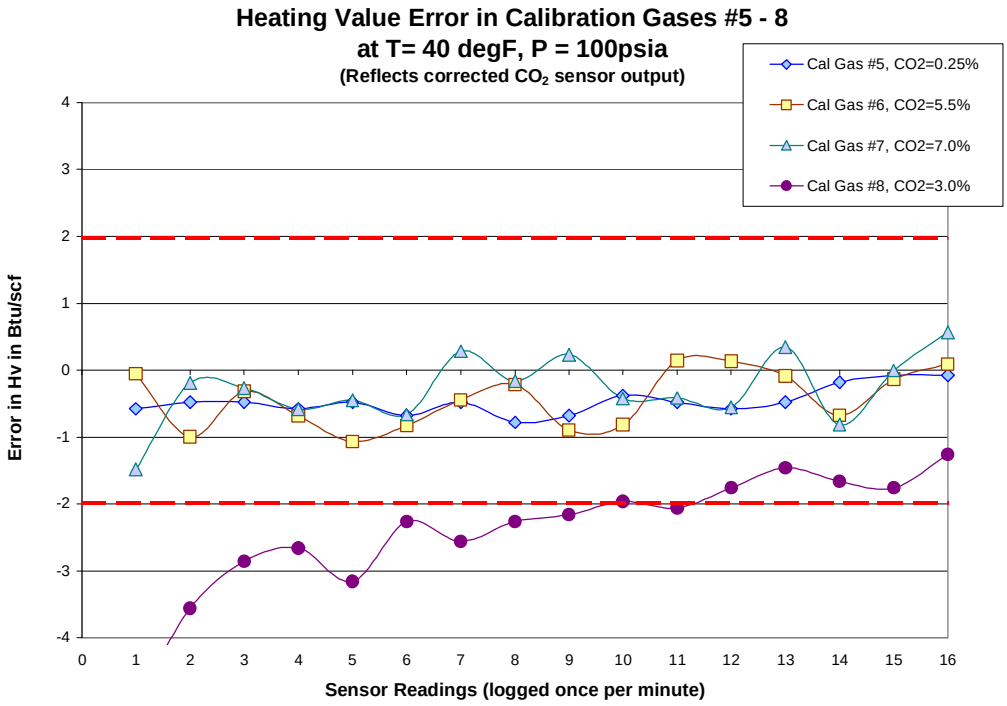

Figure 6-18. Heating value errors in test gases #5-#8 over 15-minute test runs at T = 40°F, P = 100 psia.

The increased heating value errors for the higher CO_2 gases are caused by offset shifts and scatter in the carbon dioxide sensor readings. As shown earlier in Figure 6-12 through Figure 6-14, the variations in the CO_2 sensor readings were higher for test gases #2, #3, #6, and #7, all of which have more than 5 mol% carbon dioxide. Figure 6-19 and Figure 6-20 show that tests of the same gases at 120°F exhibit similar trends in heating value error. However, the scatter in heating value for the test gases having higher carbon dioxide concentrations is still within the uncertainty limits of the algorithm. The resulting accuracy of the energy meter module is judged to be very good, considering the fact that the majority of the test gases contain diluent gas concentrations outside of the range of transmission-grade gas.

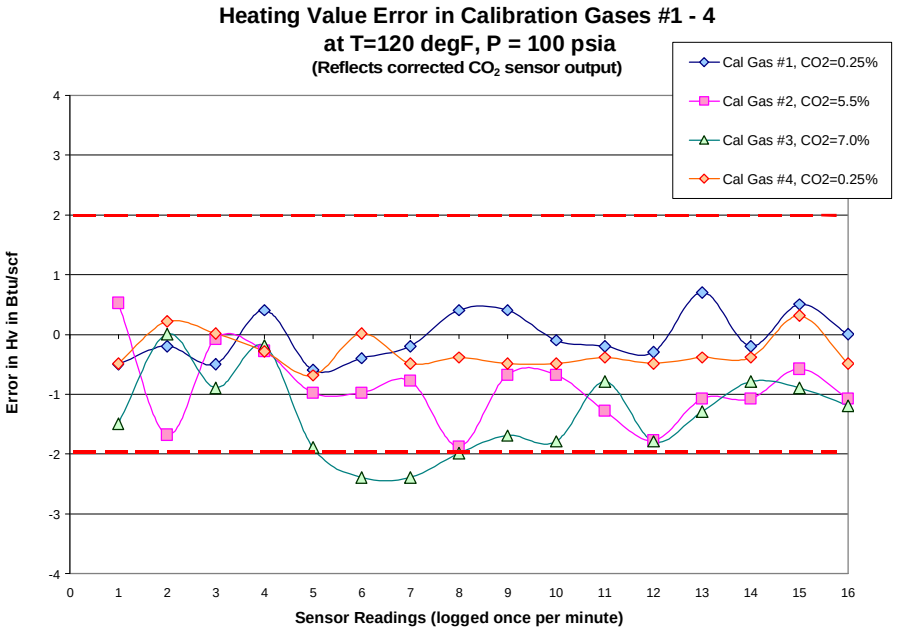

Figure 6-19. Heating value errors in test gases #1-#4 over 15-minute test runs at T = 120°F, P = 100 psia.

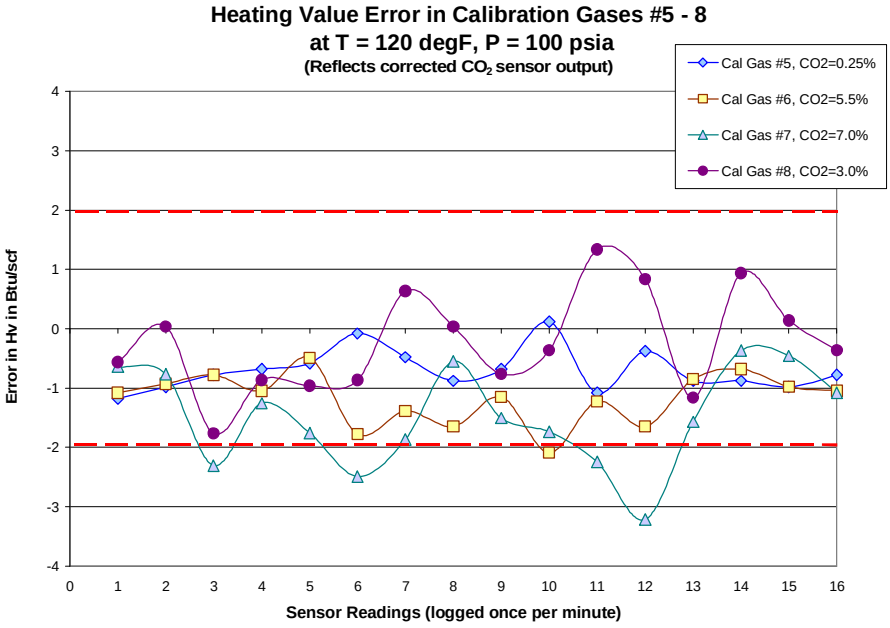

Figure 6-20. Heating value errors in test gases #5-#8 over 15-minute test runs at T = 120°F, P = 100 psia.

The effects of operating temperature on the performance of the module can also be seen by comparing Figure 6-17 with Figure 6-19 and Figure 6-18 with Figure 6-20. For example, test

gases #1 and #4 have very little scatter in their heating value results at the colder operating temperature, and greater fluctuations in their readings at high temperature. The scatter at 40°F for these low CO_2 gases is within ±0.30 Btu/scf, but grows to about ±0.50 Btu/scf at 120°F. For a higher CO_2 gas, such as test gas #7, the heating value error grows from about ±0.75 Btu/scf to about ±1.5 Btu/scf at 120°F. The increased scatter in the high temperature tests is a result of the increase in speed of sound sensor errors caused by temperature effects on the ultrasonic transducer.

Figure 6-21 and Figure 6-22 show the average heating value error for each test gas as a function of carbon dioxide concentration. The average errors were calculated over 15-minute test runs at the specified test pressures and temperatures. These illustrations show the derived heating values based upon the measured speed of sound readings and the carbon dioxide sensor readings compensated for nonlinear temperature effects. The average heating value errors are within the algorithm uncertainty limits of ±2 Btu/scf for all test gases at operating pressures of 75 and 100 psia. This error bound was also maintained for tests at the low and high temperatures of 40 and 120°F. At the lowest test pressure of 50 psia, the error fell slightly outside of the uncertainty limits, most probably because of the larger bias errors in the speed of sound at the low operating pressure. Additionally, since the 50 psia test pressure produced the lowest gas flow rate through the module, bias shifts in the CO_2 sensor readings also probably contributed to the errors in heating value at this pressure.

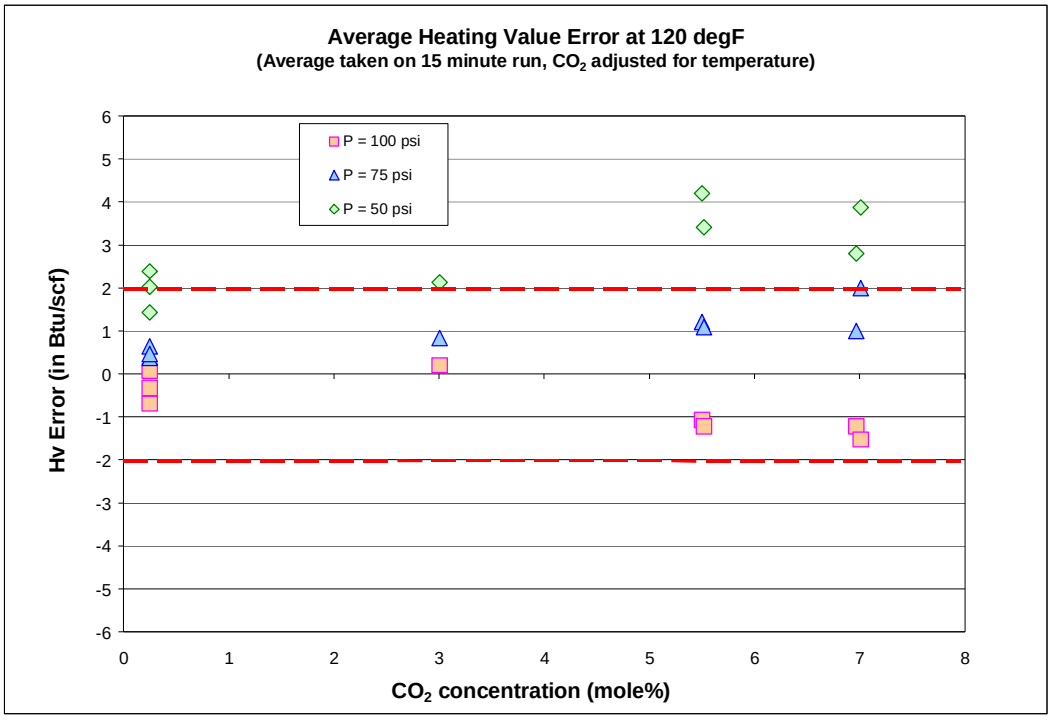

Figure 6-21. Average errors in heating value for module operating temperature of 120°F.

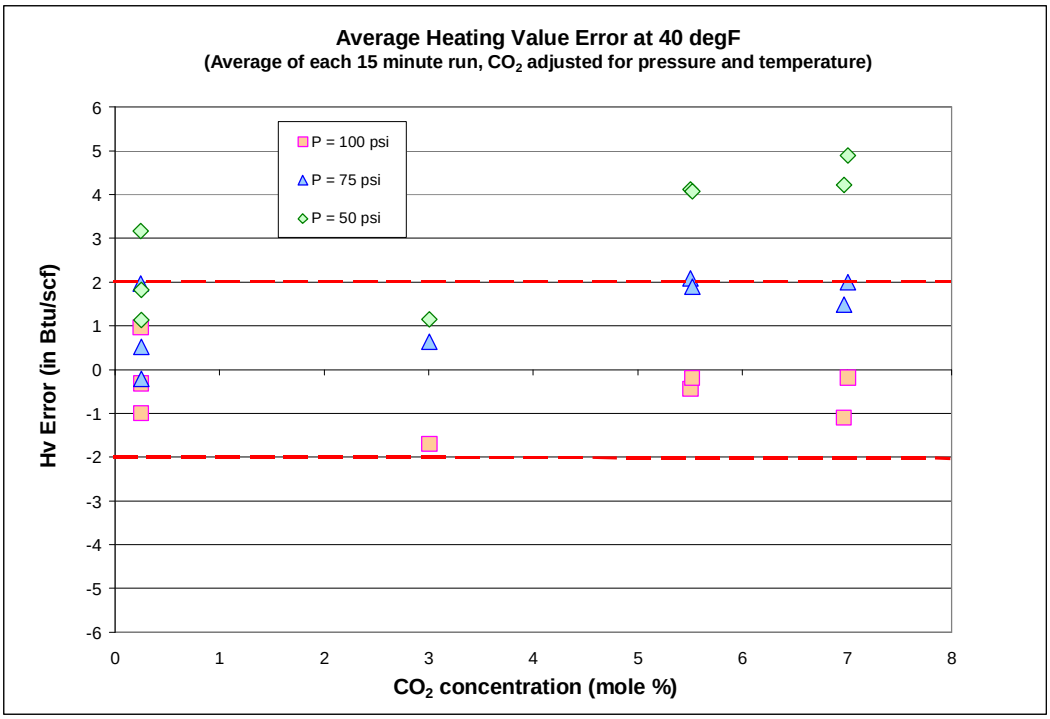

Figure 6-22. Average errors in heating value for module operating temperature of 40°F.

Within the scope of these laboratory tests, the energy meter module demonstrated accurate performance in determining the heating value for all eight test gases. The effects of high diluent concentrations did not cause significant errors in the heating value determination. In this respect, the heating value errors were all within the uncertainty limits of the algorithm. An examination of successive 1-minute determinations of heating value also provided insight into the effects of fluctuations in the measured speed of sound and carbon dioxide on the derived heating value errors over time. The measured speed of sound values were less steady at high temperatures, which contributed to an increase in the heating value error. Likewise, fluctuations in the measured carbon dioxide values increased with increasing carbon dioxide concentration, causing wider variations in the heating value errors for the test gases having higher amounts of carbon dioxide. Nevertheless, these fluctuations in sensor outputs did not cause the heating value errors to fluctuate significantly beyond the uncertainty requirements of the algorithm.

The overall results of the laboratory tests are summarized in Figure 6-23, which shows the sensor and heating value errors as low, medium, and high error zones in test matrix formats. These error zones are illustrated for gas temperature effects (diagrams with light shadings) and for gas pressure effects (diagrams with darker shadings) versus the CO_2 content in the test gases. The trends indicated in these diagrams show that the highest shifts in gas heating value error occur in the high CO_2 gases at the test temperature of 120°F. Acceptable performance of the energy meter module was obtained in all cases for gases having diluent concentrations of 3 mol% carbon dioxide plus 3 mol% or less nitrogen under all of the laboratory test conditions.

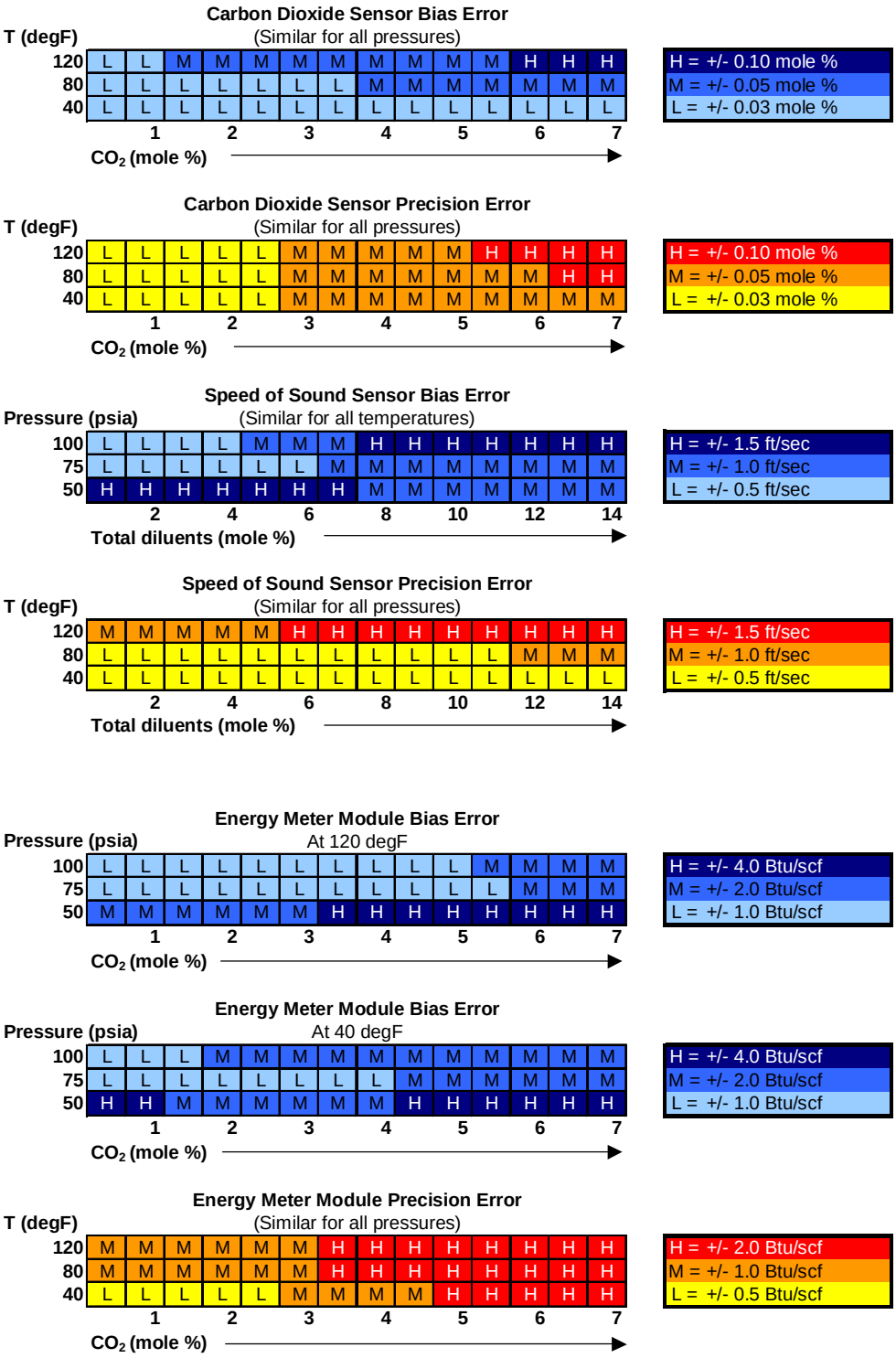

Figure 6-23. Test matrix error patterns for energy meter module operation with eight test gases having CO_2 concentrations of 0.25 mol% to 7 mol% at temperatures of 40, 80, and 120°F and gas supply pressures of 50, 75, and 100 psia.

These laboratory tests demonstrated that the prototype energy meter module can operate with acceptable performance under typical environmental operating conditions anticipated in many field installations. For operating temperatures in the range of 40 to 120°F, operating pressures of 75 and 100 psia, and gas diluent levels ranging from 0.50 to 14.0 mol%, the speed of sound and CO_2 sensor accuracies remained within acceptable limits, and the corresponding heating value errors were within the worst-case uncertainty limit of the inferential energy algorithm. Additionally, the laboratory tests provided test data useful for specifying improvements to the speed of sound ultrasonic transducer, and for guiding further development of an improved method to compensate for the nonlinearities and bias shift errors inherent in the carbon dioxide sensor.

6.2 NEW BRAUNFELS, TEXAS FIELD TEST

The energy meter retrofit module was field tested at a custody transfer meter station in New Braunfels, Texas, about 30 miles northeast of San Antonio. The module was installed at the site on February 28, 2003. The test ran from March 1-24, 2003. The test at the South Texas site marked the first field test of the assembled module using pipeline gas. The module components were exposed to ambient conditions for the duration of the test. The external temperature at the field site varied from approximately 60 to 90ºF during the test period.

The field site is a custody transfer station consisting of two 16-inch meter runs incorporating an orifice meter and an ultrasonic meter on each run. The station averages 300 MMscf of flow per day. The heating value of the natural gas at the field site averages between 1020 and 1040 Btu/scf, with a carbon dioxide content of approximately 1.25-1.30 mol% and nitrogen content of approximately 1.00-1.05 mol%. The average pipeline pressure is 550 psia, and gas temperature fluctuates between 50 and 70°F.

The energy meter module included the following components during the field tests: the 2002 speed of sound sensor, the Vaisala carbon dioxide sensor, a Rosemount pressure transmitter, a Rosemount temperature transmitter, and a gas-sample release flow rate monitor. The pressure in both the speed of sound sensing chamber and the carbon dioxide sensing chamber was held constant at 75 psia. Nonlinear calibration corrections were applied to the raw CO_2 sensor readings for proper operation at 75 psia. The correction developed by SwRI was applied to the raw CO_2 sensor readings in order to compensate for the high-pressure gas in the sensor. Pressure and temperature measurements were taken in the speed of sound sensing chamber. The installation of the energy meter module at the New Braunfels field site is shown in Figure 6-24 and Figure 6-25.

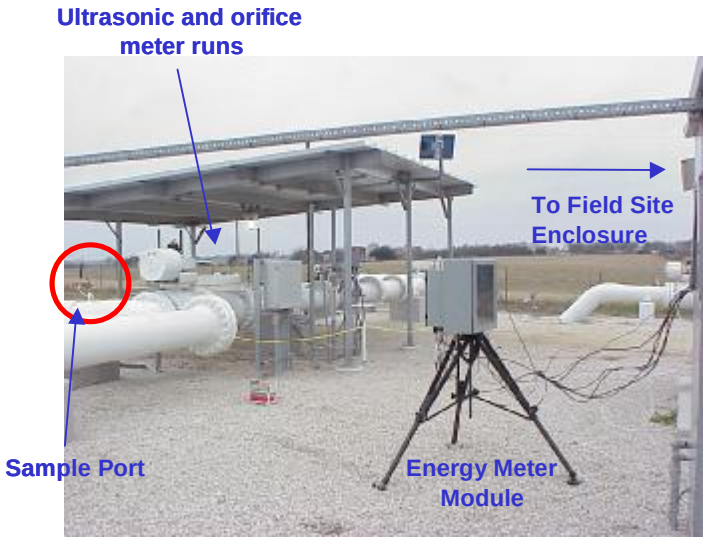

Figure 6-24. Energy meter module installation at the New Braunfels, Texas field site.

Figure 6-25. Front view of the energy meter module installed at the New Braunfels, Texas field site.

The 2002 speed of sound sensor utilized an Etalon 266 kHz ultrasonic transducer and the associated SwRI prototype electronics circuit board designed to excite the transducer and process the received reflections to yield the derived speed of sound in the test gas. As described in Chapter 3, the circuit board generates a repetitive ultrasonic pulse waveform and receives a waveform containing pulse reflections from two separated targets within the test chamber. The received signal is digitized and a cross-correlation algorithm is applied to derive the time difference between the two reflections from which the speed of sound in the gas is computed. In

the 2002 module design, the circuit board delivered the resulting speed of sound measurement, via serial MODBUS, to a Bristol Babcock flow computer for further data analysis.

The sample gas delivered to the module was taken from a pipeline sample port located upstream of an ultrasonic flow meter, as indicated in Figure 6-24. A regulator was used to reduce the line pressure to the module operating pressure of 75 psia. The module measurements for pressure, temperature, raw carbon dioxide concentration, and speed of sound were input to a Bristol Babcock flow computer located in the field site enclosure. The Bristol Babcock flow computer was programmed to apply the CO_2 calibration correction for sensor operation at 75 psia, and then apply the energy meter inferential algorithm to compute the test gas standard volumetric heating value, standard density, and molecular weight. These results were fed to an Integrated Information Technologies (IIT) RGC Data Logger for separate data accumulation and storage on 3-1/2 in. magnetic diskette.

The equipment located in the field site enclosure is shown in Figure 6-26. A Danalyzer Gas Chromatograph, capable of analyzing natural gas components to hexanes-plus resolution (i.e., heavier components are grouped with hexane in the analysis), was used in the field test. This on-site gas chromatograph was used to provide independent information on the pipeline gas mixture concentration from which the reference heating value of the gas was derived. The Bristol Babcock flow computer that applied the energy meter algorithm is also shown in Figure 6-26. Not shown in this figure is the RGC Data Logger used to store the gas chromatograph readings, the various energy meter measurements, and the Bristol Babcock output data. The RGC Data Logger sampled values from the energy meter module (via the Bristol Babcock) and from the gas chromatograph once every five minutes.

Figure 6-26. Field site enclosure for the on-site gas chromatograph (left) and the energy meter Bristol Babcock flow computer (right).

The field test results were used to evaluate the performance of the energy meter module CO_2 sensor and the speed of sound sensor by comparison with reference values derived from the gas

chromatograph and calculations using the AGA-8 equation of state, respectively. The short-term stability and accuracy of the energy meter module was also evaluated.

During the three-week test period the prototype energy meter retrofit module performed well. The module sensing components and their associated electronics and signal processing elements were not affected by the extended continuous outdoor run time at the site and, as will be seen below, were only slightly affected by diurnal changes in ambient temperature. The carbon dioxide sensor and the speed of sound sensor demonstrated reliable operation throughout the field test. However, an abnormal power surge at the field site affected the DC power supply in the Bristol Babcock flow computer. This power surge also affected the communications link between the speed of sound sensor electronics board and the flow computer. The loss in communications resulted in the flow computer not receiving updated speed of sound readings from the flow meter. Since the module was unattended during field tests, the period of recorded test data was interrupted on two occasions, resulting in less than the maximum data potentially available during the three-week test period.

The results for the carbon dioxide sensor measurements are shown in Figure 6-27 and Figure 6-28. The average difference between the energy meter carbon dioxide concentration and the gas chromatograph carbon dioxide value was ±0.03 mol%. Over the entire 120-hour test period of recorded data, the variation in the carbon dioxide sensor measurements relative to the gas chromatograph reference value remained within ±0.10 mol%, including transient extremes. Figure 6-28 highlights the influence of the module operating temperature on the carbon dioxide sensor error. Since the internal temperature of the energy meter module tracked the diurnal ambient temperature (from 50 to 100ºF), the carbon dioxide sensor error exhibited a similar trend. Figure 6-28 demonstrates that the carbon dioxide sensor output is slightly dependent on ambient temperature, possibly because of temperature differences within the module (recall that temperature is only measured in the sound speed sensor). This temperature influence on the sensor is responsible for the majority of the fluctuations in the CO_2 sensor measurements.

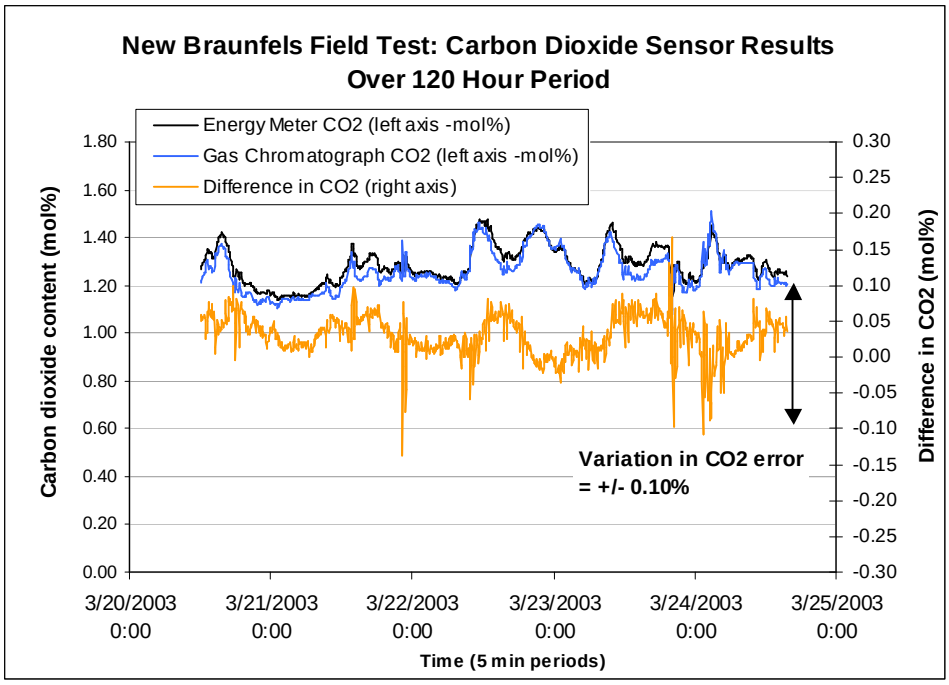

Figure 6-27. Carbon dioxide sensor results for a 120-hour field test period.

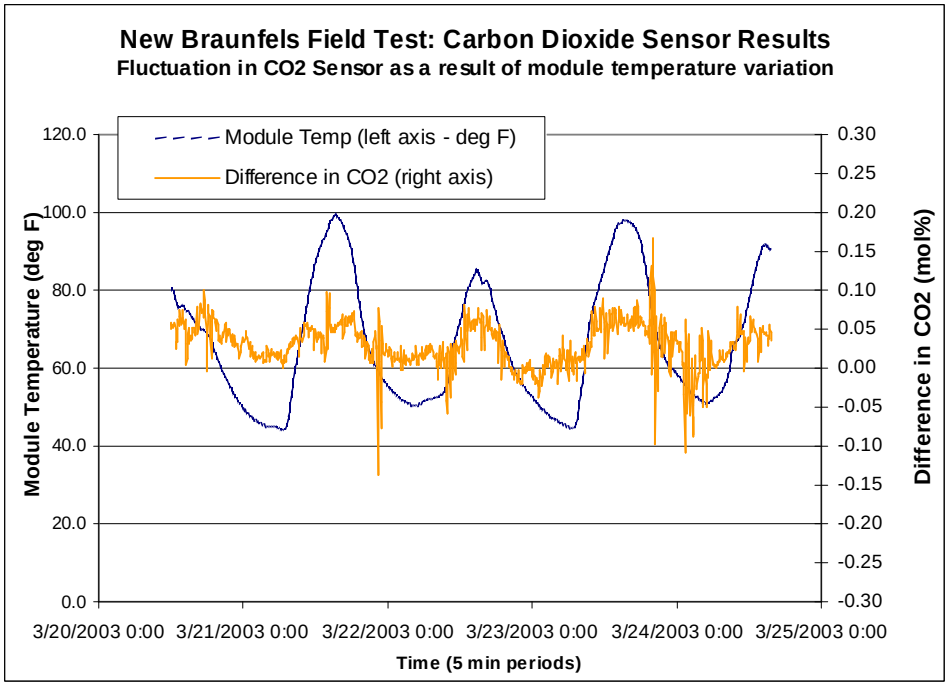

Figure 6-28. Variations in energy meter module operating temperature compared with differences in carbon dioxide readings between the energy meter and gas chromatograph.

The speed of sound sensor performance is shown in Figure 6-29. Continuous reference values for the speed of sound are not available, since the gas chromatograph readings were only updated at five-minute intervals. The AGA-8 equation of state was used to compute the speed of sound at several chromatograph gas concentration readings during the first seven hours of the test period, as a check on the speed of sound sensor measurements. This comparison is shown in Figure 6-29, and the details of the comparison are listed in Table 6-3. The average difference between the energy meter standard speed of sound measurements and the AGA-8 calculated values is -4.21 ft/s (the energy meter produced lower values than AGA-8). This offset appeared to increase as the module ambient operating temperature decreased during the seven-hour test period. The source of this offset and its temperature drift is not conclusively known, but could be one or more of the following: (1) the absolute calibration of the energy meter module (performed using a certified calibration gas mixture several days in advance of the field setup); (2) temperature influences on the ultrasonic sound speed sensor components; and (3) temperature effects on the gas chromatograph readings, which exhibited a partial failure during tests.

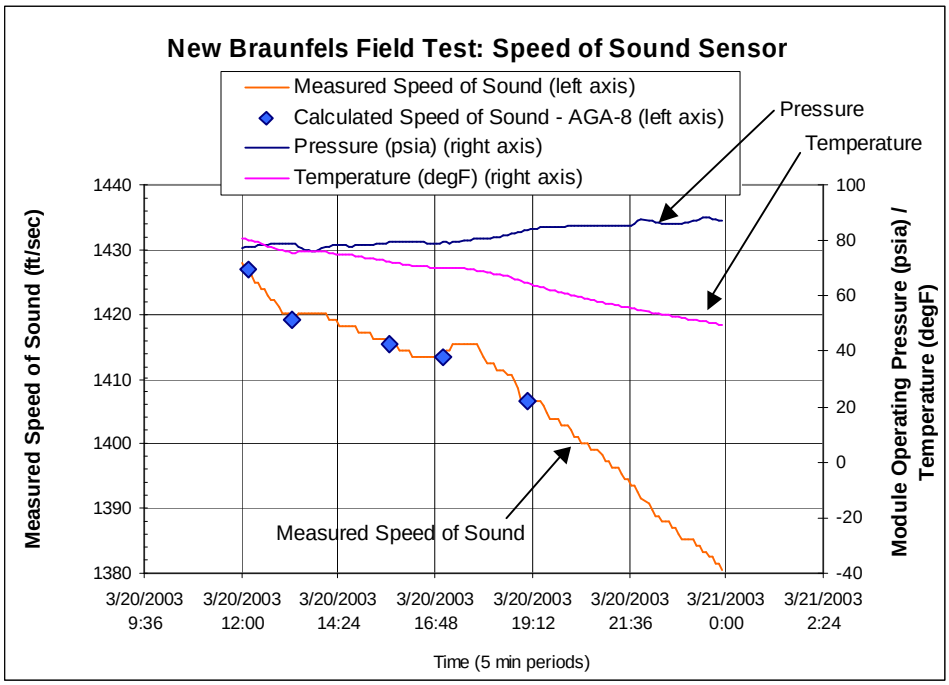

Figure 6-29. Speed of sound sensor results for a 17-hour field test period with calculated sound speed sample points for comparison only during first 7 hours, because of partial failure of GC.

Table 6-3. Measured speed of sound in the energy meter module compared with speed of sound values calculated using AGA-8 and data from the reference gas chromatograph.

Energy Meter Module Measurements				AGA-8 Values based on Reference GC		Comparison of Differences	
PX.T	TX.T	SOS (ft/s)	StdSOS (ft/s)	AGA8 SOS (ft/s)	AGA8 StdSOS (ft/s)	Diff SOS (ft/s)	Diff STSOS (ft/s)
77.699	80.180	1426.9400	1406.9120	1429.2911	1409.2702	-2.35	-2.36
78.786	75.594	1419.1640	1404.9400	1423.0107	1408.8333	-3.85	-3.89
79.270	72.335	1415.3080	1405.2010	1418.8954	1408.8453	-3.59	-3.64
79.229	70.042	1413.3870	1406.3320	1418.8030	1411.6052	-5.42	-5.27
83.700	64.732	1406.7070	1406.7920	1412.5435	1412.5042	-5.84	-5.71

Problems with ancillary equipment and the reference gas chromatograph at the test site caused a disruption in the tests after March 21, 2004. During the March 21-25 test period, the amount of ethane detected by the reference gas chromatograph dropped to zero, indicating a malfunction in the gas chromatograph. The error in the detection of ethane caused the heating value calculated by the gas chromatograph analysis to drop from an average of 1,012 Btu/scf to an average of 1,005 Btu/scf. The measured heating values from the energy meter and the one-site gas chromatograph are shown in Figure 6-30. For the remainder of the test period, the inferred heating value from the energy meter could not be compared to the reference, since the reference gas chromatograph had become inaccurate without the ethane measurement. The gas chromatograph failure suggests energy meter verification of the gas chromatograph heating value determination would be beneficial.

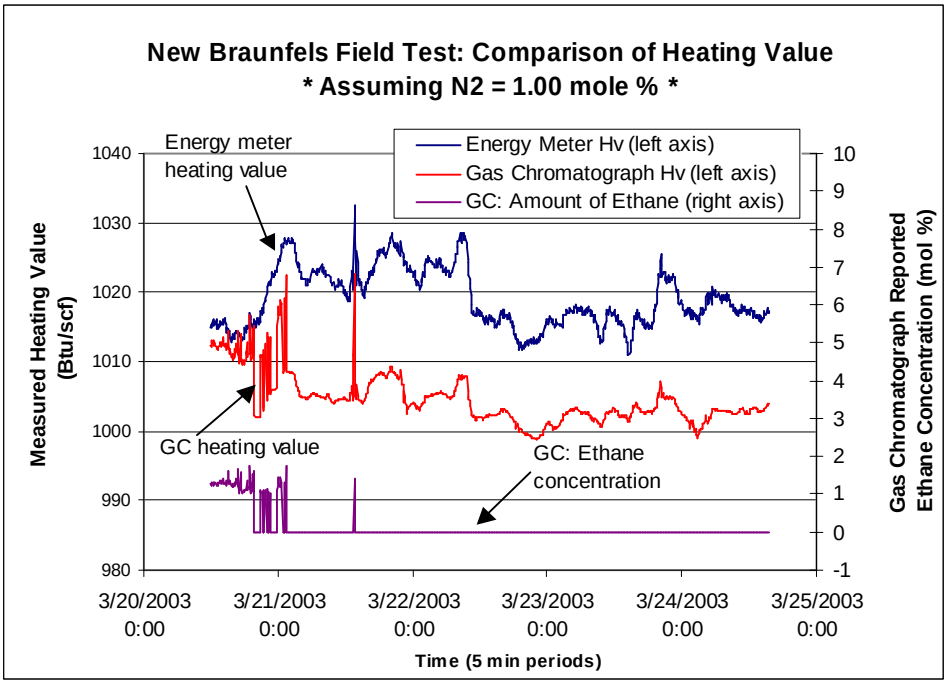

Figure 6-30. Comparison of heating values determined by gas chromatograph analysis and the energy meter module.

Figure 6-31 shows the difference in the energy meter and gas chromatograph heating values for the first eight hours of the test period, when the gas chromatograph was still providing fairly reliable data. The majority of the data shows a difference in the heating values between 2 and 4 Btu/scf. This suggests a nominal +2 Btu/scf offset, with a precision error of ± 1 Btu/scf. The offset and some of the precision error in heating value is probably due to the error in the constant nitrogen assumption. In the inferential energy meter analysis, a nitrogen concentration of 1.00 mol% was assumed, while the nitrogen level in the gas as measured by the gas chromatograph fluctuated between 1.00 and 1.20 mol%. The larger deviations in heating value correspond to abnormal changes in the ethane concentration, indicating that they are due at least in part to the error in the gas chromatograph analysis of ethane concentration.

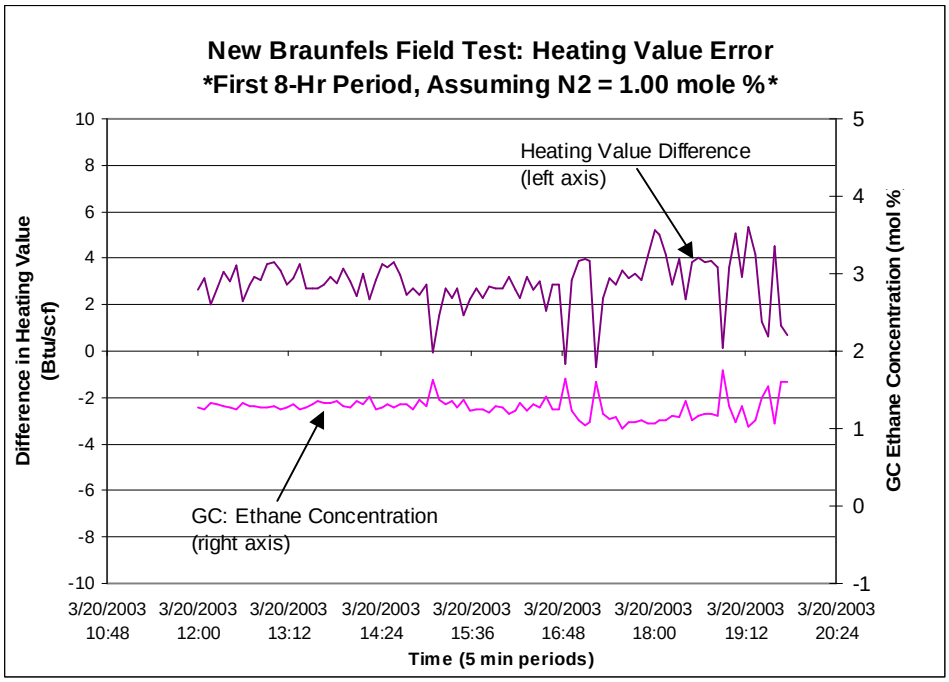

Figure 6-31. Difference in heating value measurements during 24-hour period, prior to GC failure.

Overall, despite the lack of reliable reference data as a result of the on-site gas chromatograph failure during part of the test period, the energy meter module tracked the heating value provided by the gas chromatograph analysis very well, with a difference of ±1 Btu/scf observed during the first eight hours of testing. Differences during this period can be attributed in part to the ambient temperature effects on the ultrasonic sound speed sensor described above. Additional tests are needed to fully characterize the accuracy and stability of the module instrumentation over a longer period of time and under experimental conditions in which the temperature influences on the module performance can be evaluated in greater detail.

6.3 FIELD TESTS OF THE ENERGY METER ALGORITHM AS A STAND-ALONE APPLICATION

In June 2003, members of the natural gas industry suggested another useful implementation of the energy meter technology to determine properties of the natural gas stream. In the proposed application, the algorithm would still reside on a flow computer, but the instrument module would not be used. Instead, the algorithm would receive values of sound speed, temperature, pressure, CO_2 content and N_2 content from station instruments. This implementation would be useful in verifying the performance of an onsite gas chromatograph, or as an additional gas quality monitor. The GTI/PRCI Energy Meter Subcommittee requested tests of the stand-alone application in 2003 to allow the industry to become more familiar with the algorithm capabilities, possible applications, and performance.

6.3.1 Data logger Programming and Lab Testing

For the stand-alone algorithm field tests, the single-state algorithm was installed on an Integrated Information Technologies (IIT) RGC Controller, a combination data logger and flow computer. At the test site, the RGC Controller would receive inputs to the algorithm from an ultrasonic flow meter, temperature and pressure transmitters, and an on-site gas chromatograph. Gas properties calculated by the algorithm, such as standard volumetric heating values and gas density, would be compared to the GC results.

Two RGC Controller units were purchased for the algorithm-only tests. Each of these units included two serial ports for input from meter station instrumentation operating under the MODBUS protocol, eight analog input ports for other instrumentation, and two analog output ports. Upon construction of the first RGC Controller unit, the single-state algorithm was integrated into the RGC Controller firmware to accept input from meter station instruments and to compute the heating value of the gas stream at the meter. The algorithm was implemented on the RGC during tests using both live diluent values from a GC and constant diluent values obtained from periodic GC compositional analyses. The latter could be used for gas quality monitoring in locations where a GC is not available. Pre-testing of the RGC Controllers at the SwRI MRF and deployment of the system to the first field test was accomplished in April 2004.

6.3.2 Selection of Field Test Sites

Information on the flowing gas conditions and instrumentation at various meter stations was obtained from industry representatives in order to select two applicable test sites. Tests of the algorithm required a field site with an ultrasonic flow meter for determining the speed of sound and an on-line gas chromatograph for determining the gas diluents. The final test locations were field sites nominated by El Paso Energy and Southern California Gas (SoCal). Tests were scheduled at the El Paso site first to allow extra time for preparations by SoCal. Preparations were coordinated with El Paso and IIT personnel to program the RGC Controller to properly interface with the site equipment.

The El Paso site, located downstream of a compressor station near Agua Dulce, Texas, was selected in part because it was not used for custody transfer, and the tests would therefore not interfere with custody transfer activities. The site carried transmission gas with a relatively stable composition of 94 to 98 mol% methane, 1.5 to 4 mol% ethane, 0.2 to 0.3 mol% nitrogen, and heating values from 1,020 to 1,050 Btu/scf. Only the CO_2 content of the gas showed significant historical variations between 0.2 and 1.4 mol%. Pressures at the test site historically fluctuated between 650 and 850 psia, and temperatures ranged from 68 to 78°F. Figure 6-32 shows the site layout, consisting of several Daniel ultrasonic flow meters, a Daniel gas chromatograph (GC), Rosemount pressure and temperature transmitters, and a Bristol Babcock flow computer to gather data and compute heating values and energy flow rates.

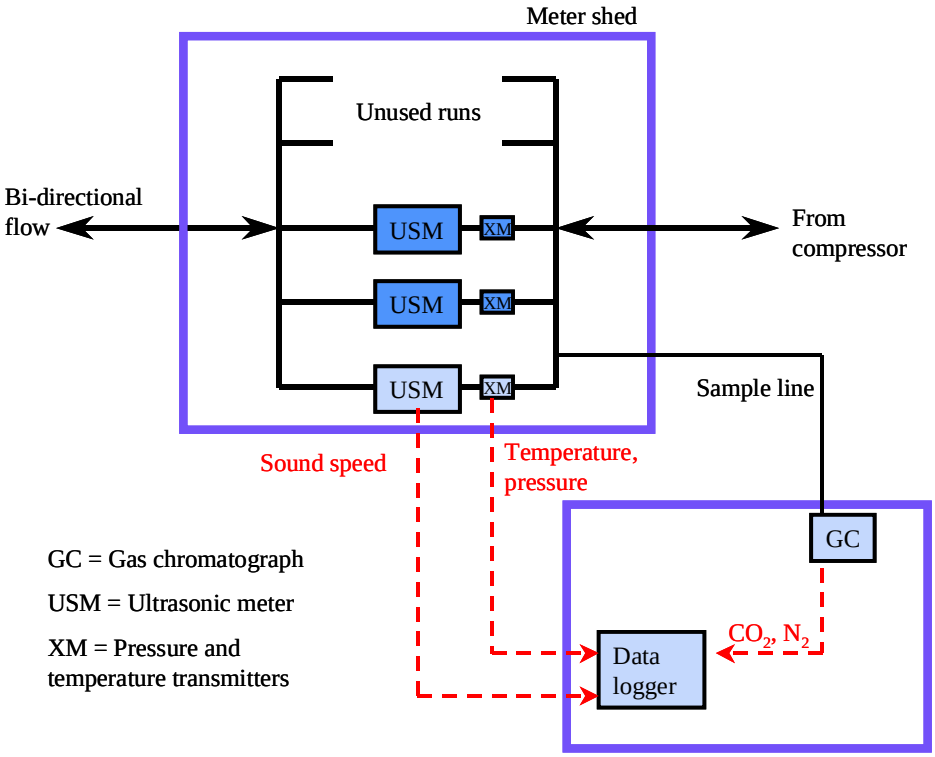

Figure 6-32. Layout of the El Paso metering station and equipment. Dashed lines mark the flow of input data to the algorithm.

6.3.3 MRF Pre-Tests

Based on the specifications of the Agua Dulce instrumentation, the first RGC unit was programmed to accept input from the instrumentation at the site. The unit was then programmed to calculate heating values using both measured and assumed values of diluents as a means of testing three potential implementations of the algorithm: (1) live diluent input values; (2) a live input for CO_2 and an assumed value for nitrogen based on knowledge of the gas stream; and (3) assumed values for both diluents.

Pre-tests of the RGC Controller were performed at the SwRI Metering Research Facility prior to installation at the field site. Inputs from an ultrasonic flow meter and pressure and temperature transmitters in the High Pressure Loop (HPL), and input from the MRF gas chromatograph, were used to pre-test the RGC for proper operation and implementation of the algorithm. The controller successfully read data from the Daniel ultrasonic meter in the MRF HPL, and temperature and pressure data from analog inputs. Due to differences between the Daniel GC at the MRF and at the Agua Dulce site, however, the controller could not be tested using live diluent inputs. Instead, the algorithm was tested using live sound speed data and "dummy" diluent values. During the pre-tests, MRF personnel were also trained on the use of the RGC Controller and the related software, in order to assist in the field installation of the RGC unit and to collect data via modem from the El Paso site.

6.3.4 Tests at the Agua Dulce Field Site

Personnel from SwRI, IIT and El Paso installed the RGC unit at the Agua Dulce field site near Corpus Christi on April 13, 2004 (Figure 6-33). Constant values for CO_2 and N_2 of 0.8014% and 0.2205%, respectively, were entered into to the controller firmware for the two implementations of the algorithm requiring assumed diluent values. These values were the average diluent content of the gas stream observed during the day that the RGC was installed. After correcting a problem in communications with the on-site ultrasonic meter, tests indicated that the unit was functioning correctly, and the algorithm was left to run continuously.

Remote polling of the device after installation revealed a problem with a signal splitter used at the site to send two inputs to the RGC through a single serial port. A second problem was discovered with the algorithm implementation using a live CO_2 value and an assumed value of nitrogen. Additional work by IIT and El Paso field staff resolved both of these problems. However, the extra work and cost required to resolve these problems resulted in deferral of the tests at Southern California Gas, pending results of the tests at the El Paso site.

Figure 6-33. Installation of the RGC data logger at the El Paso field site. *Top*: RGC data logger (on the workbench) implementing the algorithm. *Bottom left*: Flow computer and data connections providing sound speed, temperature, and pressure data. *Bottom right*: Chromatograph providing diluent data.

Initial algorithm results for density and heating value, shown in Figure 6-34, disagreed significantly with results computed by the site GC. The specific gravity computed by the algorithm using live diluent values disagreed with values from the GC by as much as 2% and differences in heating value were typically 10 Btu/scf. Comparisons of the algorithm results with heating values calculated by the on-site equipment revealed three potential problems: (1) indications of intermittent GC failure; (2) unexplained fluctuations in sound speed measurements from the ultrasonic flow meter; and (3) evidence of time delays in GC data relative to data from other on-line instruments at the site.

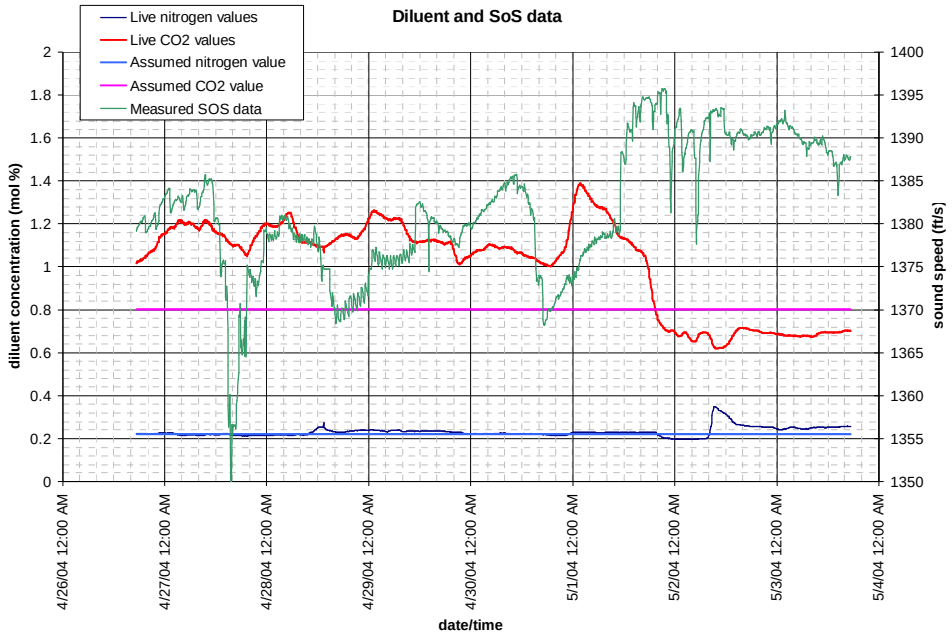

(a)

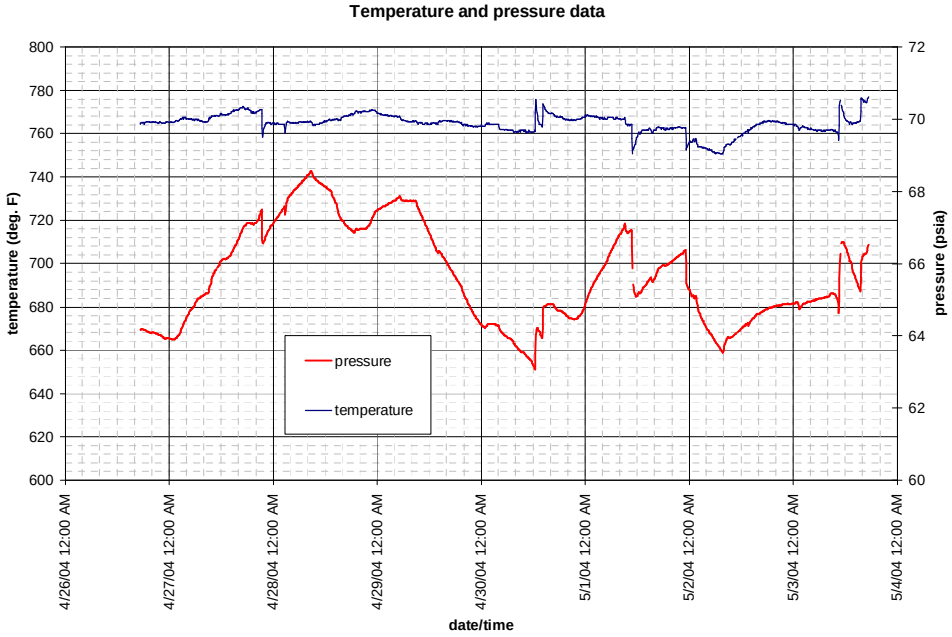

(b)

Figure 6-34. Initial data collected from the algorithm at the Agua Dulce site in late April and early May 2004. (a) Sound speed, measured diluent values, and assumed diluent values; (b) Measured pressure and temperature data.

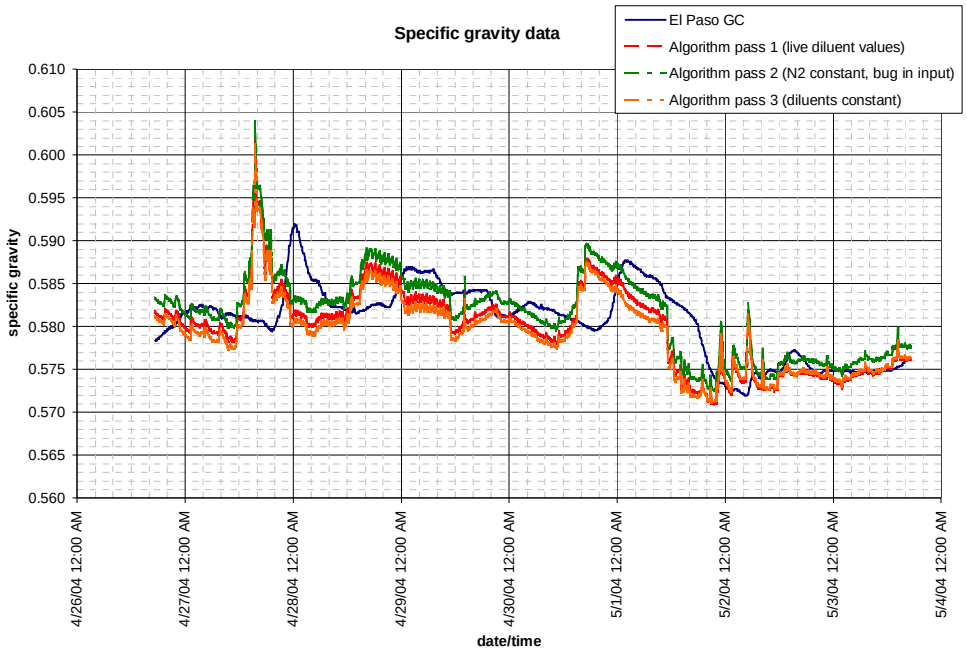

(c)

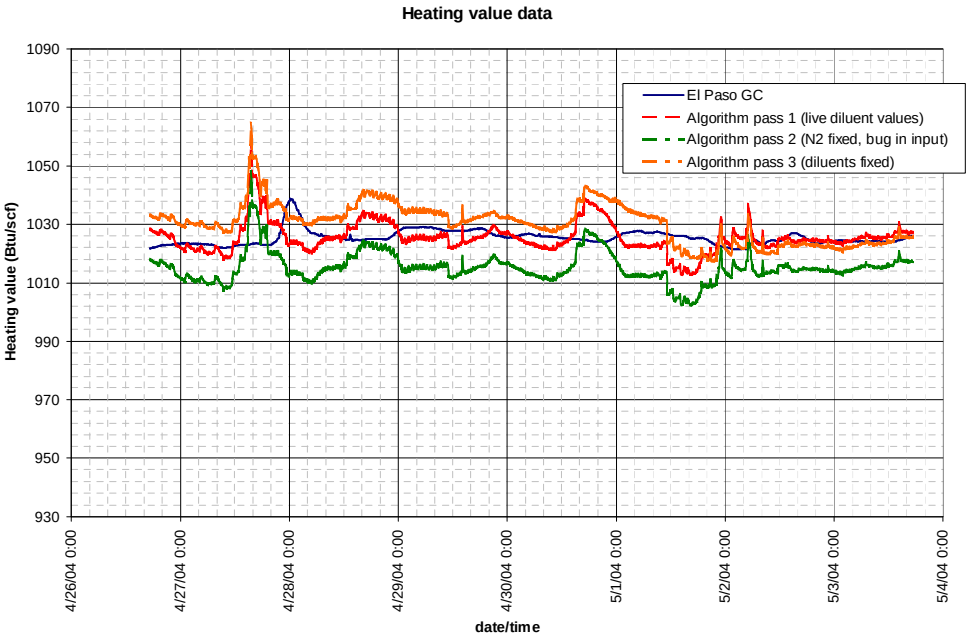

(d)

Figure 6-34 (continued). (c) Comparison of specific gravity values determined by the site GC and the three algorithm implementations; (d) Comparison of heating values determined by the site GC and the three algorithm implementations.

Figure 6-34(a) shows that the fixed nitrogen concentration assumed for the second and third algorithm implementations was very close to the actual values measured by the GC over the test

period, but that the CO_2 concentration deviated significantly from the assumed value over much of the period. Because of this, the second implementation using live CO_2 values and the assumed nitrogen value agrees very closely with the first version of the algorithm using live diluent values, while the third implementation using assumed values for both diluents deviates from the other two.

The intermittent "failures" of the GC were identified as programmed off-line calibration cycles, and were subsequently removed from the RGC analyses. In June, El Paso site personnel performed maintenance on the ultrasonic meter being used to measure sound speed, including cleaning of the transducer faces. This maintenance led to only slight improvements in the fluctuating sound speed measurements, however.

A review of the data identified fluctuations in the diluent concentrations similar to those seen in the sound speed, indicating that they reflected the actual behavior of the gas composition. However, the diluent fluctuations lagged those in the sound speed by as much as nine and one-half hours. The cause of this time lag was "line pack" between the GC gas sampling point and the GC itself. The existing sample line was made of 3/8"-diameter tubing, and included a shell-and-tube heat exchanger to warm the sample between the probe and the GC. Calculations indicated that a restricted flow rate through this apparatus could lead to a travel time of several hours from the sampling point through the heat exchanger to the GC. While temperature, pressure, and sound speed measurements would reflect the gas flowing through the meter at the time of measurement, the slow travel time of a gas sample to the GC meant that the gas composition reported by the gas chromatograph had actually passed the sampling point several hours earlier.

The heating values determined by the site GC and the three implementations of the algorithm are compared in Figure 6-35(a). Similar trends are observed among the four values, but a lag of several hours can be observed in the trends of the site GC values. This is most evident in the period of high heating values over the period of May 12 to 14. By moving the heating values computed by the GC backward in time by 9 hours 36 minutes, the general trends were brought into much better agreement. To confirm this line pack delay, sound speed values were computed from the complete gas compositions recorded by the site GC, using the AGA-8 equation of state (American Gas Association [1994]). As shown in Figure 6-35(b) and (c), the sound speed data computed from the properly timed gas compositions followed trends similar to the measured sound speed values, except for fluctuations in the measurements observed on May 12 and 13.

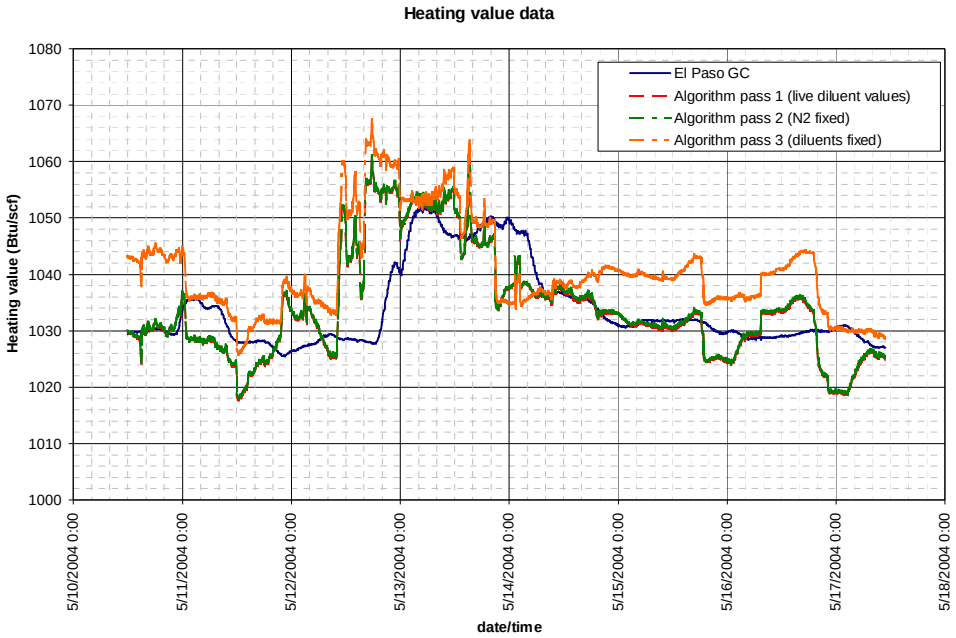

(a)

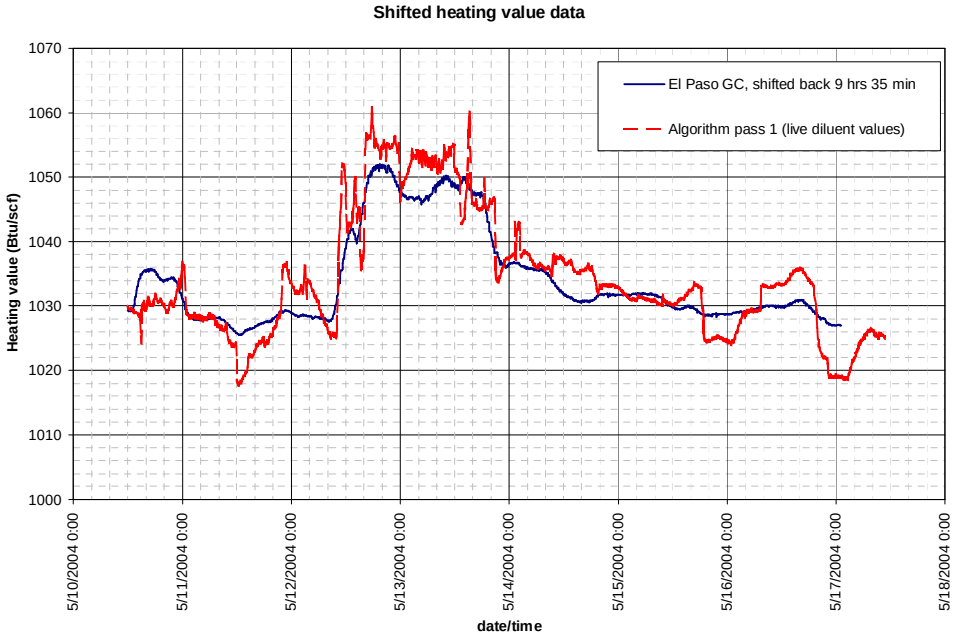

(b)

Figure 6-35. Evidence of "line pack" in the line connecting the sampling probe to the onsite GC. (a) Comparison of heating values determined by the site GC and the three algorithm implementations; (b) Comparison of heating values from the algorithm to heating values computed from the GC compositions and shifted back 9 hours, 36 minutes.

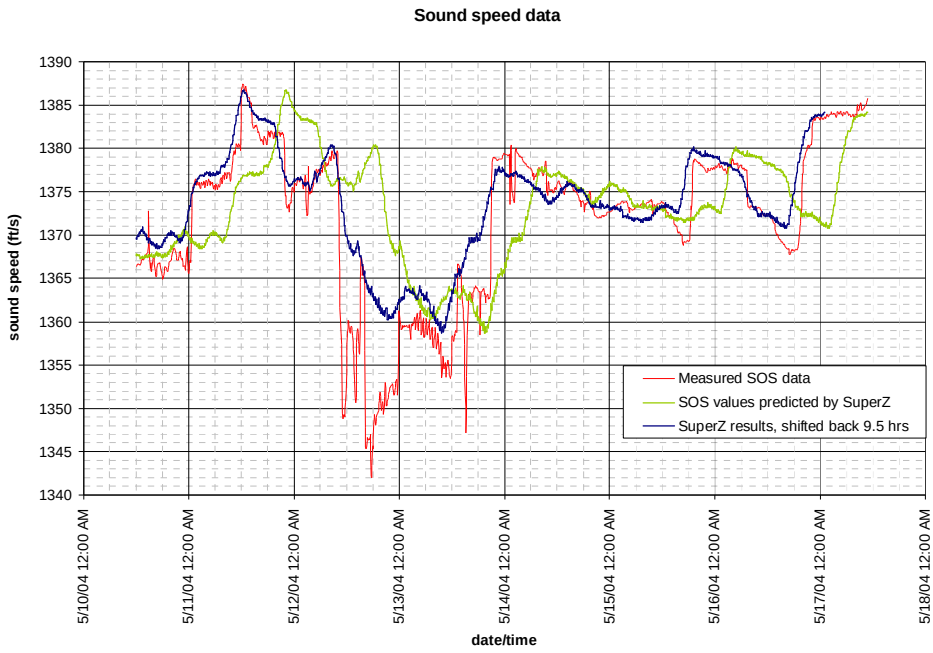

(c)

Figure 6-35 (continued). (c) Comparison of measured sound speed values to sound speed values computed from the GC compositions and shifted back 9 hours, 36 minutes.

A pressure regulated sampling probe and 1/8-in. diameter sampling line were installed at the site to bypass the existing GC sampling line. A review of the data from the RGC data logger and the GC after the GC began taking samples from the bypass line confirmed that the bypass had eliminated the GC delay. As shown in Figure 6-36, after the bypass was installed, increases in sound speed were recorded at the same time as corresponding decreases in the CO_2 content. After installation of the bypass line, data from the algorithm and the on-site GC were collected for a week and used to quantitatively compare the heating values obtained by the algorithm and the GC calculations. Figure 6-37 shows that for the one-week period, the average disagreement between heating values from the live-diluent version of the algorithm and the GC was –0.7 Btu/scf, and the standard deviation in differences was 3.6 Btu/scf. The implementation of the algorithm using live carbon dioxide values and a constant nitrogen value was in close agreement with the live-diluent version and also compared closely with the GC results. Figure 6-37 shows the larger errors caused by the assumed value of carbon dioxide in the third version of the algorithm; significant CO_2 fluctuations were observed during the week of testing, which caused the disagreement.

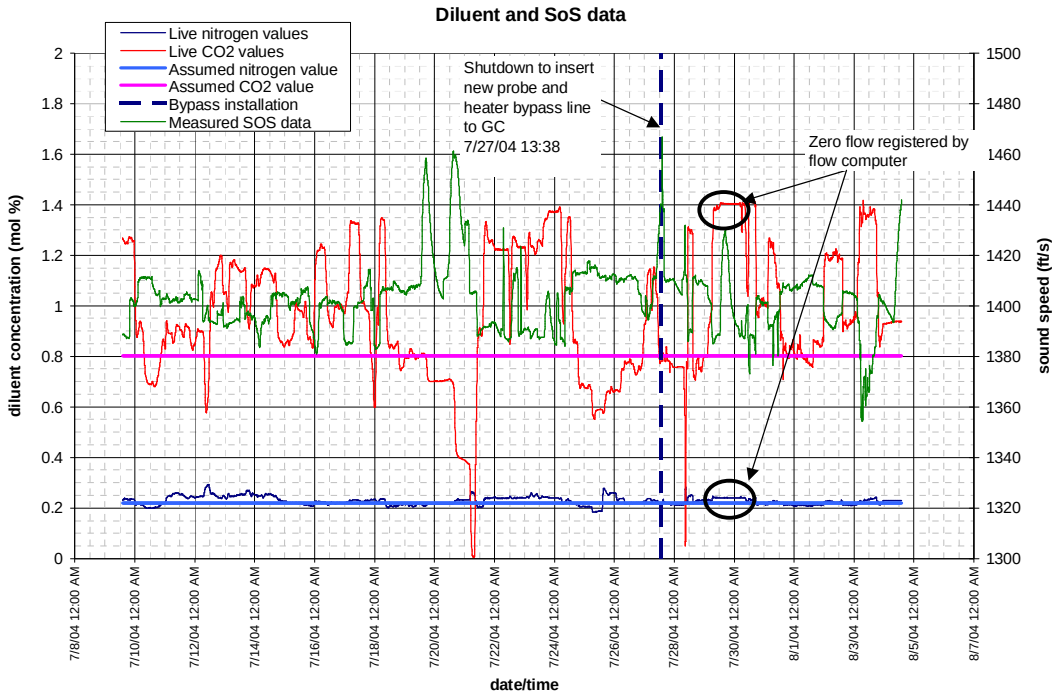

Figure 6-36. Comparison of measured sound speeds and diluent concentrations before and after installation of the bypass sample line.

After the site equipment problems were resolved, tests were continued for several months to ensure that a long period of useful performance data could be collected and the accuracy of the algorithm in its various implementations could be verified. Data collected over the month of August continued to show good agreement between heating values from the algorithm and from the GC. Several periods were recorded during the month in which the ultrasonic meter providing data to the data logger was "shut in," that is, when no flow occurred and the gas was stagnant in the meter run. During these shut-in periods, diurnal changes in pressure, temperature, and sound speed in the stagnant gas were recorded. Figure 6-38 shows a large period of such cyclic variations during the period from August 12 to 18. The errors in heating value during these no-flow periods suggest that thermal gradients in the gas led to erroneous sound speed measurements which, in turn, caused errors in the heating values computed by the algorithm as shown in Figure 6-39. In this case, during the entire period from August 4 to 24, the average error of the algorithm using live diluent values was -1.92 Btu/scf with a standard deviation of 4.9 Btu/scf, whereas during periods of flow at the meter, the average error was within 0.2 Btu/scf with a standard deviation of less than 2.5 Btu/scf.

Overall, the results of field tests of the algorithm indicate its success at inferring the properties of natural gas from these measurements, and support its use as a stand-alone diagnostic tool for metering station instruments as well as part of the inferential energy meter.

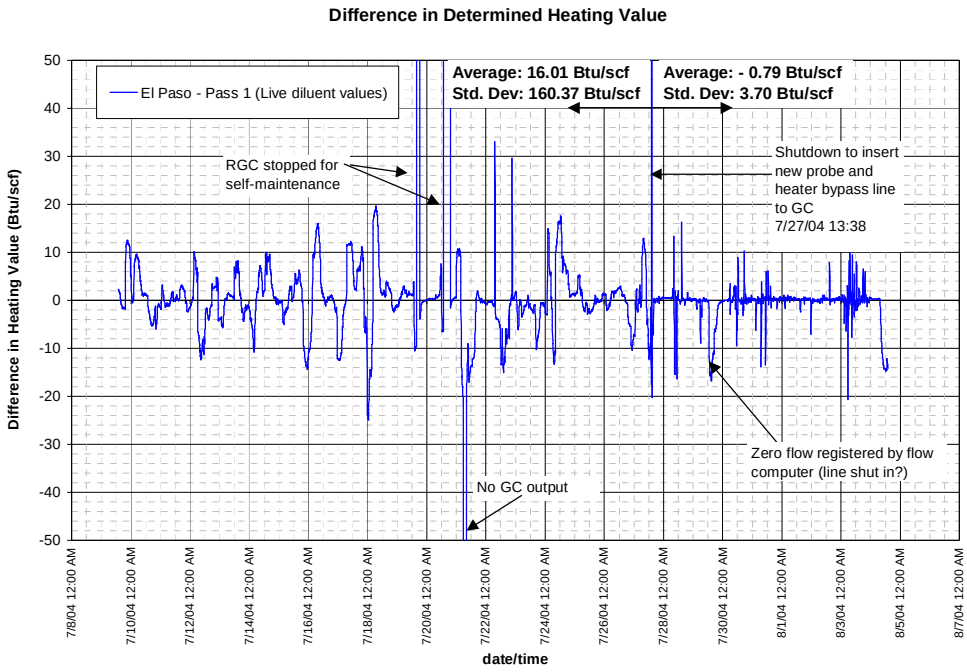

(a)

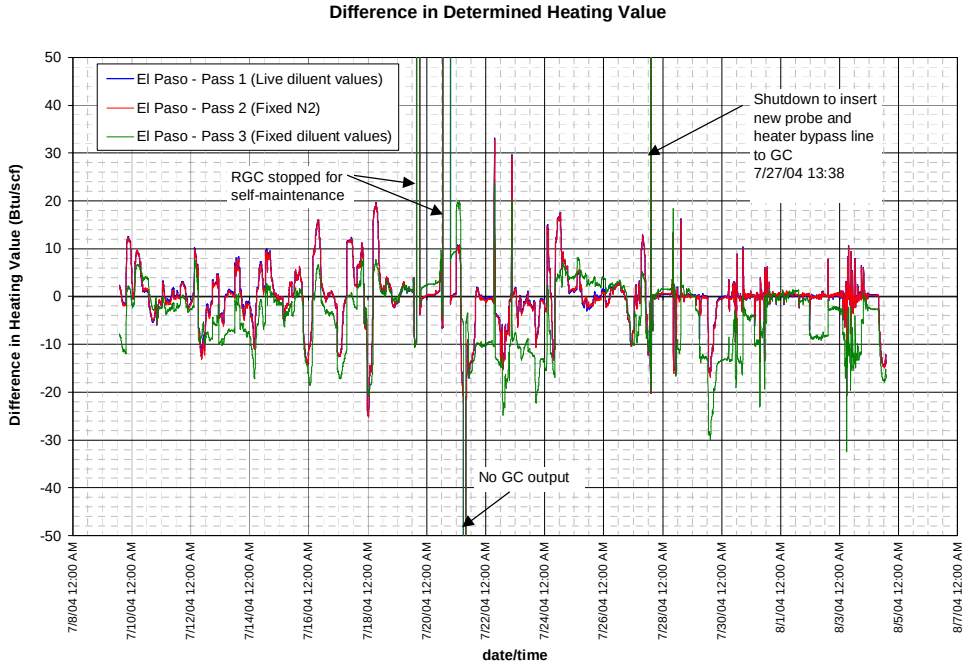

(b)

Figure 6-37. Comparison of computed heating values before and after installation of the bypass sample line. (a) Results of the algorithm using only live N_2 and CO_2 values; (b) Results of all three versions of the algorithm.

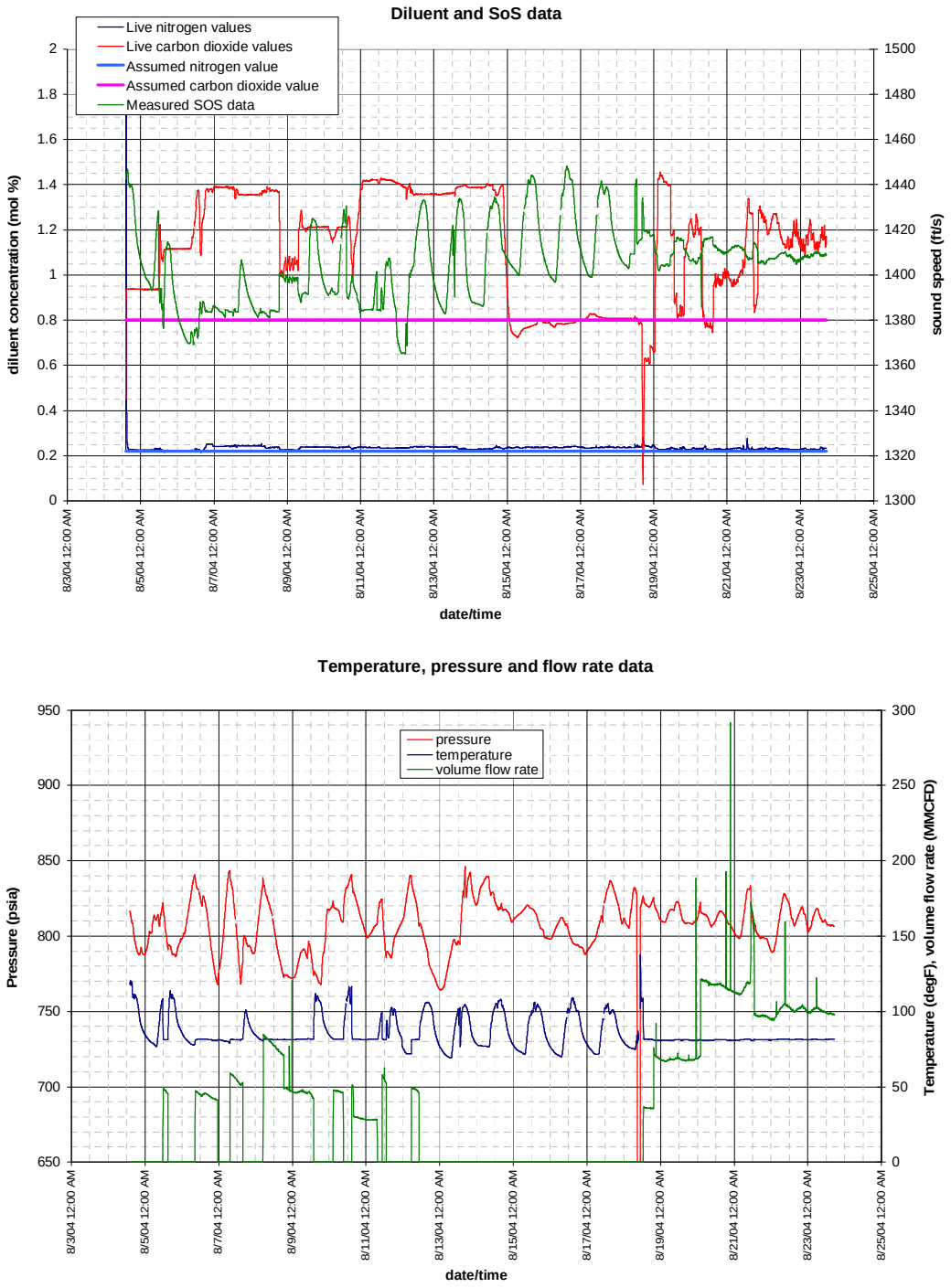

Figure 6-38. Algorithm inputs during August tests, showing diurnal variations in temperature, pressure, and measured sound speed during periods of zero flow.

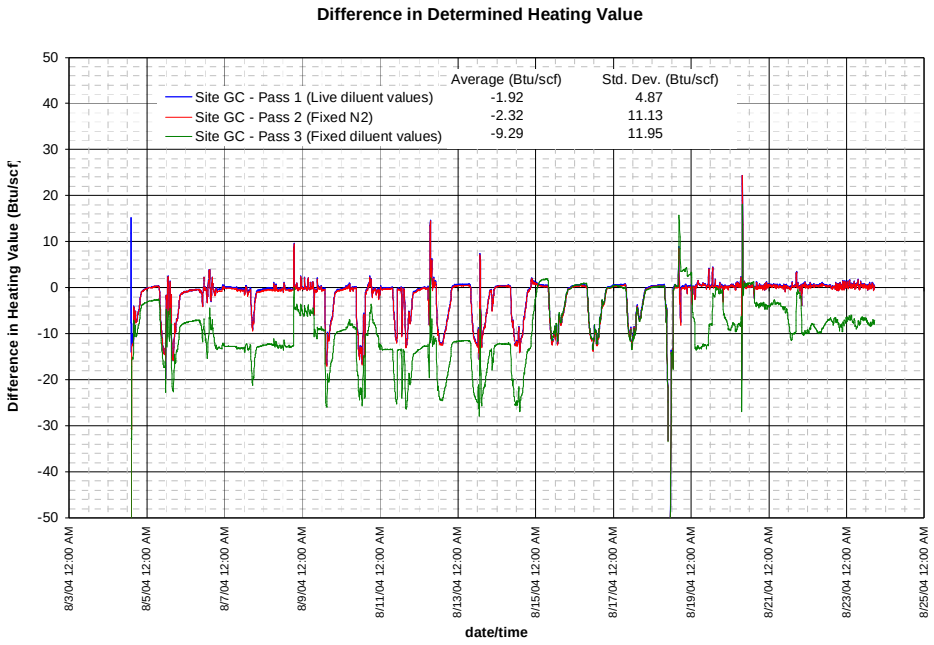

(a)

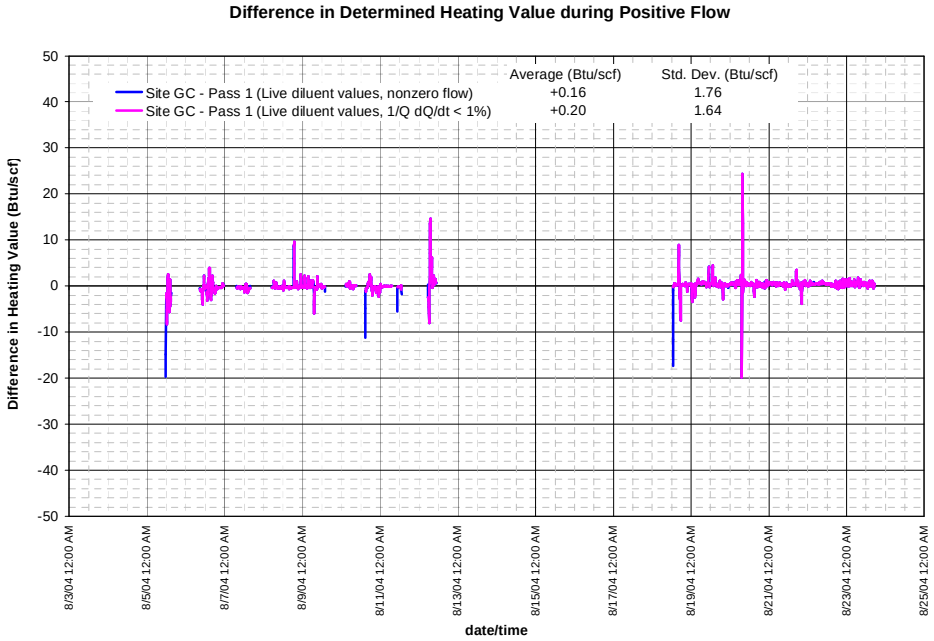

(b)

Figure 6-39. Differences between heating values computed by the various algorithm versions and the onsite GC. (a) Differences in heating value at all times during the test period; (b) Differences in heating value from the algorithm using live diluent values and sound speed values during periods of steady flow.

6.4 LABORATORY TESTS OF THE 2003 PROTOTYPE ENERGY METER MODULE

6.4.1 Laboratory Test Plan and Procedures

Laboratory bench tests were performed to evaluate the sensors and functional performance of the 2003 prototype Energy Meter module designed for two-state operation and described in Chapter 5. These tests were performed using four certified natural gas mixtures at controlled pressure and temperature conditions. The objectives of the tests were threefold: (1) Evaluate the pressure control and response time of the two-state measurement system; (2) Determine the gas volumetric replacement time required for independent measurements in the integrated sound speed and carbon dioxide test chamber; (3) Collect experimental measurements of sound speed and carbon dioxide concentration to provide a database for evaluating the sensors and for use in evaluating the two-state inferential algorithm.

These tests were conducted under laboratory room temperature conditions using manual entry of pressure commands to the programmable pressure controller, with the test chamber pressure, temperature, and carbon dioxide 4-20 ma sensor readings recorded at 2-second time intervals using an HP Model 34970A data logger. Analog ultrasonic waveforms were acquired by the speed of sound electronics system using the Ultran Model NCT-510 1-MHz transducer installed in the speed of sound test chamber. The ultrasonic data were recorded using a Tektronix Model TDS-3032 digital oscilloscope capable of storing the waveforms on 3-1/2 in. magnetic diskette. The ultrasonic waveforms were digitized at 50 MSamples/sec using repetitive transient signal averaging at 16, 32, 64, and 128 waveforms per average. Each recorded waveform contained 10,000 sample points representing a 200-μsec time window in which the ultrasonic reflections, having a nominal time spacing in the range of 55-65 μsec, were observed and recorded. The recorded carbon dioxide sensor data and ultrasonic waveform data were processed off-line to provide pressure-compensated CO_2 readings and interpolated sound speed readings for use in sensor performance evaluations and for evaluating the two-state inferential algorithm.

The laboratory tests consisted of two experimental procedures: (1) Test chamber gas purge/replacement time measurements; and (2) speed of sound and carbon dioxide sensor measurements. The procedures used in these tests are briefly described below.

***Test Chamber Gas Purge/Replacement Time Tests*:** Two of the four test gases were passed through the prototype Energy Meter module at a flow rate of 50 ml/min and pressure of 70 psia. The purpose of the tests was to determine the gas throughput time required to achieve stabilized speed of sound measurements after a change in the flowing gas composition. Since only preliminary information was available to indicate the effective replacement time, the test chamber was purged with the first test gas for a period of about 25 minutes before initiating the purge test using the second test gas. Ultrasonic waveforms were then recorded with a constant gas pressure and flow rate at approximately 1-minute time intervals for a period of 25 minutes. This test procedure was then repeated using the first test gas as the replacement gas at the same throughput flow and pressure conditions. The ultrasonic waveforms were later analyzed to

determine the time required to achieve stable speed of sound measurements in the replacement gases.

***Two-State Energy Meter Sensor Tests*:** The four natural gas mixtures used in these tests contained different amounts of methane and diluent gas concentrations and thus had distinctly different values of sound speed and carbon dioxide concentration by which the performance of the sensors could be evaluated. The tests were performed at six pressure states of 65, 70, 75, 95, 120, and 145 psia under relatively constant room temperature conditions of 74±1ºF. Since the normal (1 atm) carbon dioxide sensor full-scale measurement range is compressed at increased pressures, only the readings at 65, 70, and 75 psia were used in evaluating the CO_2 sensor response to pressure changes and the ability of the pressure corrections to compensate for nonlinearities in the sensor readings at elevated pressures. In this regard, the Vaisala Model GMP 221 probe and GMT 220 transmitter could provide a compensated full-scale range of about 3 mol% after pressure compensation of the measurements at 65 psia. Tests were performed with the sensor power on and off during the higher pressure tests to determine possible effects of off-scale measurements in the sensor electronics system. Sound speed measurements were recorded at the six different pressures to provide information on speed of sound over the pressure range of interest and as a basis for determining the effects of separation between pressure states on the accuracy of the two-state energy analysis algorithm. For these tests, the selected test gas was purged through the gas test chamber at a pressure of 75 psia and a flow rate of 90-100 ml/min for a time period of 15 min. Sound speed measurements were then performed at increasing pressure steps beginning at 65 psia and ending at 145 psia, with gas flow adjusted to 20 ml/min at each pressure. A period of approximately 4 minutes at the beginning of each pressure condition was allowed for temperature and pressure stabilization, followed by a four-waveform data recording interval of approximately 6 minutes.

Table 6-4 lists the compositions of the four certified natural gas mixtures used in the laboratory tests. Figure 6-40 shows a diagram of the equipment set-up used in the tests.

Table 6-4. Four certified natural gas mixtures used in the prototype energy meter laboratory tests.

GAS COMPONENT	TEST GAS B (mol%)	TEST GAS C (mol%)	TEST GAS D (mol%)	TEST GAS E (mol%)
Nitrogen	2.1700	3.0900	1.2900	0.995
Carbon Dioxide	1.9000	2.8500	0.5000	0.499
Methane	92.1272	90.8336	90.0811	94.766
Ethane	2.5300	2.4300	6.6200	1.995
Propane	0.5000	0.4860	1.1200	0.751
Isobutane	0.1050	0.0970	0.0960	0.299
n-Butane	0.1030	0.1040	0.0940	0.300
Isopentane	0.0505	0.0500	0.0496	0.147
n-Pentane	0.0100	0.0100	0.0990	0.148
n-Hexane	0.0199	0.0198	0.0200	0.100
n-Heptane	0.0197	0.0196	0.0201	0.000
n-Octane	0.0102	0.0100	0.0103	0.000
Total	100.0000	100.0000	100.000	100.000

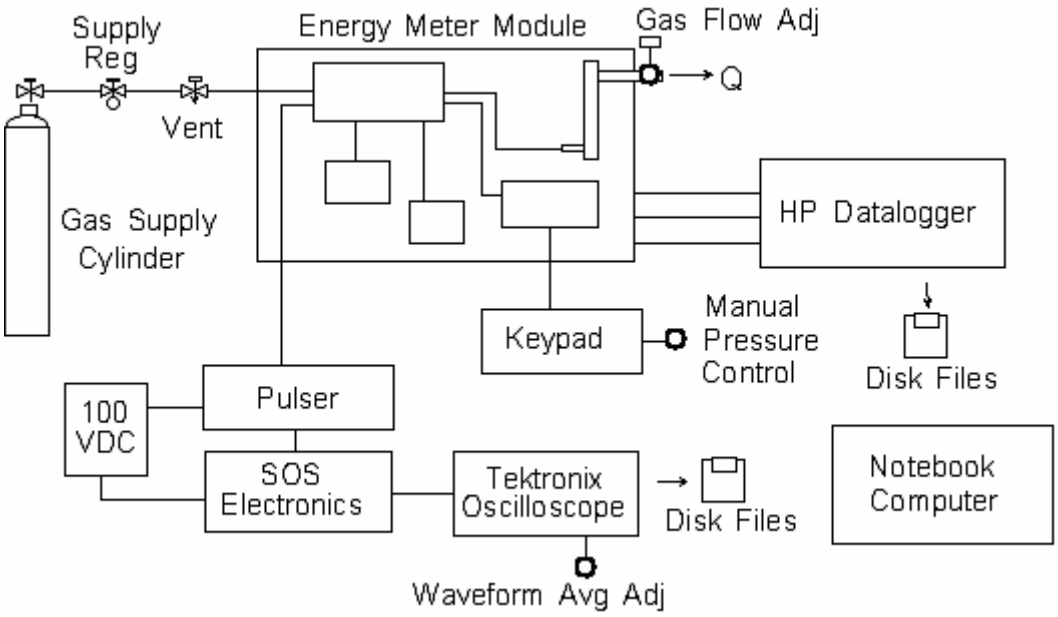

Figure 6-40. Laboratory test setup for the 2003 energy meter module.

6.4.2 Laboratory Test Results

***Programmable Pressure Regulator Command/Response*:** The pressure response time of the electrically controlled pressure regulator used to control the six pressure states is relatively independent of the operating pressure of the module, provided that the upstream supply pressure is greater than the highest command pressure by about 30 psi. The stabilization time for pressure

changes from low pressure to high pressure is inherently faster than for pressure changes in the reverse direction, since the required pressure relief is dependent upon the gas flow rate at the test chamber exit port. The pressure- response curves for step changes of 65-70, 70-75, 75-95, 95-120, and 120-145 psia are presented in Figure 6-41.

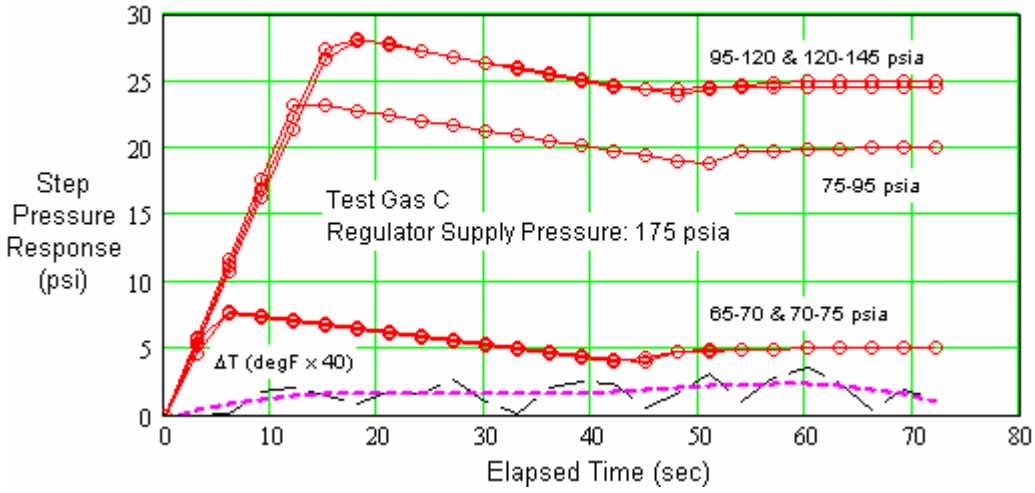

Figure 6-41. Responses to step commands from the programmable pressure regulator.

The regulator has a pressure response rate of approximately 1.8 psi/sec for all of the pressure state steps, with an overshoot of about 3 psi above the step command pressure. The settling characteristics for the five step changes are similar in response and are stabilized at the command pressure within approximately 60 seconds of the command. Figure 6-41 also illustrates the adiabatic temperature change observed during the 120-145 psia pressure step, in units of ºF magnified by a factor of 40. The indicated temperature change is very near the resolution threshold of the temperature sensor, but tends to peak at about 0.07°F above the starting gas temperature at about 60 sec after the pressure-step command. The temperature stabilization time is estimated to be about the same as the 60-sec pressure stabilization time, but for pressure changes of $\Delta P \leq 25$ psi, the actual change in temperature can be neglected.

***Gas Purge/Replacement Time*:** The steady-flow gas replacement time was measured for the integrated sound speed and CO_2 sensor test chamber at a constant pressure of 70 psia and gas-release flow rate of 50 ml/min. The physical volume of the sound speed section of the chamber is 21.2 cm^3, and the CO_2 chamber volume is approximately one half that of the sound speed chamber. Figure 6-42 shows the test results for speed of sound and CO_2 transition measurements when replacing test gas B with test gas D. The stabilization time for sound speed measurements for the specified test conditions is 12.3 minutes and the stabilization time for CO_2 measurements is 16 minutes. The difference in these times is caused by the tandem connection of the two sections of the chamber whereby gas replacement in the CO_2 chamber is delayed by about 2 minutes, and the gas flow and diffusion into the CO_2 sensor is impeded by the probe's internal porous filter membrane and protective end cap housing. Removal of these parts of the sensor probe is practical within the present sensor chamber design and is recommended.

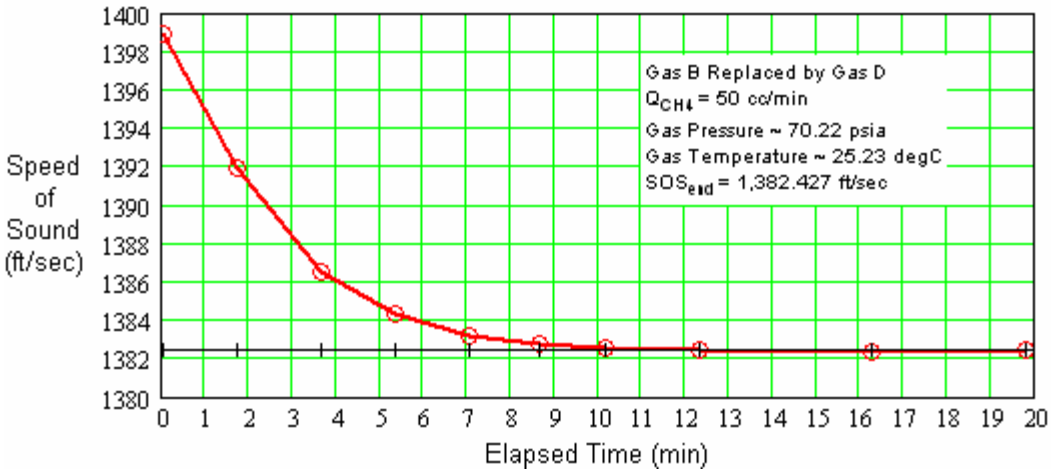

(a)

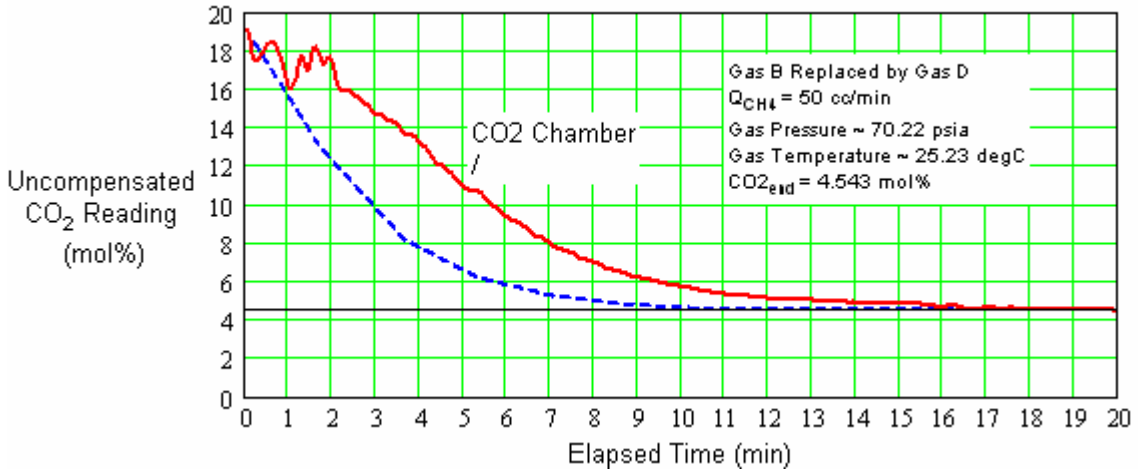

(b)

Figure 6-42. Gas purge/replacement times in the integrated sound speed-CO_2 sensor test chamber. (a) Test gas replacement response time of the speed of sound sensor chamber; (b) Replacement response time of the CO_2 sensor chamber with the sound speed response superimposed for comparison.

Carbon Dioxide Sensor Measurements: The raw CO_2 readings at the three lowest pressure states in each test gas were compensated and adjusted in calibration using the nonlinear pressure correction procedure described in Chapter 4. Table 6-5 compares the corrected values to the certified values for each test gas. Test gas C, having a CO_2 content of 2.850 mol%, caused off-scale sensor readings at all test pressures. For test gases B, C, and D, the comparison shows the compensated sensor measurements to be within the accuracy tolerance of $\Delta X_{CO2} = \pm 0.05$ mol% required by the energy analysis algorithm. Measurements of CO_2 concentration in test gas C and at values higher than 2.850 mol% will require a lower pressure in the sensor test chamber. The measurement response time of the CO_2 sensor at all pressures where measurements were made

(the lower pressures of 65, 70, and 75 psia) appeared to be more stable when power was removed from the sensor probe at the higher test pressures (where measurements were not performed).

Table 6-5. Pressure-compensated carbon dioxide readings for the four certified test gases.

Test Gas	Pressure (psia)	Temperature (ºF)	Measured X_{CO2} (mol%)	Certified X_{CO2} (mol%)	Error X_{CO2} (mol%)
B	70.34	75.97	1.93919	1.900	0.03919
B	60.38	75.91	1.92291	1.900	0.02291
B	50.35	75.86	1.87571	1.900	-0.02429
C	CO_2 sensor	off scale at all	test pressures	2.850	---
D	70.40	76.62	0.50335	0.500	0.00335
D	60.38	76.58	0.51354	0.500	0.01354
D	50.35	76.58	0.55129	0.500	0.05129
E	70.43	75.29	0.47833	0.499	-0.02067
E	60.41	75.20	0.47640	0.499	-0.02260
E	50.38	75.12	0.48971	0.499	-0.00929

***Speed of Sound Sensor Measurements*:** The ultrasonic waveforms recorded at the six pressure-temperature states in each test gas were processed to yield the speed of sound for each state using the cross correlation and coherence peak interpolation procedures described in Section 3.4. All of the derived experimental values of sound speed were calibrated using the design spacing between the two reflecting faces, namely, 0.5000 in. The pressure and temperature conditions defining the thermodynamic state at which the four different signal-averaged waveforms were recorded were obtained by averaging the pressure and temperature values accumulated by the data logger over the approximately 6-minute period required to sequentially adjust and store the different oscilloscope waveforms to 3-1/2 in. magnetic disk. Although the variations in pressure and temperature during these individual data averaging intervals are small, the effects of associating such an "average" pressure-temperature state with the four different experimental sound speed measurements has not yet been determined. Also, because the time required to complete the six measurement states for each test gas was about three hours, the measured gas temperature typically changed by as much as 1.5°F during each test gas experiment.

The experimental sound speed measurements at each pressure-temperature state in the test gases were compared with values calculated using the AGA-10 equation of state, the certified gas compositions, and the "average" pressure-temperature states at the time of the measurements. Figure 6-43 presents these values plotted versus pressure.

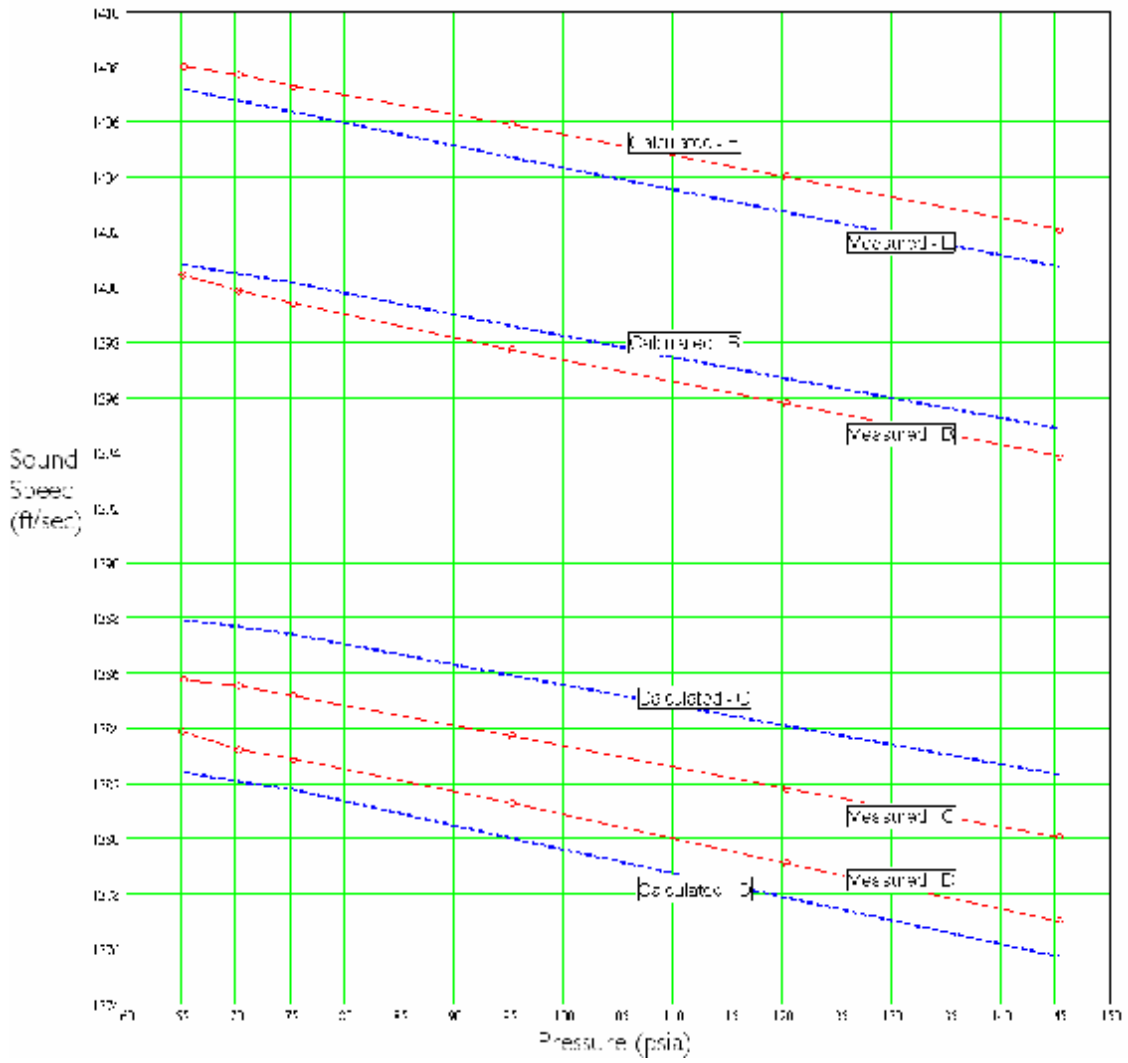

Figure 6-43. Comparison of measured and calculated speed of sound values in the four certified test gases.

The results in Figure 6-43 show that, while the general trends in sound speed are the same in the experimental and calculated values, none of the four test gases are suitable as an accurate common calibration reference gas using the calibration adjustment procedure presented earlier in Section 3.4.1. Test gases D and E come closest to having a common calibration factor, but shifting their experimental points down to match the calculated values would only increase the errors observed in test gases B and C. Therefore, there is a clear uncertainty concerning the accuracy of the experimental measurements and the calculated values of sound speed in these test gases.

While the laboratory test results obtained so far cannot resolve the observed discrepancies, possible reasons include:

1. Composition-dependent measurement bias in the sound speed sensor;
2. Inaccuracy in the certified test gas compositions;
3. Inaccuracy in sound speed calculations implemented in the AGA-10 equation of state.

The potential bias in the sound speed sensor can only be resolved by conducting additional measurements using ultrapure gases such as argon, nitrogen, methane, ethane, or other test gases compatible with the ultrasonic sensor equipment, so that gas composition is removed as a possible unknown. In this case, sound speed measurements on any of several pure gases can be compared with well documented values reported in the literature (Zuckerwar [2002]) to verify the performance and calibration of the sensor. The measured values can also be compared with values calculated using the AGA-10 equation of state and other similar equations of state as a basis for evaluating the calculated results.

The question of inaccuracies in the certified gas compositions can be investigated by obtaining other certified assays of the specific test gases used in the present sound speed measurements. With such supplemental gas composition information available, the sound speed calculations can be repeated for comparison with the previous measured values. Assay measurements capable of discrete determination of hydrocarbon constituents through C_{10} may be important in resolving questions concerning uncertainties related to gas compositions and the associated effects on calculated speed of sound.

A second feature by which the sound speed data in Figure 6-43 disagree is the small but noticeable differences in the offset bias between the measured and calculated values. These differences are presented in more detail in Figure 6-44, where the measured values are shifted to match the calculated values at the 95 psia test pressure and the differences at the other test pressures are calculated and plotted.

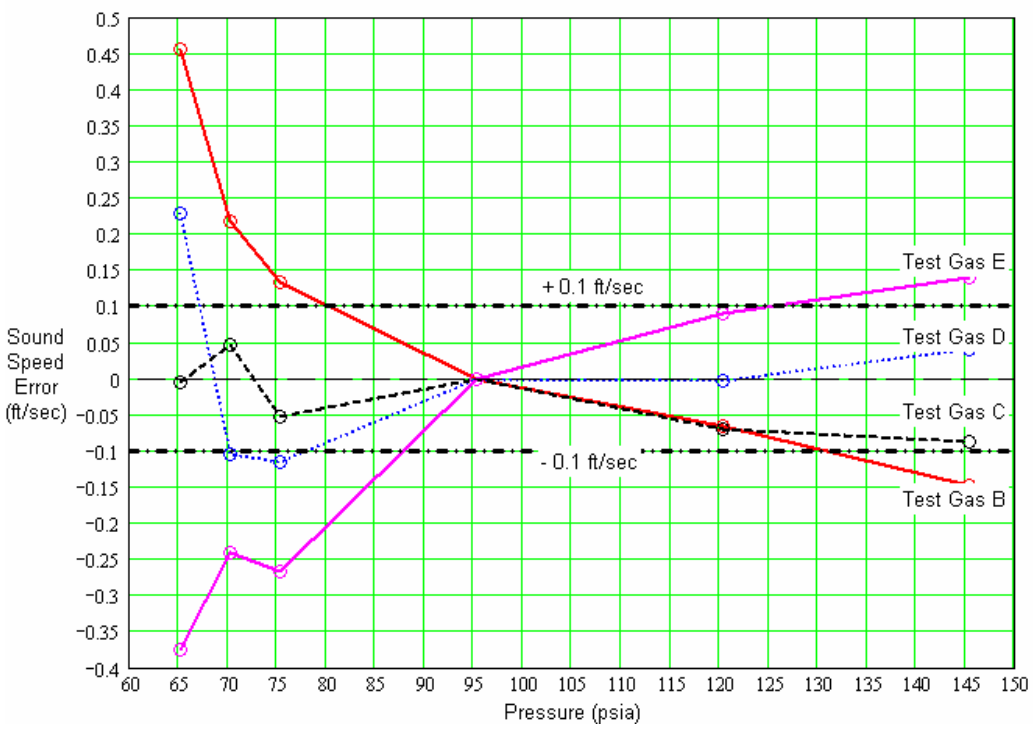

Figure 6-44. Differences between measured and calculated speed of sound values when measured results from each gas are calibrated to match the calculated value at 95 psia.

These results show greater differences for all of the test gases at the lower pressures, but the signs of the differences for test gases B and C tend to be opposite from those of test gases D and E. The larger differences at the lower pressures are related to the signal-to-noise ratios of the ultrasonic waveforms, which are affected by the reduced acoustic impedance of the gas and the associated lower efficiency in coupling sound energy into the gas. The differences at the higher pressures are smaller, but still exhibit systematic differences in sign between gases B and C and gases D and E. Error effects of this kind imply that there may be some form of pressure dependent condition in the test gas that is not accounted for in the thermodynamic equation of state, or possibly some extraneous pressure effect in the sensor apparatus or in the way that the manually controlled experimental measurements were performed. Fully automating the data acquisition process as planned in the future version of the Energy Meter module can be expected to alleviate the latter source of possible error.

Although the pressure-related variations in Figure 6-44 cannot be resolved at this time, two possible sources of such errors are the effects of viscous friction absorption in the gas, a predictable macroscale effect in most gases, and molecular vibration absorption in the gas, a more composition-dependent effect occurring at the molecular level in polyatomic gases. Both of these absorption effects introduce sound energy losses along the propagation path and, since sound velocity dispersion (i.e., frequency-dependent propagation velocity) always accompanies attenuation, there can be a potential change in the speed of sound when measured at different frequencies. Viscous attenuation increases as the square of frequency and therefore increases monotonically with frequency in all gases. Molecular relaxation absorption occurs when sound

waves at frequencies near the vibration resonances of specific molecules expend part of their energy in exciting those molecules in an irreversible manner. This frequency selective absorption effect is temperature and pressure dependent, and is affected by complex molecular vibration interactions in gas mixtures containing several components. For this reason, molecular relaxation effects in natural gas are impractical to predict with quantitative accuracy. However, an invariant feature of such molecular relaxation is to cause an increase in the ratio of specific heats in the gas and, hence, cause an attendant increase in the speed of sound in comparison with values calculated by thermodynamic considerations alone. Such frequency-dependent effects are measurable and may potentially introduce noticeable variations in precision measurements of the speed of sound when using different measuring frequencies.

The test results in Figure 6-43 indicate that gases D and E tentatively exhibit the possible influences of velocity dispersion, whereas gases B and C require other explanations for their discrepancies. In this case, the presence of the two pairs of ambiguous sound speed comparisons suggests that velocity dispersion is not necessarily the most likely prospect for explaining the disagreement among the measured and calculated values. Additional experimental measurements at two different ultrasonic frequencies, one using the present 1-MHz transducer and the other at a substantially lower frequency, will provide useful information by which any frequency-dependent velocity dispersion effects may be observed and evaluated.

This page is intentionally blank.

7. INFERENTIAL METHODS OF DETERMINING NITROGEN CONCENTRATION

During the 2000-2001 research program, several potential methods were identified to infer the nitrogen concentration of a gas stream from other measurable gas properties, such as viscosity, heat capacity, or infrared light absorption (Kelner et al. [2004]). Additional methods were identified during the 2002-2003 research program that also relied on correlating the nitrogen content with measurable properties of natural gas. Because of available resources, not all the methods could be pursued experimentally. One of the untested methods would have used a known amount of nitrogen added to the gas sample to perturb the properties of the gas, and the measured changes in gas properties would have been used to infer the original nitrogen content. Another untested method involved the measurement of ultrasound energy attenuation in natural gas to infer nitrogen content. The fact that these methods were not tested should not be taken to mean that the methods were inaccurate, but only that they could not practically be evaluated as part of the project scope of work.

Two of the methods conceived for determining N_2 during the research program were evaluated experimentally, both of them involving measurements of the gas viscosity. This section describes both inferential methods, presents results of tests of both methods, and reports their potential for determining the nitrogen content of natural gas streams.

7.1 HONEYWELL NATURAL GAS SENSORS

One approach evaluated for nitrogen measurement was first identified as part of the 2000-2001 scope of work. This approach involved commercial thermal anemometers, modified by Honeywell Laboratories to measure properties of natural gas or other flammable gases at high flow rates up to 200 m/s. As described by Bonne and Kubisiak [2001], actuators, or "speakers," induced pulsations in a natural gas sample, and a ruggedized thermal anemometer was used to measure the response of the gas sample to the pulsations. The sensor response could be used to infer various gas properties such as specific heat at constant pressure (c_p), the ratio of specific heats (g), thermal conductivity (k), and dynamic viscosity (m). In one implementation described by the authors, a pair of these ruggedized anemometers, or "microbricks," could be used to simultaneously measure gas properties in a main gas line and in a sample of the gas held in a separate measurement chamber. The difference in the gas response to the acoustic pulsations at the two different locations would be measured by the microbricks and used to infer the properties of interest.

The approach conceived to incorporate the sensor into the energy meter module would use a gas property measured by the sensor as an input variable to the algorithm. This would require that the measured property correlate accurately to nitrogen content. Several test correlations were created and evaluated for their ability to accurately predict nitrogen content and gas density at STP (standard temperature and pressure, 60°F and 14.696 psia) as a function of CO_2 content, sound speed at STP, and each of the gas properties that could be inferred from the microbrick sensor. For example, the correlations with specific heat (c_p) took the form:

$$r_{STP} = A_0 + A_1 c_p + A_2 X_{CO2} + S\left(B_0 + B_1 c_p + B_2 X_{CO2}\right) + S^2\left(C_0 + C_1 c_p + C_2 X_{CO2}\right) \quad (7\text{-}1)$$

$$X_{N2} = A_3 + A_4 c_p + A_5 X_{CO2} + S\left(B_3 + B_4 c_p + B_5 X_{CO2}\right) + S^2\left(C_3 + C_4 c_p + C_5 X_{CO2}\right) \quad (7\text{-}2)$$

where:

r_{STP} = density of the gas at standard temperature and pressure;
X_{N2} = mole fraction of nitrogen in the gas;
S = speed of sound in the gas at standard temperature and pressure; and
X_{CO2} = mole fraction of carbon dioxide in the gas.

Correlations of this form were also used to relate density and nitrogen content to the specific heat ratio, thermal conductivity, and dynamic viscosity. The coefficients A_i, B_i and C_i were generated using data at STP for a database of 118 gases found in the literature (Gas Research Institute [1998], Morrow et al. [2000]).

The results revealed that the specific heat quantities, c_p and g, correlated closely to nitrogen content. The correlations with both c_p and g predicted density at STP for all the database gases to within a very acceptable accuracy of ±0.05 mol%, and could predict N_2 concentration to within ±0.25 mol%. Similarly, a correlation with dynamic viscosity (m) predicted STP density for the database gases to within an accuracy of ±0.08 mol% and N_2 concentration to within ±0.31 mol% (Figure 7-1). However, the correlation between viscosity and nitrogen content had a slightly better correlation coefficient and a tighter 95% confidence interval than the correlations between N_2 and c_p or g (Table 7-1), making viscosity the first choice of all quantities measured by the microbrick sensor for inclusion in the algorithm. Although the design criterion of measuring N_2 to within ±0.05 mol% could not be achieved using the quadratic correlations of Equation 7-2, the Honeywell "microbrick" sensors were seen as having the potential to accurately measure properties needed for nitrogen content, heating values and energy flow rates. Further, the microbrick sensors required minimal development to be incorporated into the energy meter. It was decided to pursue this option, and discussions were held with a representative of Honeywell to evaluate the “microbrick” as a viscosity sensor.

Table 7-1. Comparison of the goodness of fit of correlations between properties measured by the Honeywell microbrick sensor and natural gas nitrogen content.

Measured Gas Property	r^2 Goodness of Fit	U_{95} Confidence Interval on N_2 Regression (mol%)
Viscosity (m)	0.9978	± 0.14
Specific Heat (C_p)	0.9976	± 0.15
Ratio of specific heats (g)	0.9968	± 0.17
Thermal conductivity (k)	0.4510	± 2.24

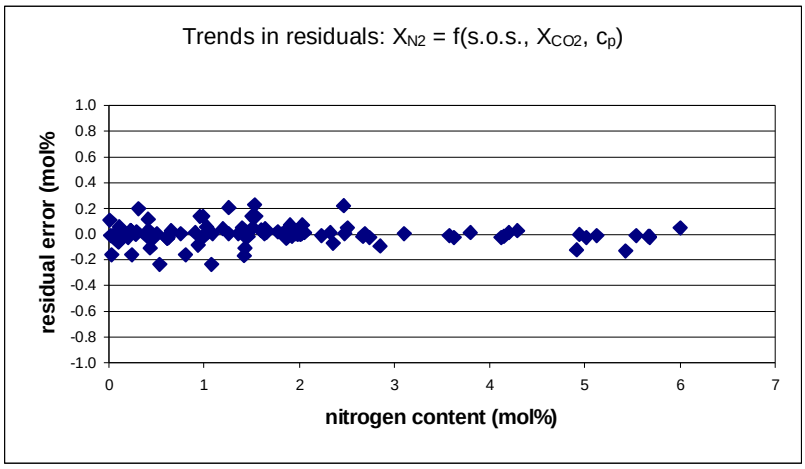

(a)

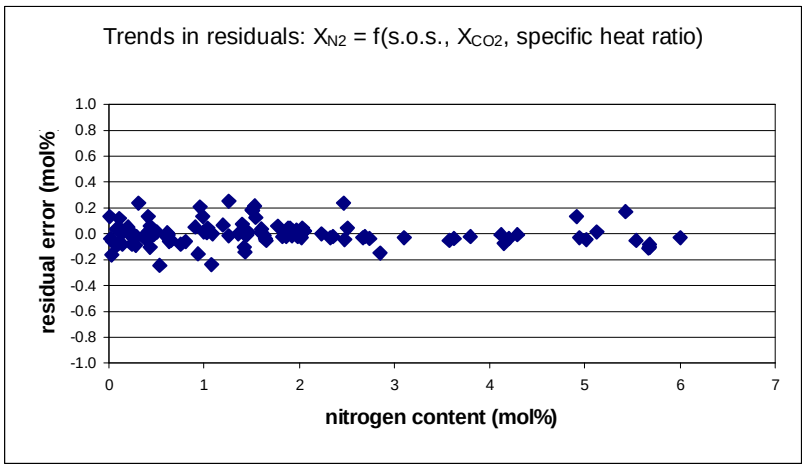

(b)

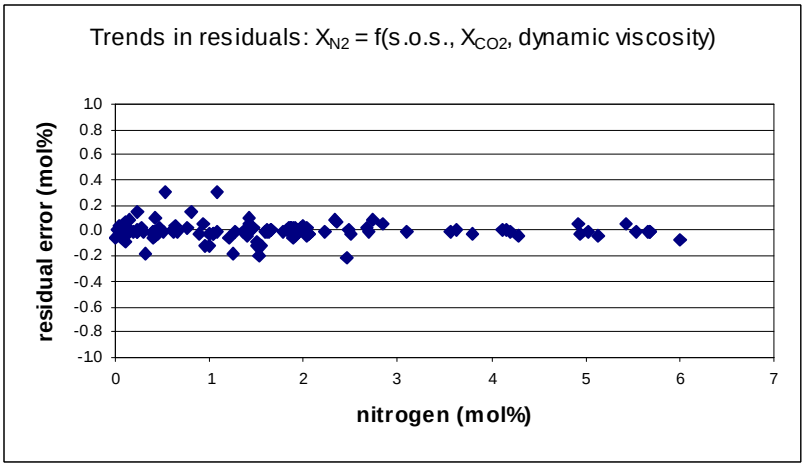

(c)

Figure 7-1. Errors in nitrogen content predicted by quadratic correlations to sound speed, CO_2 content, and properties measured by the Honeywell microbrick sensor: (a) specific heat at constant pressure; (b) specific heat ratio; (c) dynamic viscosity.

A series of tests was devised to assess the accuracy and steadiness of the viscosity measurements from the device, as well as the device's ability to detect changes in viscosity caused by changes in the amount of nitrogen in a natural gas mixture. The Honeywell viscosity sensor was initially tested in the MRF calibration lab, with the sensor placed in a housing exposed to quiescent room air. Room conditions were measured with a high-accuracy pressure gauge and thermocouple. Reference values of air viscosity were calculated with commercial software (Lomic, Inc. [1996]) using the measured room conditions and a standard air composition (Weast et al. [1995]) as input. After initial transients during startup, viscosity measurements from the sensor stabilized, and varied by no more than ± 2% over a thirty-second period. Average measured values of air viscosity exhibited a 5 to 7 micropoise (μP) bias relative to computed reference values, but this was traced to a consistent offset in temperature measurements from the sensor relative to the reference room temperature.

The sensor was then moved to the MRF Low Pressure Loop (LPL) to test its accuracy in a natural gas flow; however, the tests could not be completed due to problems with the sensor electronics. It was concluded that the Honeywell microbrick design showed promise, but that the viscosity sensor on hand had insufficient stability for use in the energy meter prototype. It was decided to end tests of the sensor, and to determine Honeywell's interest in developing an improved sensor for future testing and possible use by SwRI. Discussions began with Honeywell for development of an improved sensor, but the microbrick approach was eventually abandoned in favor of the multiple-states approach described in Section 2.2 of this report.

7.2 LAMINAR FLOW VISCOSITY MEASUREMENTS

During the tests of the Honeywell sensor, requirements were developed for values of measured viscosity that would yield results from the energy meter algorithm with the desired accuracy. General specifications were drawn up from these requirements for viscosity sensors that could be used as part of the energy meter system. Upon completion of the microbrick tests, it was decided to determine if laminar flow elements could instead be incorporated into the energy meter prototype and meet the accuracy requirements for viscosity measurement.

The first candidate for a laminar flow element was the existing speed of sound chamber, which used a long capillary tube in the outer shell to equilibrate the temperature of the gas sample before it entered the chamber (Figure 7-2). Since gas flow through the capillary tube and the chamber itself are both laminar, it was deduced that the speed of sound apparatus might be calibrated as a laminar flow element to measure gas viscosity. Implementing this approach would require a differential pressure measurement across the inlet and outlet of the chamber, and a means to measure the flow rate through the chamber. Initial design calculations indicated that common pressure transmitters could be used to measure the pressure drop across the chamber's capillary tube, and a commercial miniature turbine flow meter was identified that was capable of measuring the flow rate through the speed of sound/CO_2 sensor loop with acceptable accuracy. Although the total pressure drop across the chamber (excluding the capillary tube) could not be measured within the required uncertainty limits using common commercial pressure transmitters,

it was decided to test the viscosity measurement concept experimentally in the energy meter module using these instruments.

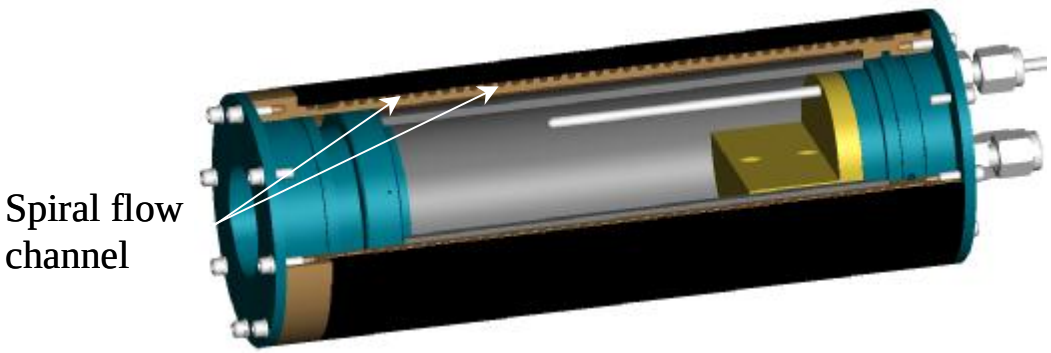

Figure 7-2. Cross-section of the prototype speed of sound chamber, showing the spiral laminar flow chamber used for viscosity measurements.

To test the energy meter module as a viscometer, the chambers for the sound speed and CO_2 sensors were removed from the module and arranged on a workbench in the MRF calibration lab. An OmniFlo® Model FTO-2 miniature turbine meter with jewel bearings was fabricated by Flow Technology™ and calibrated in natural gas to provide an accurate calibration curve for the tests. The calibrated miniature turbine meter and its transmitter were incorporated into the module instrument chain upstream of the sound speed and CO_2 chambers. A Rosemount pressure transmitter was obtained and calibrated to measure the expected pressure drop across the sound speed chamber. Preliminary tests of the setup performed with nitrogen gas, however, showed that the pressure drop across the speed of sound chamber had been overestimated by the design calculations. An MKS Baratron® high-accuracy differential pressure transmitter, capable of measuring differential pressures on the order of 100 torr (about 2 inches of water column), was then substituted for the original transmitter. Measured differential pressures across the speed of sound chamber then responded as expected to changes in measured flow rate, and a preliminary calibration factor in nitrogen was computed for the "laminar flow module." The arrangement of the instruments after installation of the MKS transmitter is shown in Figure 7-3.

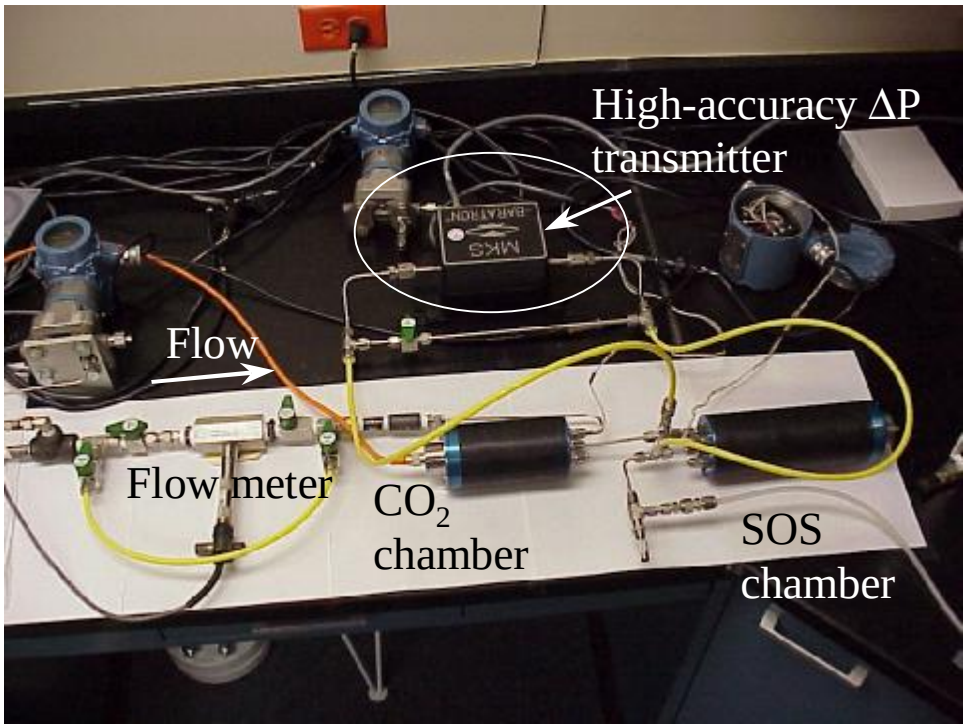

Figure 7-3. Instrument chain used to test the potential of the sound speed chamber for measuring gas viscosity.

The relationship between viscosity and the pressure drop through the laminar flow channel is analogous to Poiseuille's equation of volumetric flow through a capillary tube:

$$Q = \frac{\Delta P \cdot pr^4}{8Lm} = K\frac{\Delta P}{m} \tag{7-3}$$

where:

Q = volumetric flow rate through the tube;
ΔP = pressure drop across the length of the tube;
r = internal radius of the tube bore;
L = length of the capillary tube; and
K = constant incorporating all geometric terms.

Note that in either the case of a round capillary tube or the semicircular cross section of the laminar flow channel, all geometric terms can be condensed into a single constant K. By testing the apparatus in a gas of known viscosity and flow rate and measuring ΔP, this constant can be determined, and the setup can be calibrated and used to measure the viscosity of other, unknown gases.

Calibration of the speed of sound/turbine meter viscometer began with a certified natural gas mixture of known viscosity. According to Poiseuille's law (Equation 7-3), an ideal viscometer

will have a single, constant calibration factor over a range of flow rates and gas viscosities. The calibration factor of the system was found to vary, however. Specifically, the measured flow rates and differential pressure data were repeatable, but did not behave as predicted by Poiseuille's law. Because the speed of sound chamber involved a complex internal geometry, it was theorized that secondary flows in the chamber and other deviations from Poiseuille flow might have occurred, introducing error into Equation 7-3. It was then decided to test the approach using a simpler geometry of a capillary tube alone.

Coiled copper tubing with a circular cross section, an internal diameter of 1/8" and a length of 50 feet was substituted for the speed of sound chamber to serve as the capillary tube. This combination was calibrated on three known gas compositions, and further tests were run with two other gases having similar viscosities. Again, the calibration factors were not constant, but varied with both flow rate and viscosity (Figure 7-4). While trends in the calibration factor with flow rate and viscosity were mostly predictable, use of this system with a single calibration factor would lead to unacceptable errors in viscosity of as much as ±10%.

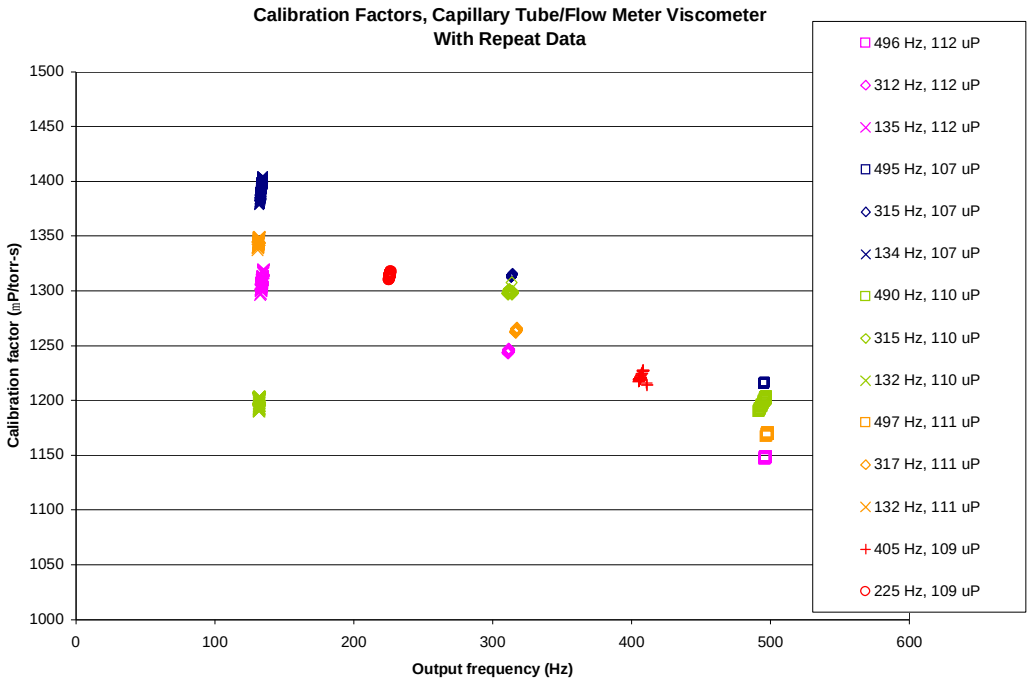

Figure 7-4. Calibration data from tests of the coiled copper tube as a viscometer.

Causes of the variable calibration factor were considered. The miniature turbine meter was checked against a reference-quality bubble flow meter in the MRF calibration lab, and was found to be in good agreement with the bubble meter, eliminating the turbine meter as a source of error. It was also theorized that the flow might not have fully developed into laminar flow early enough for Poiseuille's law to be accurate along the entire length of tube. However, calculations for

worst-case conditions showed the development length to be no more than 2.2% of the total capillary length, and this theory was rejected. It was also theorized that the curvature of the coiled copper tube might not have provided ideal laminar flow conditions, and might have caused the observed changes in calibration factor with flow rate and viscosity. This could also have partly contributed to the varying calibration factor from tests with the speed of sound chamber, since the capillary channel was coiled around the chamber itself to maximize heat transfer and equilibrate the gas temperature.

A method of correcting Poiseuille's law for curved capillary tubes was identified. However, to first test the theory of non-ideal laminar flow conditions in the tubing, it was decided to perform measurements with a straight laminar flow path for the gas that would not introduce secondary flow effects. The copper tubing in the instrument chain was replaced with a Meriam Instruments laminar flow element with a maximum flow rate of 0.1 standard cubic feet per minute and a maximum differential pressure of 8 inches of water column. Experiments were performed using three certified natural gas blends to calibrate the LFE/turbine meter system. The test gases ranged in nitrogen content from 3.0 mol% to 7.0 mol%, and represented a viscosity range of approximately 108 to 111 micropoise (μP) at 75 psia. Seven flow rates spanning the lower half of the turbine meter's full-scale range were tested. After analysis of the data from the LFE, the calibration factor derived from Poiseuille's Law was still found to depend on flow rate, though the dependence became smaller as the flow rate increased (Figure 7-5).

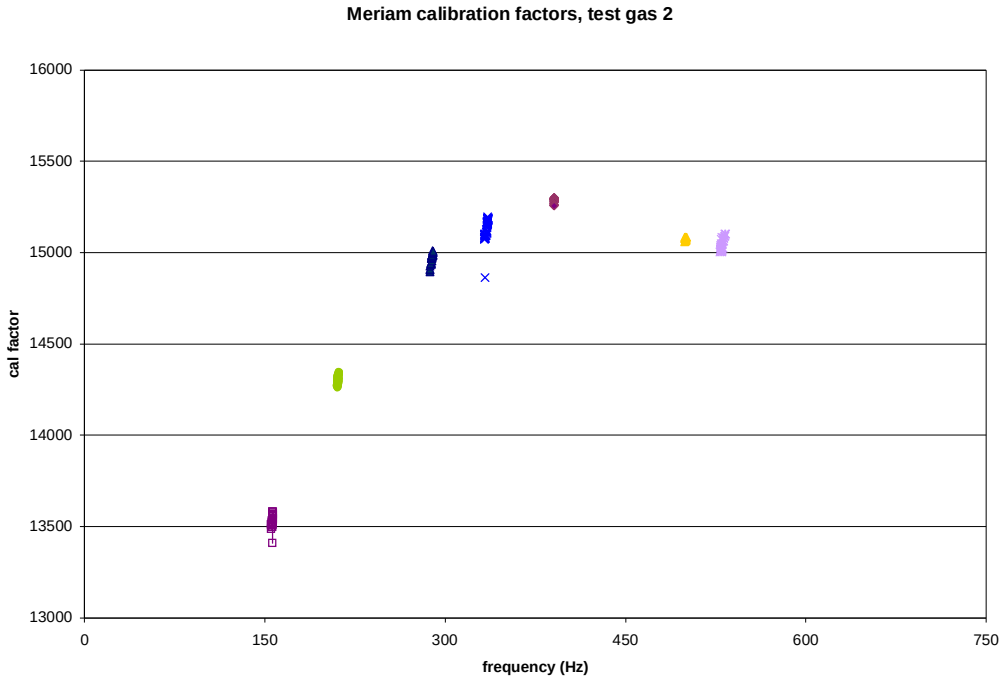

Figure 7-5. Example of calibration data for the commercial laminar flow element viscometer.

Clearly, a better understanding was needed of the variables that caused the dependency of the geometrical calibration factor on flow rate. Tests of the LFE/turbine meter system were performed with a fourth test gas to gain more data on the behavior of the calibration factor and determine the cause of the flow rate dependency. Unlike the first three test gases, which were used as calibration gases for the system, the fourth test gas was used to test the accuracy of the calibration equation itself. Tests with the fourth gas over the course of several days determined that the gas temperature, influenced by the ambient temperature of the lab, could significantly shift the calibration curve. A change of 4ºF in gas temperature was found to shift the calibration factor by approximately 7% at the high flow rates and 20% at the low flow rates. This indicated that the laminar flow element method for determining viscosity could be highly influenced by small temperature shifts, especially at low gas flow rates.

In a final investigation, the four gases were tested again, with the gas temperature and ambient temperature held to within 1.5ºF. The three test gases were used to generate an average calibration curve over a range of flow rates; that curve was then used to determine viscosity in the fourth test gas over the same flow rates. The errors in viscosities calculated from the calibration curve ranged from 1.0% to 5.0% (1.1 to 5.4 μP), with the higher flows having a larger error. These errors in viscosity would lead to errors in computed nitrogen content significantly larger than the target of 0.05 mol%.

At this point, no further work on viscosity measurement was performed. Although the flow rate dependency of the calibration factor was not resolved during the tests and remains a primary uncertainty in the method, it was concluded from these results that the laminar flow method of viscosity measurement would not be viable for inferring the nitrogen content of natural gas. As with the Honeywell sensor, this technique was set aside in favor of the multiple-states method described in Section 2.2 of this report.

This page is intentionally blank.

8. REFERENCES

American Gas Association [1994], AGA Report No. 8, *Compressibility Factors of Natural Gas and Other Related Hydrocarbon Gases*, Second Edition, Second Printing, American Gas Association, Arlington, Virginia, USA.

American Gas Association [2003], AGA Report No. 10, *Speed of Sound in Natural Gas and Other Related Hydrocarbon Gases*, American Gas Association, Washington, DC, USA.

Behring II, K., Kelner, E., Minachi, A., Sparks, C., Morrow, T., and Svedeman, S. [1999], "A Technology Assessment and Feasibility Evaluation of Natural Gas Energy Flow Measurement Alternatives," Final Report, Tasks A and B, under U. S. Department of Energy Cooperative Agreement No. DE-FC21-96MC33033, Southwest Research Institute, San Antonio, Texas, USA.

Bonne, U., and Kubisiak, D. [2001], "Actuation-Based Natural Gas Microsensors," Proceedings of the GTI 2001 Natural Gas Quality, Energy Measurement, Metering, and Utilization Conference.

Gas Research Institute [1998], GRI's Gas Resource Database, Unconventional Natural Gas and Gas Composition Databases, CD-ROM Report GRI-98/0364.3, Gas Research Institute, Chicago, Illinois, USA.

Gas Processors Association [1994], *Table of Physical Constants of Paraffin Hydrocarbons and Other Components of Natural Gas*, GPA Standard 2145-94, Gas Processors Association, Tulsa, Oklahoma, USA.

Kelner, E., Owen, T.E., George, D.L., Minachi, A., Nored, M.G., and Schwartz, C.J. [2004], "Development of a Low-Cost Inferential Natural Gas Energy Flow Rate Prototype Retrofit Module," Topical Report, DOE Agreement No. DE-FC21-96MC33033, March 2004, Southwest Research Institute, San Antonio, Texas, USA.

Lomic, Inc., SonicWare® Speed of Sound Calculation Software, State College, Pennsylvania, USA, 1997.

Morrow, T.B., Kelner, E., and Minachi, A. [2000], "Metering Research Facility Program: Natural Gas Heating Value Determination," Topical Report to Gas Research Institute, Report GRI-00/0123, September 2000, Southwest Research Institute, San Antonio, Texas, USA.

Weast, R.C., Astle, M.J., and Beyer, W.H., editors [1985], *CRC Handbook of Chemistry and Physics*, 66th edition, CRC Press, Inc., Boca Raton, Florida, USA.

Zuckerwar, A.J. [2002], *Handbook of the Speed of Sound in Real Gases, Vol. 1*, Academic Press, San Diego, California, USA.